Università degli Studi di Cagliari

PhD DEGREE

Ingegneria Elettronica ed Informatica

Cycle XXXII

TITLE OF THE PhD THESIS

2D material-based electromagnetic devices

Scientific Disciplinary Sector

ING-INF/02

PhD Student: Nicola Curreli

Coordinator of the PhD Programme Prof. Alessandro Giua

Supervisor Prof. Giuseppe Mazzarella

Dr. Alessandro Fanti

Final exam. Academic Year 2018 – 2019

Thesis defence: January-February 2020 Session

CONTENTS

LIST OF FIGURES

INTRODUCTION

The realization of technologically-advanced components to be used in optoelectronic systems is one appealing research area in modern electronics. At present, a variety of materials and chemicals are used by the electronics industry. Some of the more common metals include copper, lithium, tin, silver, gold, nickel and aluminium. Silicon - considered a metalloid, or semiconductor - is used in microchips. Other non-metal or semimetal materials, largely used in the electronics industry, comprise antimony, bismuth, cobalt, fluorite, garnet and magnesium. For such materials, their high price is a critical issue. Moreover, the production of electronic devices generally involves polluting processes such as patterning and chemical etching. In order to address the aforementioned issues, alternative materials and processes must be developed considering the device requirements. A possible solution is to investigate the use of materials with different dimensionality. In fact, new fundamental material physical properties, superior to the ones of the bulk counterpart, can manifest themselves at the nanoscale. Moreover, the morphology of the nanomaterials, *i.e*. their dimensionality (zero-, one-, two- or three-dimensional), strongly affects the final properties. Among these dimensionalities, two-dimensional (2D) nanomaterials have been at the centre of a large part of the scientific community for over a decade after the isolation of few-layer graphene by Geim and Novoselov in 2004. In addition to graphene, many other layered materials of different composition have been isolated, covering the entire range of electronic properties, from insulators (*e.g*., hexagonal boron nitride) and semiconductors (*e.g*., indium selenide, gallium selenide, transition metal dichalcogenides) to metals and superconductors. Thanks to such properties, 2D materials provide the building blocks for a number of electronic devices, including lightweight and flexible displays, electric/photonics circuits, solar cells, medical devices, just to cite a few.

While these materials possess exceptional properties as they approach the monolayer thickness, to fully exploit the properties of these materials the production methods must be optimized with the aim to scaling up. In order to address the practical problem of the production of large quantities of 2D materials, a rapidly increasing list of production techniques have been recently developed to enable their use in commercial applications.

Among the processes which have been developed for the production of 2D materials, liquid-phase exfoliation (LPE) is positioned as one of the most promising methodologies for the industrial scaling up. Liquid-phase exfoliation is a top down process by which bulk crystals of layered materials are exfoliated to obtain liquid dispersions of exfoliated 2D crystals. Besides the large production volumes, another advantage of the LPE is that the 2D crystals dispersions can be used as the base for

functional inks and pastes that can be deposited on different substrates following many strategies, such as drop and dip casting, rod and spray coating, screen and ink-jet printing and other techniques.

The combination of specifically designed 2D material-based inks with commercially available deposition techniques (screen printing and spray coating) has been the core of my thesis work, aiming at the realization of printed integrated electronic devices for wireless sensing. In fact, the growing demand for interconnected systems in the era of the Internet of Things (IoT) is leading to widespread use of wireless components for remote sensing of environmental parameters. For this purpose, I investigated three type of devices related to fundamental functions of a wireless sensor, which are an antenna for wireless communication, a supercapacitor for energy storage and a photodetector as the sensing unit. Photodetectors are essential components of optoelectronic integrated circuits and fibre optic communication systems for applications ranging from communications to environmental monitoring and surveillance. In view of the implementation of a robust integrated system on flexible substrates that can withstand mechanical stresses, it is advantageous to use ultra-wideband antennas, which can maintain their performance even after bending. Finally, supercapacitors are chosen due to their ability to be charged and discharged almost instantly and their longer life compared to electrochemical cells, providing an efficient solution for the energy needs of the wireless system.

From the point of view of the materials properties, the antenna component requires a material with a high electrical conductivity, while supercapacitors need electrodes with both good electrical conduction and high active area. Monolayer and few layer graphene are considered among the best electrical conductors. With a conductivity of $\sigma \approx 4.9\ 10^8$ S m^{-1} in the monolayer, coupled with 97.7% optical transparency, and a specific area of 2630 $m^2\ g^{-1}$, graphene represents a promising conductive material for antennas and electrodes for supercapacitors.

On the other hand, the photodetector is based on a semiconductor which can efficiently absorb light and generate charge carriers with high mobility. Two dimensional indium selenide (2D-InSe), a layered semiconductors of the IIIA−VIA group, has emerged as a promising candidate for the realization of thin-film field effect transistors (FETs) and photodetectors due to its high intrinsic mobility ($> 10^2$ $cm^2\ V^{-1}\ s^{-1}$) and the direct optical transitions in an energy range suitable for visible and near-infrared (NIR) light detection.

Both graphene and InSe have been successfully exfoliated by LPE and used for the formulation of printable functional inks and pastes that were used for the fabrication of the antennas, supercapacitor and photodetector components. By testing the single components, we demonstrated the effective printing of graphene-based antennas with an ultra-wide band behaviour (fractional band 45%) centred at 2 GHz. In addition, the screen-printed supercapacitor has shown high-rate performance (areal

capacitance up to 1.324 mF cm^{-2}, voltage scan rate > 10 V s^{-1} and charge/discharge current density up to 25 mA cm^{-2}). Finally, spray-coated InSe photodetectors have shown good photosensitive responsivity to visible and NIR (< 900 nm) light (maximum D* ~ 5.49 10^{12} Jones, R_{ph} ~ 274 A W^{-1} @ 455 nm illumination) and fast response time (τ_R ~15 ms, τ_F ~64 ms). In conclusion, by using different 2D materials, the printing of high-performance components for the realization of a wireless system has been achieved, revealing the great potential of 2D materials in electronic applications.

In detail, the Thesis is organized as follow:

In the first four chapters, I will introduce the main properties of the 2D materials, the production strategies and their characterization.

In **Chapter 1** is given a brief overview of the main classes of 2D materials. The properties of these materials are discussed as well as the resultant applications owing to these properties.

In **Chapter 2** are outlined the exfoliation processes, in particular, the liquid phase exfoliation method and its challenges, as well as covering the formulation of inks and their optimization.

In **Chapter 3**, I will discuss the sample preparation methods and the characterisation tools used in this Thesis. An overview will be provided for each characterization method, outlining the respective measurement parameters.

From Chapter 4 to Chapter 7, I will explore the basic theory of electromagnetic and power supply devices.

In particular, in **Chapter 4**, I will describe the key features and the radio frequency characterization of the antennas.

In **Chapter 5**, I will discuss about the energy storage systems for wireless applications and their figure of merits including their strengths and drawbacks.

Chapter 6 will provide an overview of the characterization and measurement of photodetectors.

In **Chapter 7**, I will present an overview on the manufacturing techniques of the devices used in this thesis work. In particular, the deposition/coating strategies will be briefly introduced (*i.e.*, the spray coating, ink-jet printing and screen-printing techniques).

The last four chapters are dedicated to the results obtained in the three years of Doctoral activity.

Chapter 8 provides a summary of the engineering and characterization of the inks, starting from the strategies used in the exfoliation of pristine crystals.

In **Chapter 9** I will discuss the design of printed bow-tie antennas, their realization and morphological and electrical characterization.

In **Chapter 10** I will discuss the design of InSe photodetectors, their implementation and the characterization of the device.

Finally, **Chapter 11** concerns the design, manufacture and characterization of graphene-based supercapacitors and their application in the context of an integrated wireless system.

In the conclusions section, the main results of this thesis are summarized, and future developments of this research project are suggested.

1 STRUCTURE AND PROPERTIES OF 2D MATERIALS

The isolation of monolayer graphene flakes by mechanical exfoliation of bulk graphite opened the field of two-dimensional (2D) layered materials [1], [2]. Layered materials are composed of stacked nanometer-thick crystalline sheets, which are weakly bound by electrostatic, van der Waals, or hydrogen-bonding interactions [3]. Those crystals with atomic thickness, are nowadays at the centre of an ever-growing research effort due to their unique physical and chemical properties, often superior with respect their bulk three-dimensional counterparts, interesting for both fundamental science and applications [4], [5]. In view of the success obtained in the search for graphene layers, the ideas and methodology learnt in these studies have been extended to other layered materials, opening new horizons to a whole new variety of possibilities beyond the limited current applicability of graphene. In fact, after the graphene discover, many other 2D materials have been exfoliated, such as transition metal-dichalcogenides (TMDs, e.g., MoS_2, WSe_2) [6], hexagonal boron-nitride (h-BN) [6], and other 2D semiconductors of the IIIA-VIA group (e.g., InSe, GaSe, GaS) [6]. The family of 2D materials offers a full spectrum of physical properties, from conducting graphene [3] and semiconducting MoS_2 [7] to insulating h-BN [8] and more recently ferromagnetism and exotic electronic states, including topological insulators and Weyl semimetals [9].

1.1 Graphene

Graphene is the name given to a flat monolayer of carbon atoms in hexagonal structure and is the basic building block for graphitic materials of other dimensionalities as is schematized in Figure 1 [10]. Indeed, graphene can be wrapped up into (0D) fullerenes, rolled into (1D) nanotubes or stacked into (3D) graphite. The fullerene is a carbon-based material composed by hexagonal and pentagonal carbon rings that give it the spheroid structure [11]. Graphene sheets can also be rolled into a chiral angle, obtaining carbon nanotubes (CNTs). They have a cylindrical structure with interesting properties for electronics, optics, chemistry and materials science applications [12]. In particular, due to their thermal conductivity (2000-6000 W m^{-1} K^{-1}) [13], [14], mechanical (Young's modulus between 270 to 950 GPa and tensile strength of 11 - 63 GPa) and electrical properties [15], CNTs find applications as additives in many structured materials (i.e., carbon nanotube reinforced polyurethane applied for wind blades) [16]. The combination of the graphene rolling angle and the diameter, determine the CNT electronic properties; i.e., whether it is a metal or a semiconductor [17].

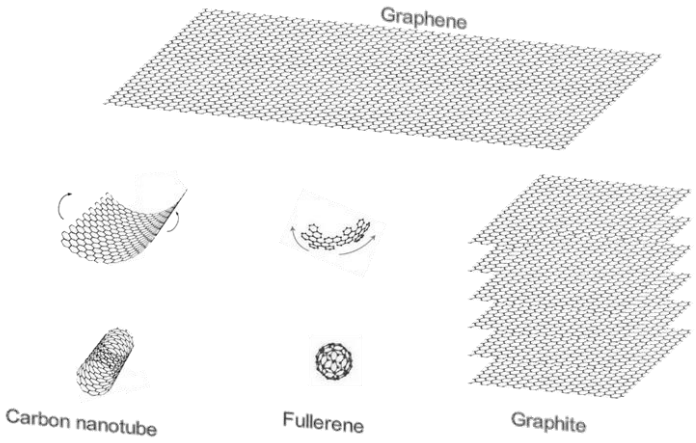

Figure 1 - Carbon allotropes.

Additionally, CNTs are categorized as single-walled nanotubes (SWNTs) and multi-walled nanotubes (MWNTs), the latter consists in multiple rolled layers (concentric tubes) of graphene [18]. The 3D counterpart of graphene is the graphite. It is a semimetal and is found in nature as a mineral and is the most stable form of carbon under standard conditions of temperature and pressure. Graphite has a layered, planar structure in which each plane is a graphene layer; the distance between the planes in graphite is 0.335 nm [19]–[21].

1.1.1 Graphene properties

The reason why graphite crystals can be exfoliated into individual sheets depends on the atomic bonding within the crystal. This consists of sp^2 hybridised carbon atoms, a hybrid orbital of the 2s and $2p_x$ and $2p_y$ orbitals [22]. As a result, graphite is covalently bonded in plane with a bond angle of 120 degrees [22]. These sheets are stacked in an AB configuration (Bernal stacking) [22] seen in Figure 1. Sheets are bound together by van der Waals interactions of the $2p_z$ orbitals to their neighbouring sheets [22]. Exfoliation of these materials is possible because the bounding forces are relatively weak (cleavage energy: 0.39 ± 0.02 J m^{-2} for ABAB graphite stacking) [23]. In this way sheets of graphene can be exfoliated while their lateral size is mostly preserved [23]. Graphene earns its interest with a long list of physical properties surpassing those obtained for any other material and far superior to its unexfoliated parent crystal [23]. Its electrical properties, due to its band structure, has caught interest of the scientific community since its discovery [3]. With an electron mobility [24] of 2.5×10^5 cm^2 V^{-1} s^{-1}, capable of sustaining extremely high current densities, 10^6 times that of

copper [25]. It exhibits several novel properties including room temperature quantum Hall Effect [26], [27]. The strong and anisotropic bonding of the carbon atoms gives graphene unique thermal properties with thermal conductivity ranging from 4800 to 6000 W m^{-1} K^{-1} [28], [29]. Graphene thermal properties play a crucial role in the performance of (opto)electronic devices [30]. In fact, the amount of heat generated during the device operation affects the energy consumption of electronic and photonic devices [31]. Also in the case of graphene film deposited on SiO_2, the thermal conductivity is about 600 W m^{-1} K^{-1} [32], rendering it one of the most promising material for heat dissipation applications [33]. As far as graphene optical properties are concerned, even if graphene is a single atom thick material [34], it is visible at the optical microscope [35] and its transmittance (T) can be expressed in terms of the fine-structure constant[35]. The absorption spectrum of graphene is quite flat from infrared (IR) to the visible range, having a peak at ~ 270 nm, due to the exciton-shifted van Hove singularity in the density of states [36]. In few-layer graphene (FLG), other absorption features can be seen at lower energies, attributable to inter-band electronic transition to the unoccupied π^* states [37]. The theoretical transmittance of a freestanding graphene can be derived by applying Fresnel equations, in the thin film limit, for a material with a fixed universal optical conductance [37] $G_0 = e^2/4\,\hbar \approx 6.08 \times 10^{-5}\,\Omega^{-1}$, to give:

$$T = (1 + 0.5\,\pi\,\alpha)^{-2} \approx 1 - \pi\alpha \approx 97.7\% \qquad \text{Eq. 1}$$

where $\alpha = e^2/(4\pi_0\,\hbar c) = G_0/(\pi_0\,c) \approx 1/137$ is the fine-structure constant [35]. The absorbance can be calculated as $A = 2 - \log_{10}(\%T) = \pi\alpha = 2.3\%$. Graphene only reflects < 0.1 % of the incident light in the visible region [35]. Graphene also possesses unique mechanical properties. Despite it is harder than diamond and stronger (~ 200 times) than steel [38], it is also highly stretchable (up to 20%) [39]. Combined with its robust physical properties, its highly favourable electrical properties make graphene a very attractive option as a transparent conductive coating in electronics, particularly for flexible electronic devices [40].

1.2 Transitional Metal Dichalcogenides

Transition metal dichalcogenides (TMDs) is a family of compounds having the formula MX_2, in which M is a transition metal and X is a chalcogen atom. Depending on the arrangement of the atoms, the structures of 2D TMDs can be categorized as trigonal prismatic (hexagonal, H), octahedral (tetragonal, T) and their distorted phase (T′) as shown in Figure 2 [41].

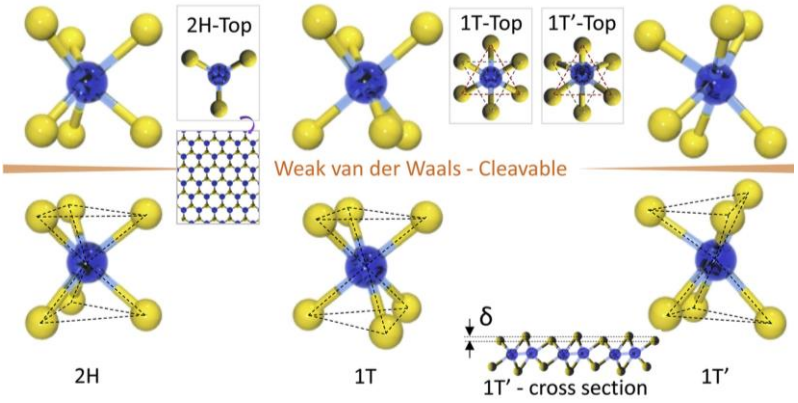

Figure 2 - Typical structures of layered transition metal dichalcogenides. Cleavable 2H, 1T and 1T' structures in layered TMD are shown [41].

In literature are present more than 40 types of TMDs depending on the combination of chalcogen and transition metal (Figure 3) [42], [43]. Additionally, depending on the coordination and oxidation state of the metal atoms, the doping of the lattice, or the crystal phase, TMDs can be metallic ($NbSe_2$ and TaS_2) [43], semimetallic (WTe_2) [44], or semiconducting (MoS_2 and WS_2 – for the 2H phase) [42], [43]. The structure and properties such as charge density wave (CDW), magnetism (ferromagnetic and anti-ferromagnetic), and superconductivity of 2D TMDs are summarized in Figure 3 [41].

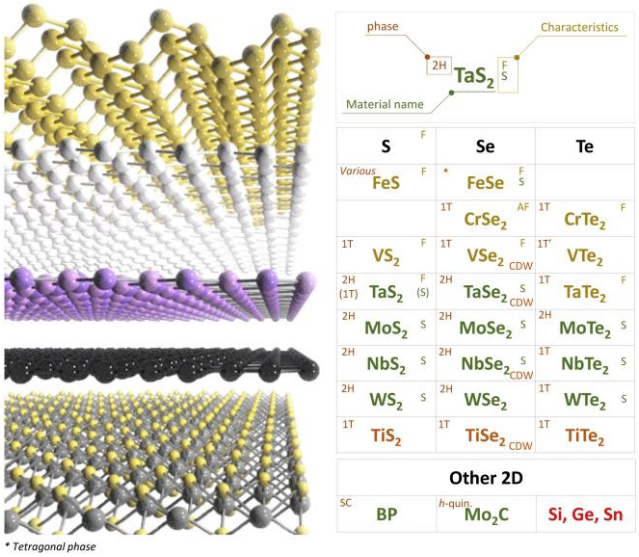

Figure 3 - Table for several 2D TMDs and other 2D materials exhibiting various physical properties such as magnetism (ferromagnetic (F)/anti-ferromagnetic (AF)), superconductivity (s) and charge density wave (CDW) and crystal structures (2H, 1T) [41].

1.2.1 TMD Monolayer Properties

TMDs, as already addressed for graphene, are bound strongly in plane while the layers only bound to each other by van der Waals interactions. In this way, the bulk crystals can be exfoliated into monolayer or few layer platelets [41]. Exfoliation of these materials allows to increase the surface area of exfoliated flakes being beneficial for catalysis of the hydrogen evolution reaction. [45], [46] 2D TMDs exhibit interesting electrical and optical properties as well. This is a result of quantum confinement effects due to restricting the wave function to two dimensions [47], appearing during the crossover from an indirect bandgap to a direct bandgap when bulk materials are exfoliated to monolayers [41]. Strong photoluminescence (PL), large exciton binding energy, and tuneable bandgap in TMDs make them promising candidate for a large variety of opto-electronic devices, including solar cells, photo-detectors, light-emitting diodes, and photo-transistors [41], [48]–[51]. For example, unique properties of monolayer MoS_2 include direct bandgap (~ 1.8 eV), good mobility (~ 700 $cm^2\ V^{-1}\ s^{-1}$), high current on/off ratio of ~ 10^7–10^8, large optical absorption (~ $10^7\ m^{-1}$ in the visible range) and a giant PL arising from the direct bandgap (1.8 eV) in monolayer; thus, it has been studied widely for electronics and optoelectronics applications [7],[41].

1.3 IIIA-VIA group layered semiconductors

The class of IIIA–VIA layered semiconductors generally have the chemical formula MX, where e.g., M = Ga/In (Group IIIA) and X = S/Se/Te (Group VIA) [52], [53]. As with TMDs, IIIA–VIA layered semiconductors also have strong in-plane covalent bonding and weak out-of-plane van der Waals interactions [54]–[56]. Over the last few decades, much progress has been made in the synthesis of such materials, leading to the development of methods such as chemical vapor deposition (CVD) using various precursors, [57] the Bridgman method, [58], [59] plasma discharge of precursors, [60] electrodeposition [61] and chemical reduction [62] for the fabrication of IIIA–VIA layered semiconductors. In recent years, investigations into the properties of nanometrically thin flakes of such layered materials have been conducted [63]–[68].

1.3.1 Properties

GaSe and InSe are two representative compounds of the family of IIIA–VIA layered materials. The GaSe crystal displays a layered hexagonal structure (space group P_{6m2}), in which each layer consists

of GaSe sheets bonded in the sequence Se–Ga–Ga–Se; each Ga atom is tetragonally bonded to one Ga atom and three Se atoms, while each Se atom is trigonally bonded to three Ga atoms [56], [69]. On the other hand, InSe exhibits three highly distinct polytypes [56], [70], [71] (β, ε, and γ) [53], in which InSe layers are differently arranged. The β (space group symmetry D_{46h}) and ε polytypes (space group symmetry D_{13h}) are characterized by a hexagonal lattice consisting of eight atoms in the unit cell, and their extension over two layers [72]. Rhombohedral γ polytype (space group symmetry C_{53v}) contains two cations and two anions distributed on four adjacent layers [71], [73]. InSe is made of stacked layers of Se-In-In-Se atoms with van der Waals bonding between quadruple layers [74], [75].

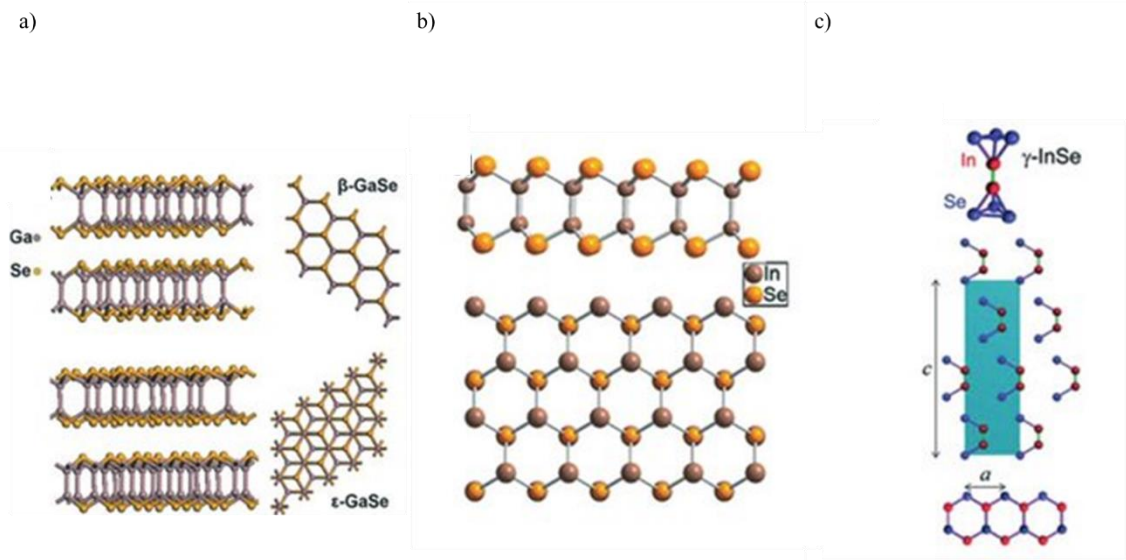

Figure 4 - Crystal structures of typical IIIA-VIA 2DLMs: a) GaSe crystal structure: side view and top view for β-and ε-GaSe; both β-and ε-GaSe show 2H stacking [76]. b) β-InSe crystal structure: the top is the side view of the InSe lattice structure, and the bottom shows the top view of the InSe crystal structure [77]. c) Scheme of γ-InSe crystal structure: the lattice constant along the c-axis is 24.961 Å; within each plane, atoms form hexagons with a lattice parameter of 4.002 Å [78].

While ε-InSe has an indirect band gap of 1.4 eV [71], both β- and γ-InSe have a direct band gap [71] with closely matching values (1.28 eV [72] and 1.29 eV [79], respectively). Accordingly, only β and γ phases of InSe could supposedly be employed in optoelectronics, for which finite and direct band gaps are beneficial [80]. Exfoliated samples of γ-InSe host quantization effects, which enable near-infrared photoluminescence emission [78]. As a result of their optical and electronic attributes, coupled with semiconducting properties which are similar to those of TMDMs such as MoS_2 and WS_2, they are often explored for use as electrical sensors, and photoelectric and nonlinear optical devices [81]–[83].

2 PRODUCTION AND PROCESSING OF 2D MATERIALS

A 2D material can be produced by using many techniques that may be clustered into two main groups: the top down and the bottom up approaches (some techniques are showed in Figure 5) [4], [84], [85]. In the top down approach, the 3D bulk material is exfoliated layer by layer to obtain the related 2D material. Within this group there are several techniques, to name a few:

- micro mechanical cleavage (MC) (Figure 5a);
- anodic bonding;
- photoexfoliation;
- liquid phase exfoliation (LPE) (Figure 5b).

In contrast, the bottom-up approach consists in bonding together the atoms in order to obtain the related 2D material on top of a substrate, which is carried out by exploiting several techniques, amongst them, a few are listed below:

- precipitation from metals;
- chemical vapour deposition (CVD) (Figure 5c);
- molecular beam epitaxy (MBE);
- chemical synthesis.

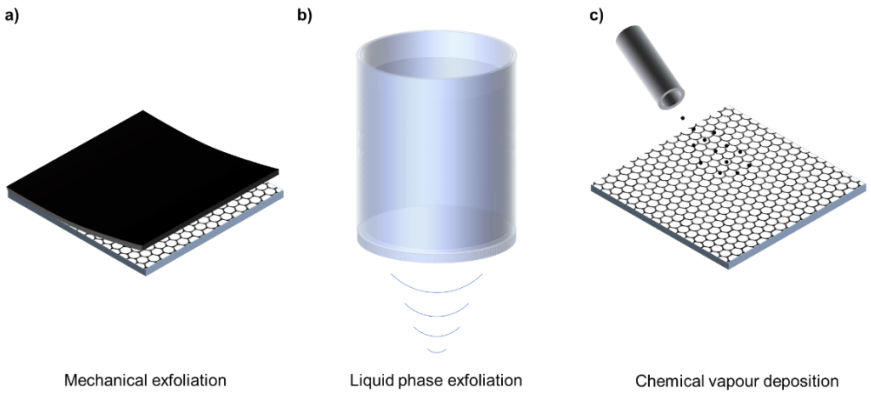

Figure 5 - Schematic illustration of some production techniques. a) Micromechanical cleavage. b) Liquid phase exfoliation c) Chemical vapour deposition.

2.1 Micromechanical cleavage

Micromechanical cleavage (MC) was the method used in 2004 by the Nobel Laureates A. K. Geim and K.S. Novoselov to isolate of graphene for the first time [86]. Exfoliation of graphite has been known from crystallographers since the 16th century, and it can be "roughly" associated to the process that occurs when a pencil is pressed against a sheet of paper during writing [3], [34], [87]. MC method is very simple and involves the peeling off a piece of graphite by means of adhesive tape (Figure 6). The method has been optimized over the years to produce graphene of up to millimeters in lateral size [88], [89].

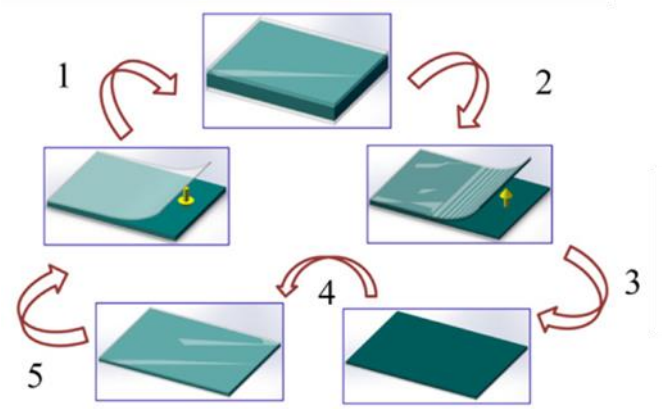

Figure 6 - The process of mechanical exfoliation method [90].

The processed material can then be transferred onto the surface of a substrate [91]. The number of layers can be readily identified by elastic (Rayleigh) [92] and inelastic (Raman) [93], [94] light scattering. Rayleigh scattering intensity has a very strong dependence on the size of the particles (it is proportional to the third power of their diameter) [92] and is inversely proportional to the fourth power of the wavelength of light, which means that the shorter wavelengths in visible white light are scattered stronger than the longer wavelengths toward the red end of the visible spectrum [92]. Contrast spectroscopy of layers on a 300 nm thick SiO_2 was done and results revealed that single layer graphene (SLG) is visible by optical microscopy [92]. Although MC is the standard approach for fundamental research due to the high structural and electronic quality of the flakes, it has disadvantages in terms of yield, being impractical for large-scale applications [88].

2.2 Liquid phase exfoliation

Despite MC remains the source of the highest-quality graphene samples available [95], it suffers from low yield and a production rate that is not technologically scalable in its current form [42]. One possible solution is the exfoliation of layered compounds in liquids to give large quantities of dispersed nanosheets [40], [42], [96]. This should allow for methods to obtain sizable quantities of 2D materials that can be processed by using existing industrial techniques, such as reel-to-reel manufacturing [42]. There are several liquid exfoliation techniques for layered materials, among them in this section, I briefly outline the Sonication-assisted exfoliation and the Wet-Jet milling exfoliation techniques.

In general, the Liquid phase exfoliation essentially consists of three steps (Figure 7):

1 the dispersion of the layered material (in this specific case graphite) in an appropriate solvent;

2 the exfoliation process by a driving force;

3 the purification;

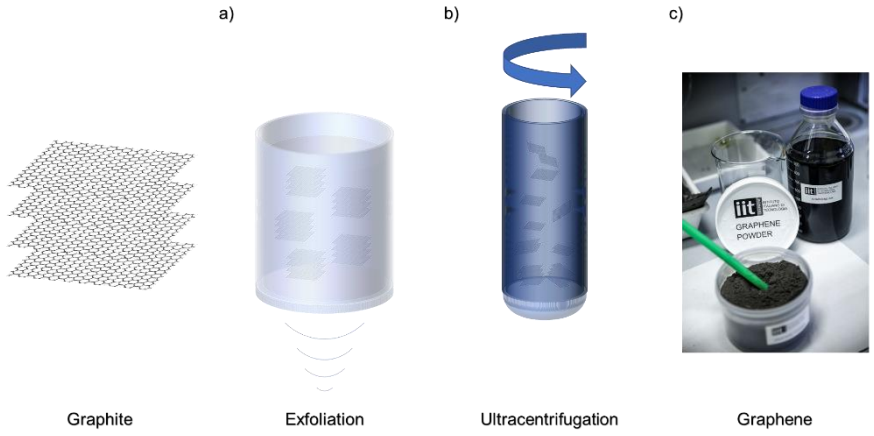

Figure 7 - Different steps of LPE: the starting material is pristine graphite; after the dispersion in the solvent, the following step is a) the exfoliation b) purification via ultracentrifugation. c) Following the procedure, a graphene dispersion is obtained.

2.2.1 Dispersion

The selection of the solvent plays a central role in the exfoliation process [88]. For this reason, the surface tension (γ), the Hansen (or Hildebrand) parameters and the viscosity (η), are pivotal constraints in the choice of the solvent [97]. Stable dispersions can be achieved minimizing mixing

Gibbs free energy ΔG_{mix}. For simplicity, the exfoliation in solvent can be viewed as simply a mixture of two species. The thermodynamic physics of mixtures has been well studied since the XIX century. In a mixture of two substances there is a change in entropy (S) and depending on the interactions between the two species there is a corresponding change in enthalpy (H) for the whole system; with the system that includes both species before mixing and the total mixture after mixing. In general ΔG_{mix} of two materials can be described under isothermal conditions, by [97]:

$$\Delta G_{mix} = \Delta H_{mix} - T\Delta S_{mix} \qquad \text{Eq. 2}$$

where ΔH_{mix} and ΔS_{mix} are the change in enthalpy and entropy involved in the mixing process, respectively [97]. Being $\Delta S_{mix} > 0$ (the mixing of two substances increase the disorder of the system) ΔH_{mix} must be positive and not too large in order to satisfy the Eq.2. This means that in order to produce a stable dispersion the enthalpy of mixing must be minimised. In terms of solubility, for these materials to be soluble the process needs to be energetically favourable i.e., $\Delta G_{mix} \leq 0$. Solvents whose surface tension is very close to graphene surface energy value ($\gamma \approx 46.7$ mN m^{-1}) satisfy this requirement [97]. Extensive experiments have demonstrated that in the case of graphene, the best value for the surface tension is about $\gamma \approx 40 - 50$ mN m^{-1}, and the best candidates for stable dispersions are N-Methyl-2-pyrrolidone (NMP), Dimethylformamide (DMF) and benzyl benzoate [4], [84], [97], [98]. The exfoliation using the aforementioned solvents has been demonstrated also in many other layered materials [42]. However, most of these solvents are toxic and hard to remove, once deposited onto a substrate, due to high boiling points, over than 450 K [99]. This is a critical issue when the inks must be used for the deposition on plastic substrates, such as polyethylene terephthalate (PET), polyethylene naphthalate (PEN). A possible solution to this issue relies on the tuning of the rheological parameters of lower boiling point solvents, such as acetone [100] and isopropanol [101]. A problem with acetone and IPA is usually that the surface tension of these solvents is low ($\gamma \sim 25$ mN m^{-1}) and the concentration of the dispersed graphene flakes in the as-obtained inks is far too low [101], with respect to the one obtained with solvents such as NMP, i.e. ~ 0.3 g L^{-1} [98]. If the surface tension of the solvent is too high, with respect to the surface energy of graphite, the exfoliation and the following dispersion is ineffective. In fact, dispersions of graphitic materials in water is impractical because of the high surface tension ($\gamma \approx 72$ mN m^{-1}). The use of surfactants (such as sodium dodecylbenzene sulfonate, SDBS) is a solution largely explored in literature [97]. Additionally, bile salts (such as sodium cholate, SC, or sodium deoxycholate, SDC) or polymers (such as pluronic) [4], [97], [102] have been extensively used as well. The disadvantage of using the surfactants and polymers relies on the fact that their presence prevents the electric contact between

graphitic or graphene flakes, with a degradation of the overall electrical properties [88] and this is detrimental in electronic applications (i.e., the fabrication of transparent conductive film). However, the presence of the surfactant/polymer molecules is not an issue for other types of applications (i.e., the realization of polymer composites) [40]. Consequently, the use of surfactants/polymers strictly depends on the target application. Research efforts have been driven by the exploitation of co-solvency effect in which the dispersibility of layered materials can be greatly improved by using a mixture of solvents [98], [103], [104], *e.g.*, water/isopropyl alcohol [105], water/ethanol [98], etc. By fine-tuning the relative concentration of the co-solvents, it is possible to adjust the rheological properties (*i.e.*, density, viscosity, and surface tension) [98], [106] of the mixture "on demand". Nevertheless, the use of co-solvent mixtures, mostly based on alcohols and water, for the dispersion and exfoliation of graphite and other inorganic layers materials has some drawbacks. The quality of the dispersion, that can be defined as the ratio of the number single layer flakes with respect to thicker flakes and the maximum concentration achievable by the exfoliation process in such co-solvent mixtures [98] is currently much lower with respect to the ones achieved in NMP [107] and water-surfactant dispersions [108]. Furthermore, the surface tension is very sensitive to solvent evaporation [5], [85] and all the rheological properties of alcohol-based co-solvents are temperature dependent [109], affecting the long-term stability of the dispersions.

2.2.2 Exfoliation Process

The exfoliation of layered materials in a liquid medium can be carried on by applying an external driving force such as ultrasonication, [110] high-shear mixing, [111], [112] ball milling, [113], [114] wet jet milling [115] and microfluidization [116]. In the following section, ultrasonication and wet jet milling techniques will be presented.

2.2.2.1 Ultrasonication

In the ultrasonication technique, a layered crystal is dipped into the solvent and then soaked in a sonic bath that provides ultrasound vibrations, which are then transmitted to the sample. Cavitation is the main phenomenon involved in the exfoliation of layered materials by ultrasonication [95]: as a result of collapsing cavitation bubbles, tensile and shear stresses act on the nanomaterial leading to both exfoliation and fragmentation [40], [117]. The ultrasonication process can be carried out using either sonic baths [88], [95] or tip ultrasonicators [40], [88]. In bath sonication, the ultrasonic waves

propagate through both reaction container and tank, setting up a standing wave [88], [95]. The intensities of the ultrasonic waves acting on the sample are lower than nominally expected and their non-uniform distribution through the tank can result in poor reproducibility of the ultrasonication process [40]. High-power sonic probes can also be used [88]. In this case, the sonotrode is directly immersed in the solution resulting in a much more intense ultrasonication [118]. In this configuration, the exfoliation of the layered materials is dependent not only on sonic power, amplitude and frequency, but also on sonic probe type and container shape. The main limitation of ultrasonication is the poor reproducibility and, above all, the exfoliation is intrinsically linked to the fragmentation of the material [117]. In addition the time required to obtain 1 g of exfoliated material (t_{1gram}), the volume of solvent required to produce 1 g of exfoliated material, (V_{1gram}), as well as the ratio between the weight of the final graphitic material and the weight of the starting graphite flakes, defined as exfoliation yield (Y), are still insufficient for industrial scale productions [115], [119]. For example, in the case of graphene, after more than 35 h of sonication and several steps of sonication and re-dispersion, the concentration of the processed material can reach up to 60 g L^{-1}, which means t_{1gram} > 1800 min and V_{1gram} = 0.53 L) and a Y of 19% [115], [119]. For a 6 h of sonication, the following results have been attained: t_{1gram} > 180 min, V_{1gram} = 3.3 L and Y_W = 3% [115], [119].

2.2.2.2 Wet Jet Milling

In view of addressing the drawbacks presented by the ultrasonication technique, our group has developed a new scalable approach, the wet jet milling technique (WJM) [115]. With WJM technique is possible to exfoliate layered crystals (i.e., graphite, hexagonal-boron nitride, and transition metal dichalcogenides) with high throughput and weight-yield, resulting in the cost-effective production of the 2D crystals without compromising the crystalline-integrity [115]. The process is based on high-pressure WJM, with a production capability of 2 L h^{-1} [115]. A concentration of 10 g L^{-1} is achieved for both single- and few-layer 2D crystal flakes dispersion, making the scaling-up more affordable [115]. A hydraulic mechanism (Figure 8) and a piston supply the pressure (up to 250 MPa) in order to push the sample into a set of 5 different perforated and interconnected disks, named the processor, where jet streams are generated [115]. The pulverization is obtained mainly by colliding the pressurised streams of the particle liquid dispersions [115]. The WJM process enables the production of defect-free and high quality 2D-crystal dispersions on a large scale, opening the way for their full exploitation in different commercial applications [115]. In the case of graphene, the WJM exfoliation process comprises a first step of preparing a dispersion of graphite powder in NMP as dispersant solvent, and a subsequent step of exfoliating the aforesaid dispersion during its exposure to the

hydrodynamic forces generated through high-pressure (180–250 MPa) compression of the dispersant fluid phase through nozzles with different sizes (between 0.1-0.3 mm⌀) [115], [119]. By decreasing the size of the nozzle it is possible to obtain thinner and smaller lateral size flakes [115], [119].

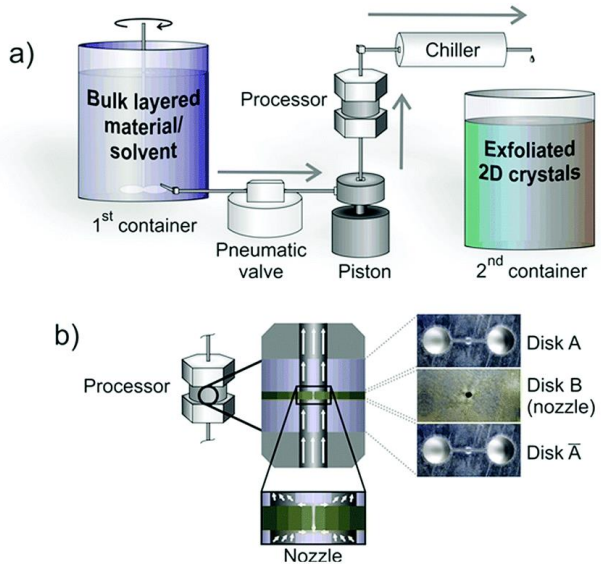

Figure 8 - Scheme of the wet-jet mill system [115].

Immediately after, the sample is cooled down in form of a liquid dispersion by means of a chiller [115], [119]. Actually, WJM exfoliation is a pulverization technique that allows large volumes (litre-scale) of concentrated high quality (single-/few-layers graphene) graphene dispersions (gram per litre-scale) in short times (second-scale) to be obtained [115], [119]. For instance, we achieved t_{1gram} = 2.55 min and V_{1gram} = 0.1 L, with Y_W of ~100 %.

2.2.3 Purification

The purification is the last step in the LPE process. Here, exfoliated layered crystals flakes are separated from un-exfoliated bulk [107], [118]. During the exfoliation process, bulk and layered materials are mixed together in a heterogeneous composition ranging from un-exfoliated and thick flakes, to thin flakes, few and single layer. The as-produced flakes have also a wide lateral size distribution. Hence, the control of morphological properties is of fundamental importance in consideration of the optimization and scalability of the LPE process [40], [88]. Different strategies can be considered in the purification process of the as-obtained exfoliated materials. One approach

can be the sedimentation based-separation (SBS) process [105] in a uniform medium [120], [121], while another approach can be the density gradient ultracentrifugation (DGU) [122] in a density gradient medium (DGM) [122]. In SBS, particles are separated based on their sedimentation rate [120], [121] in response to a centrifugal force acting on them. Currently, SBS is the most common separation method, obtaining flakes ranging from few nanometers to a few microns, both for graphene and other inorganic 2D crystals [88]. In general, the sedimentation rate of dispersed nanomaterials subjected to a centrifugal field is ruled by the Svedberg equation [120], [121]:

$$s = m(1 - \rho\upsilon')/f \qquad \text{Eq. 3}$$

In this equation, *s* represents the sedimentation coefficient, the time needed for the nanomaterial to sediment, commonly reported in Svedberg (*S*) unit (1 *S* corresponds to 10^{-13} s), [120], [121]. *m* is the mass, υ′ is the volume of each gram of the flakes in solution, ρ is the density of the solvent, while *f* is the frictional coefficient [120], [121]. In the case of 2D crystals, *f* depends on both the lateral size and thickness of the 2D flakes and the viscosity (η) of the solvent in which they are dispersed []. Overall, *s* depends on the morphological properties of the dispersed nanomaterials, being proportional to its buoyant effective molar weight and inversely proportional to *f* [123]. As expressed by the Svedberg equation, the sedimentation of 2D flakes depends on their mass and the frictional coefficient [120], [121]. Thick and large sheets, having larger mass, sediment faster with respect to small and thin sheets (having smaller mass), which are thus maintained in dispersion during the SBS process, see Figure 9. The composition of the suspended flakes principally depends on the η of the medium [96], therefore, since at room temperature NMP shows higher η (1.7 mPa · s) than water (1 mPa · s), sedimentation of heavier flakes during ultracentrifugation is more difficult, and the fraction of SLG on the total amount is lower in NMP than in water [96]. Following SBS, concentrations of up to ~ 60 mg ml^{-1} for graphitic flakes have been demonstrated [105], [124]. The SBS yield is only related to the lateral sizes of the flakes. Control on the number of layers can be obtained by DGU, where nanomaterials in dispersion are ultra-centrifuged in a DGM [40].

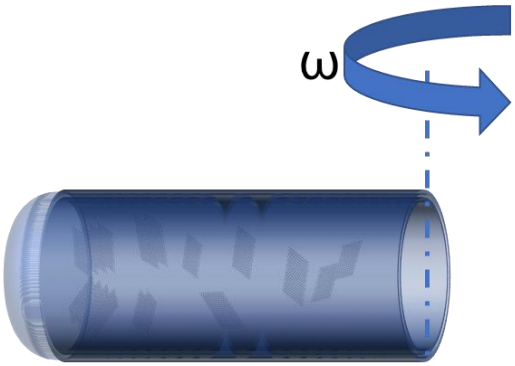

Figure 9 - Forces acting on graphene flakes inside an ultracentrifuge tube during ultracentrifugation with a swinging bucket rotor.

During DGU process, the flakes are sorted along the ultracentrifuge tube, dragged by the centrifugal force, until they reach the corresponding isopycnic point, - the point where their buoyant density matches that of the surrounding DGM [40]. The uniform coverage of the flakes with surfactant molecules results in an increase of the buoyant density with the number of layers [40]. To date, up to ~ 80% SLG yield was reported by exploiting the isopycnic separation [40], [125]. Another method to sort layered materials is the rate zonal separation (RZS) [88], where, in a DGU process, the ultracentrifugation is stopped during the transient centrifugal regime, before the flakes (nanomaterials in general) arrive at their own isopycnic points [88]. Rate zonal separation exploits differences in the sedimentation coefficient of (nano)materials under ultracentrifugation [88]. Thus, flakes with different sedimentation coefficient values will travel along the ultracentrifuge tube at different sedimentation velocities, determining their spatial separation [88].

2.3 Chemical vapour deposition

Chemical Vapour Deposition (CVD) is an attractive bottom-up approach used not only to produce high structural quality 2D materials [88], [126]–[128] but also polycrystalline silicon [129], diamond [130] among others. A CVD furnace (Figure 10) is formed by a gas delivery system, which provides the path for the gas species to enter into the reactor, and in the case of graphene synthesis, methane is commonly used [131]. The amount of gas entering the chamber is controlled with valves, so that gas is uniformly mixed in a desired stoichiometric proportion before entering the reactor [131]. Inside the reactor, the main chemical reactions take place. On the substrates, thin solid films are consequently grown [132].

Figure 10 - Example of compact CVD furnace designed for growing several materials on substrates [133].

The chemical reactions need high temperatures (1000 K – 1300 K) generally provided by heaters surrounding the reactor [127]. Pressure, temperature, time of reaction as well as diffusion of the reactants' species are all parameters needed to be taken into account to optimize the growth process to obtain a homogenous deposition [127]. In the case of graphene, a thin metal substrate (Ni, Cu, Co, Fe, Ru), is needed as catalyst to decompose the impinging hydrocarbons [127]. In the thermal CVD process are present three steps [127]:

1 a heating step, performed under a gas flow (usually H_2 and/or Ar) or in vacuum, to anneal the catalyst surface, removing oxide layers grown on it;

2 a deposition step, in which the carbon precursor flows into the furnace and its molecules undergo a decomposition process near the catalytic surface, leaving C atoms free to diffuse inside the catalyst or on its surface;

3 a cooling-down step, in which the temperature is fast decreased down to room temperature, allowing for the nucleation of C atoms on the metallic substrate, later coalescing into larger clusters.

Carbon atoms, after decomposition from hydrocarbons, nucleate on Cu, and the nuclei grow into large domains [127]. The nuclei density is principally a function of T and pressure and, at low precursor pressure, mTorr, and T > 1000 °C, very large single crystal domains, ~ 0.5 mm, are observed [127]. Another CVD approach is the plasma assisted growth. The advantage of plasma methods with respect to thermal CVD, is the production of graphitic materials without metal catalyst over a wide range of growth conditions [127].

2.4 Solution processing of 2D materials

LPE is the ideal technique to produce functional inks that can be printed into low cost 2D-material-based devices. In this paragraph it is discussed the optimization processes in order to formulate the inks to be printed/deposited by different printing techniques (i.e., inkjet printing, screen printing and spray coating). The formulation and properties of graphene-based inks will be discussed in the framework of the state of the art of printable technologies, highlighting the role potentially played by 2D-based inks soon to boost the real application of these technologies.

2.4.1 Printable ink optimization

The dispersions of liquid-exfoliated flakes, discussed in the previous chapter, can be used as an ink in order to produce conductive patterns, devices or insulating layers [96], [134]. Deposition by spray and drop casting can be performed directly with the obtained dispersion, without complicated engineering operations [135]. However, in most cases, the as-produced dispersion itself cannot serve directly as inks and they need to be further processed by exploiting several coating and printing strategies [136]. Colloquially it is possible to classify the inks according their viscosity (η). The formulation of "liquid" (η ~ 10 cP [136]) inks is required in ink-jet printing while "pastes" with increasing viscosity (η ~ 10^3 cP [136]) are used in flexographic, slot-die, and screen-printing techniques [136]. In the case of 2D crystals, the variation of η is affected by the lateral size vs thickness ratio. In fact, the increase in contact area and surface interaction between the dispersed 2D sheets and the dispersion medium results in an increase in the η of the dispersion, compared to spherical nanoparticles counterpart [137]. Another critical parameter is the morphology control of the dispersed nanomaterials (*e.g.* 2D crystal flakes). Additives, such as rheology and γ-modifiers, play an important role in the study of morphology of the inks and are added to prevent aggregation and/or precipitation of the dispersed flakes (nanoparticles in general) and to obtain a good wetting of the substrate [96], [134] in order to guarantee the best performances in term of coating/printability [96], [134]. The composition of inks is functional to the type of coating/printing process, the type of substrate and the device one wants to obtain. Taking as example conductive inks, these are multi-component system containing (nano)materials as active component (i.e., nanoparticles -NPs-, conducting polymers, CNTs, graphene and other 2D materials [96], [134], [138]) dispersed in a liquid. Binders, solvents (either aqueous or organic) and additives change the electrical and mechanical

properties by varying contents of these additives (from 20% up to 80%) depending on the type of ink to be prepared [139].

In the case of inkjet printing technique (see Inkjet printing section at page 57), the realization of printable inks containing nanomaterials is very challenging. Liquid properties such as density (ρ), γ and η have a strong effect on the printing process [96]. The effect of these physical properties on the jettability of the ink can be summarized in a dimensionless figure of merit (FoM), the Z number, defined as follow:

$$Z = \frac{(a\rho\gamma)^{0.5}}{\nu} \qquad \text{Eq. 4}$$

where a reported in μm represents its diameter. In order to avoid printing instabilities, such as jetting deflection and satellite droplets [140] the Z number must be in the range between $1<Z<14$ that is a commonly accepted value for optimal printability [96]. However, other parameters for optimal printing must be tuned. Firstly, the morphological properties of the nanomaterials dispersed in the ink as well as the formation of aggregates in the ink and their subsequent accumulation on the print-head can determine printing instabilities [96]. Dispersed nanomaterials with lateral sizes smaller than ~1/50 of the nozzle diameter are usually required [88].

3 CHARACTERIZATION TECHNIQUES OF 2D MATERIALS

In this chapter, it is provided an overview of the experimental techniques that have been used in this thesis work. UV-Vis-NIR and Raman spectroscopy as well as transmission electron microscopy (TEM) for the characterization of the morphology of the 2D materials and rheological measurement for the study of the ink rheology. The experimental setups, which were used for the experiments, will be briefly introduced and illustrated.

3.1 Optical absorption spectroscopy

The interaction of light with matter is a process that has been under investigation for centuries [141]. The propagation of light from one medium to another with different refractive indices, leads to a bending of the beam as the speed of the traveling wave changes: this phenomenon is called refraction. Two main events happen when a light beam propagates through a liquid sample containing particles: the beam is partially scattered or absorbed by the particles [142]. The Beer-Lambert law [143] explains this variation in intensity. A reduction in intensity is proportional to the initial intensity before the beam interacted with the sample and is given by:

$$dI = -\beta I C(z) dz \qquad \text{Eq. 5}$$

The change in intensity (dI) is dependent upon the sample concentration (C), the path length (l), and a constant (β). The expression needs to be integrated for the length of the entire path length; therefore, it is possible to integrate the intensity (I) over the range from the initial to the final intensity:

$$\int_{I_0}^{I} \frac{dI}{I} = -\beta \int_{0}^{l} C(z) dz \qquad \text{Eq. 6}$$

which can be further simplified to:

$$\ln \frac{I}{I_0} = -\beta \int_0^l C(z)dz \qquad \text{Eq. 7}$$

Introducing a constant and change to base 10, the familiar form of Beer-Lambert equation is obtained:

$$A = \varepsilon \int_0^l C(z)dz \qquad \text{Eq. 8}$$

where:

A is the Absorbance defined as $A = -\log_{10}(I/I_0)$, ε, found experimentally, is the molar attenuation coefficient in the material sample, C is the concentration of the material sample; l is the path length of the beam of light through the material sample. The relative intensity attenuation is obtained by the difference of the attenuations obtained by the two measurements of blank solvent and the dispersion under investigation. Absorbance A is used to perform calculations. Samples are usually diluted to avoid possible scattering losses at concentrations higher than 0.01 g L^{-1}: given the ratio r of dilution between the original sample volume and the final volume after dilution (for example, r = 20 stands for 200 µL of ink diluted to 4 mL), concentration can be calculated as:

$$C = \frac{Ar}{\varepsilon l} \qquad \text{Eq. 9}$$

In order to evaluate the concentration of the LPE-produced ink, the absorption spectroscopy is a key characterization for the optimization of production techniques, especially in view of industrial-scale applications [123]. In fact, to develop good quality printed devices it is needed a graphene ink with concentration values around to 1 g L^{-1} is needed [144].

3.2 Raman spectroscopy

Raman spectroscopy is a technique based on inelastic scattering of monochromatic light, usually from a laser source, being one of the most important tools in the characterization of the different material allotropes [92], [93], [145], [146]. The photons impinging in a sample are absorbed by the sample itself and then re-emitted with the same or different frequency [147]. Most of the scattered light has the same frequency as the incident one and the process is called Rayleigh (elastic) scattering (see Figure 11). On the contrary, if the kinetic energy of photons is not conserved, the scattering process is called inelastic. In this condition, the scattered photons have a reduced or increased frequency, a process known as Raman scattering [145]. Contrary to Rayleigh scattering, Raman is very weak (~ 10^{-5} % of the incident beam). There are two different Raman scattering processes that can be distinguished, i.e., Stokes scattering, where the frequency of scattered light is reduced with respect to the incident one, due to the excitation of photons, and Anti-Stokes scattering, where the resulting frequency of the scattered light is increased (see Figure 11) [148] due to the dissipation of the thermal phonons in the crystal lattice, cooling the crystal during the process. These characteristic (Raman) shifts provide valuable information about vibrational, rotational and other low frequency changes in the samples. In the Raman spectrometer a light beam from the laser sources and it enters inside the optical system, where it is shaped, focused and transmitted through mirrors. Afterwards, the laser beam is reflected hitting the sample, whose surface can be observed with an optical microscope. Finally, the scattered beam is focused again into an entrance slit. A Charge-Coupled Device camera detects the resulting beam and performs photon counting, providing the Raman spectrum.

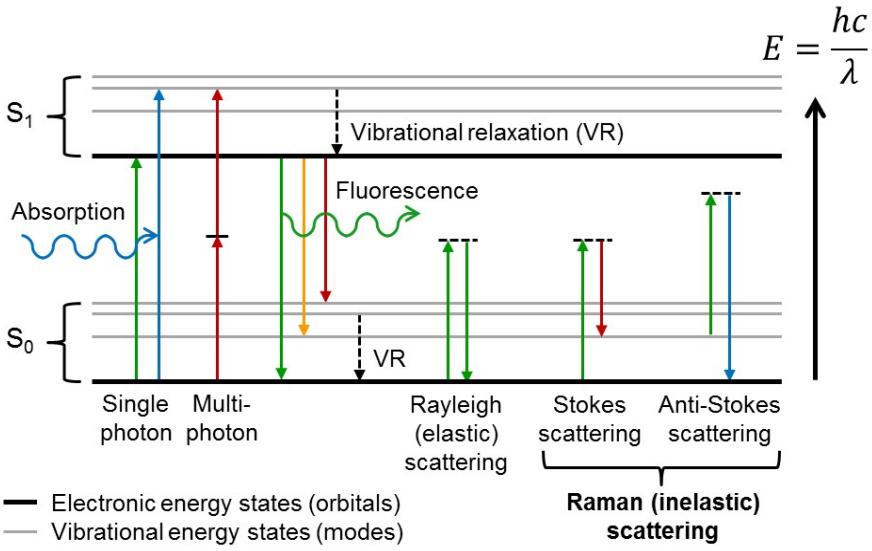

Figure 11 - Energy-level diagram showing the states involved in Raman spectra [149].

3.2.1 Graphene Raman spectroscopy analysis

Raman spectroscopy is an ideal tool for the investigation of different carbon–based materials ranging from sp^2- to sp^3- based ones. In fact, Raman spectroscopy can provide information on both the vibrational structure and on the electronic properties of investigated materials [145]. Moreover, it is a fast, reliable and nondestructive method that gives information on the structural quality of the investigated specimens. Each carbon (nano)materials has a clear fingerprint Raman spectrum, which allows the identification and study of different kinds of allotropes. In the specific case of graphene, the Raman signal not only demonstrates the changes in the electron bands but also provides useful information in order to determine the number of graphene layers [93]. In fact, the graphene vibrational properties are strictly dependent on the thickness of the flakes, which is in turn reflected in the characteristic spectral features [93]. The most characteristic Raman features of graphene are the so-called G and 2D modes.

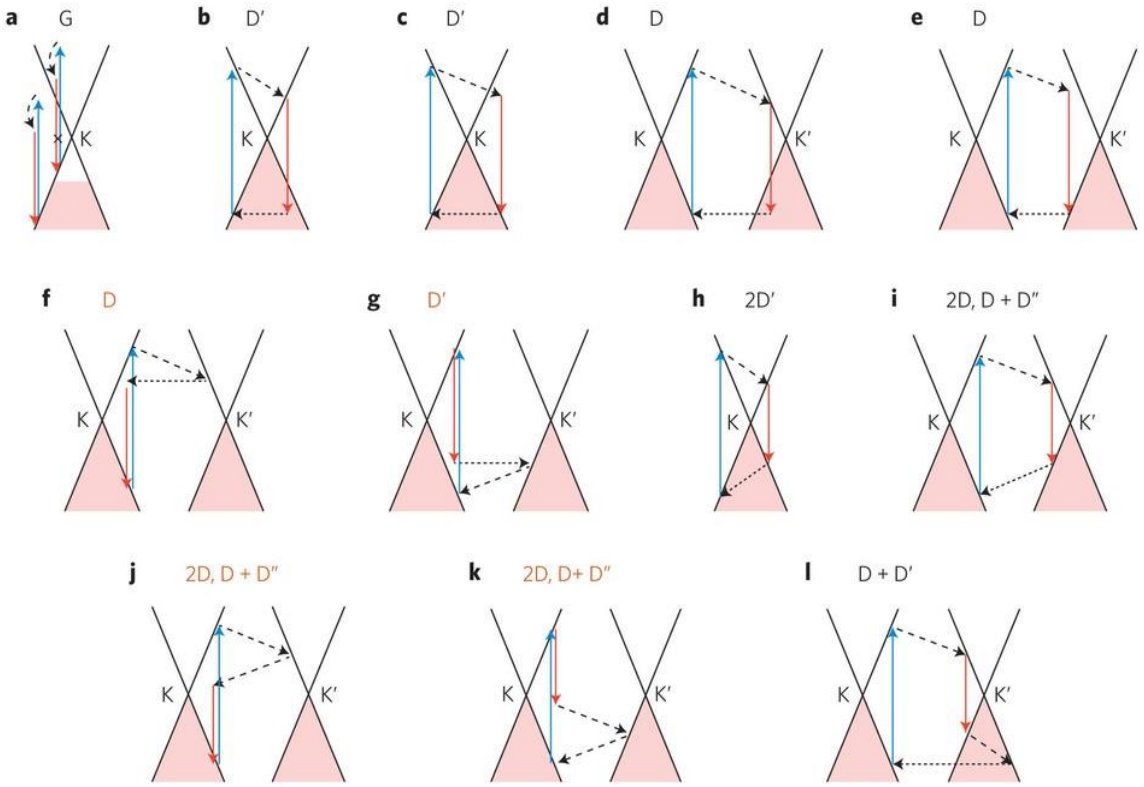

Figure 12 - Different scattering processes responsible for G bands (a), D and D' bands (b-c-d-e) and 2D bands [93].

In graphene, the G mode lies at around 1580 cm^{-1}, while the 2D peak is at around 2700 cm^{-1}. Another peak, called D peak, may appear at around 1350 cm^{-1} as a consequence of the presence of defects. The G mode corresponds to bond stretching of all pairs of sp^2 atoms in both rings and chains, whereas the D mode arises due to the breathing modes of sp^2 atoms in ring [93], [145]. Usually the D mode is not present in pristine and defect-free samples, however in presence of defects or edges the transition is allowed [145]. Thus, the D peak is absent in defect free graphene and graphite. While the G mode originates from a first order Raman scattering process, the D and 2D modes originate from a second-order double resonant process between nonequivalent K points in graphene's first Brillouin zone (Figure 12) [93]. Figure 13 shows a typical Raman spectrum for graphene and graphite respectively obtained using a 514 nm excitation laser.

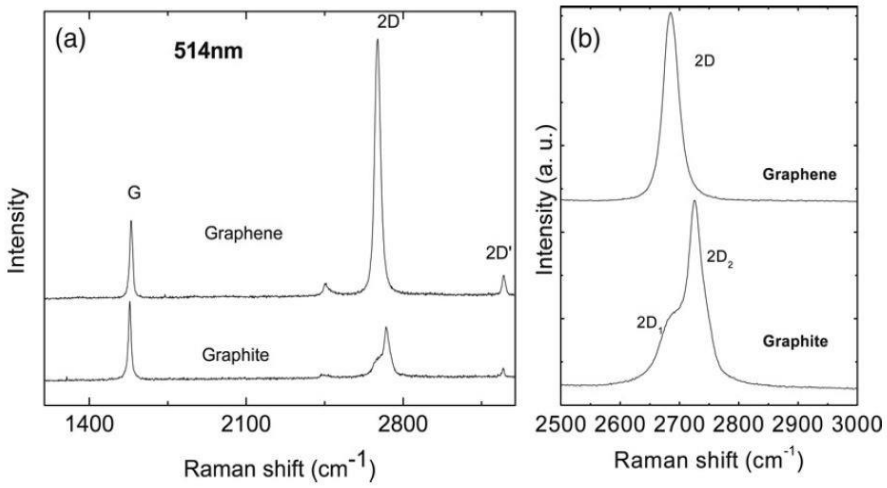

Figure 13 - a) Comparison of the Raman spectra of graphene and graphite measured at 514.5 nm. b) Comparison of the 2D peaks in graphene and graphite [145].

As shown in Figure 14, significant changes in position, lineshape and intensity are observed for the 2D band of graphene and graphite. The lineshape of the 2D peak, in monolayer graphene, is sharp, narrow and centered below 2700 cm^{-1}, for an excitation wavelength of 514.5 nm for example. An increase in the number of layers reduces the relative intensity of this peak - I(2D), with respect to the G one – I(G), and increases its full width at half maximum (FWHM) [93]. In fact, in graphene, the I(G) is lower than the I(2D) while, already for bilayers and thicker flakes, the G peak is the most intense peak [145].

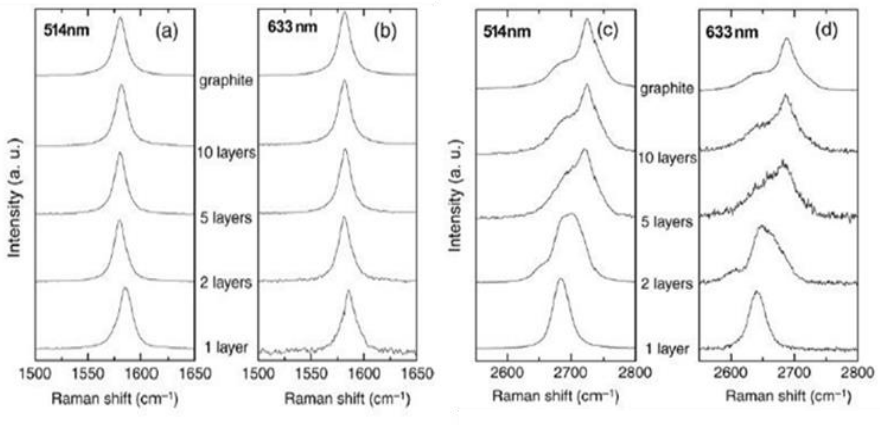

Figure 14 - a) and b) Evolution of G peak as a function of number of layers for 514 and 633 nm excitations, c) and d) Evolution of the 2D peak as a function of number of layers for 514 and 633 nm excitations [145].

The 2D pick is a superposition of multiple components, the main being the $2D_1$ and $2D_2$ components, for few-layers graphene [93], [94]. In general, for graphite the intensity of 2D2 peak ($I(2D_2)$) is roughly double compared to the intensity of $2D_1$ peak ($I(2D_1)$) [93], [94]. while for single-layer graphene the 2D band is a single and sharp peak, which is roughly four times more intense than the G peak [93], [94]. Taking into account the intensity ratios of the $2D_1$ and $2D_2$, it is possible to estimate the flake thickness [93], [94]. The normalized intensity ratios $I(2D_1)/I(G)$ vs. $I(2D_2)/I(G)$ gives a view of the flakes thickness. The $I(2D_2)/I(2D_1)$ ratio decreases as the flake thickness is reduced [93], [94], until the 2D band is constituted by the mere $2D_1$ Lorentzian component for single-layer graphene [93], [94]. The line $I(2D_1)/I(G) = I(2D_2)/I(G)$ roughly represents the multilayer condition (~ 5 layers) [93], [94]. Thus, graphitic samples whose $I(2D_2)/I(2D_1)$ value falls above the aforementioned line can be assumed to be less than 5 layers thick, while for the ones that the aforementioned value falls below, are considered thicker than 5 layers, thus displaying graphite-like properties [93], [94].

The C band can also be used to obtain detailed information about the number of layers. Unlike D, G, 2D, which are due to in-plane vibrations and therefore visible in SLG, the C peak originates from the shear motion of the graphene layers. Being sensitive to the interlayer coupling (whence the name C) its absence would be the proof of the presence of SLG [93]. However, care must be taken in doing so because the lack of a signal could always be linked with experimental procedures/errors. This low frequency mode ranges from 31 cm^{-1} in BLG to 42 cm^{-1} in graphite, scaling with the number of layers, as shown in Figure 15.

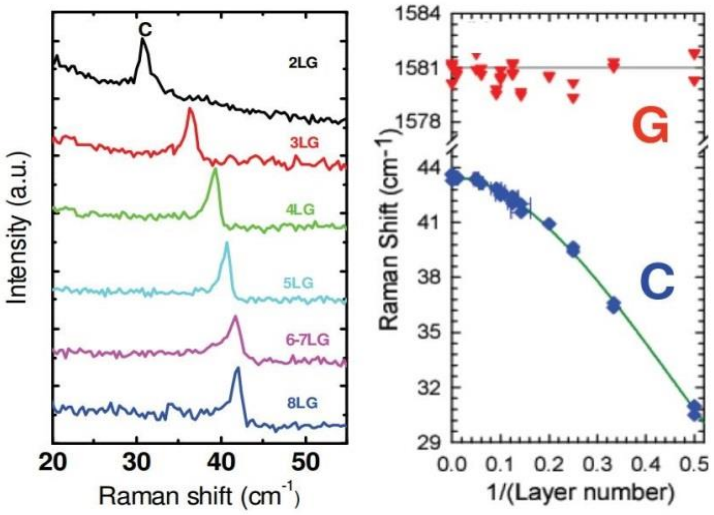

Figure 15 - Evolution of C band in few layer graphene [93].

Raman spectroscopy is also a powerful tool to investigate the presence of impurities and defects [92]. In fact, the interpretation of Raman spectra offers the possibility to understand the origin and quantity of structural disorder in the carbon sample as well as to distinguish between graphite and amorphous carbon that shows a mixture of sp^2 and sp^3 hybridization [92], [145].

Moreover, Raman spectroscopy allows to distinguish between edges defects and structural bulk defects in graphene [92]. There is an increase of the ratio I(D)/I(G) with defect density. Through the correlation between the ratio I(D)/I(G) and FWHM(G) it is possible to define the origin of defects. In principle, the I(D)/I(G) ratio cannot discriminate between defects localized in the bulk and the ones at the edges. However, when this intensity ratio is coupled with the FWHM(G), useful information about defects can be obtained. In fact, a larger FWHM(G), with respect pristine un-defected samples, is a direct consequence of an increasing of bulk disorder [145]. Therefore, if there is a correlation between I(D)/I(G) and FWHM(G) it is a clear signature of a structural disorder.

Experimentally, in this work Raman spectroscopy was used to measure the effectiveness of the graphite exfoliation process. The graphene-based inks were drop-cast onto a Si wafer with 300 nm thermally grown SiO_2 (LDB Technologies Ltd.) and dried under vacuum. A Renishaw inVia confocal Raman microscope using an excitation line of 514 nm for graphene-based inks collected Raman measurements. A 100× objective lens was used to focus on the samples with an incident power of laser ~1 mW. For each sample, more than 20 spectra were collected.

3.3 Transmission electron microscopy

In optical microscopy, the resolution is physically limited because of the Abbe diffraction limit [150]. The theoretical resolution limit of an optical microscope, assuming visible range light (from 380 to 740 nm), is ~250 nm. Transmission electron microscopy (TEM) is able to avoid this problem due to the smaller de Broglie wavelength of electrons [151]. Electrons, as well as all matter, can exhibit a wave-like behaviour [152]. The de Broglie wavelength is the wavelength (λ) associated with a massive particle and is related to its momentum, p, through the Planck constant, h [152]:

$$\lambda = \frac{h}{p} \qquad \text{Eq. 10}$$

In this way, TEM allows the study of (nano)materials up to the atomic scale by breaking the diffraction limit of the optical microscopy. In a TEM experiment, the electrons are emitted from an electron gun by thermionic or field emission under ultra-high vacuum (UHV) conditions [153]. The gun consists on a tungsten filament or a lanthanum hexaboride source. When the gun is connected to a high voltage source (from 60 to 200 kV) it emits electrons. The electron beam is created at this point and it is the analogue of a lamp emitting light rays in an optical microscope [153]. Because of the small electron's mass, high vacuum conditions (typically up to 10−7Pa) are necessary in order to avoid interaction or deflection due to gas particles [153]. Subsequently, the electrons are injected into the microscope column by virtue of accelerating voltages, ~ 100 keV, and directed through a double or triple electromagnetic condenser lens system to illuminate the specimen under investigation [153]. The passage of electrons through the sample determines a scattering by the electrostatic potentials of the atoms [153]. An image is formed from the interaction of the electrons transmitted through the specimen; the image is magnified and focused onto an imaging device, such as a fluorescent screen, on a layer of photographic film, or to be detected by a sensor such as a charge-coupled device [153]. The sample is placed on a standard perforated grid for TEM analysis. TEMs are capable of imaging at nanometer- and atomic- scale resolution [153]. To perform imaging at high resolution, thin samples and high energies of the incident electron beam are needed [153].

In this work, TEM imaging was carried out on a JEOL JEM 1400Plus microscope, operating at 120 kV, equipped with a LaB6 thermionic source, a Gatan charge-coupled device (CCD) camera Orius 830. Lateral size statistic is fitted with log-normal distribution [117].

3.4 Scanning electron microscopy

Scanning electron microscopy (SEM) is a fundamental imaging technique for surface morphology and obtaining information on chemical composition of thicker samples [154]. It is used extensively for defect analysis of semiconductor wafers, and manufacturers make instruments that can examine any part of a 300 mm semiconductor wafer [154]. Many instruments have chambers that can tilt an object of that size to 45° and provide continuous 360° rotation [154]. A lens condenses the electron beam (~ 1 nm) extracted by an anode (usually, acceleration voltages of between 5 and 20 kV are used [155]). The beam, interacting with the surface, is then raster scanned by varying current through the scanning coils [156]. Electrons as well as characteristic x-rays are emitted by the sample following the interaction with the electron beam [156]. For conventional imaging electrically conductive samples are needed, or they must be prepared to increase their electrical conductivity and to stabilize them, in order to withstand the high vacuum conditions and the high energy beam of electrons [154]. Non-conductive specimens collect charge when scanned by the electron beam and this causes scanning faults and other image artefacts, so they are usually coated with an ultrathin coating of electrically conducting material, deposited on the sample either by low-vacuum sputter coating or by high-vacuum evaporation [156]. Samples are usually mounted on a specimen holder or stub using a conductive tape to be electrically grounded in order to prevent the accumulation of electrostatic charge [154]. Unlike in an optical system, the resolution is not limited by the diffraction limit, fineness of lenses or mirrors or detector array resolution [154]. Resolution is limited to a few nm by a combination of the size of the electron spot and the interaction volume [154]. The two primary types of electrons involved in SEM imaging are back (elastically) scattered electrons and secondary (inelastic) electrons. Low energy (< 5 eV), inelastically scattered electrons give information within a few nm of the sample surface. Thus, they are good for surface imaging. Back scattered electrons are higher in energy and produced from deeper within the interaction volume [156]. Since heavier elements backscatter electrons more strongly this can be used to detect contrast between areas of different chemical composition [154]. Similarly, characteristic x-rays are emitted when the electron beam removes core shell electrons from the sample which are filled by an electron from a higher shell. The analysis of the emitted radiation by energy dispersive X-ray spectroscopy (EDX) also allows to obtain a chemical analysis of the sample [156].

3.5 Atomic force microscopy

Atomic-force microscopy (AFM) is a high-resolution type of scanning probe microscopy (SPM), with demonstrated sub-nanometer resolution, more than 1000 times better than the optical diffraction limit [157]. Figure 16 shows an AFM typically consisting of the following [157]: the small spring-like cantilever is supported by a holder; a piezoelectric element oscillates the cantilever. A sharp (curvature of 1-2 nm) tip, usually made of silicon, is fixed to the free-end of the cantilever. The detector records the deflection and motion of the cantilever. The sample is mounted on the sample stage. A three-dimensional drive permits to displace the sample and the sample stage in x, y, and z directions with respect to the tip apex. Although, Figure 16 shows the drive attached to the sample, the drive can also be attached to the tip, or independent drives can be attached to both, since it is the relative displacement of the sample and tip that needs to be controlled. The information is gathered by "feeling" or "touching" the surface with a mechanical probe. Piezoelectric elements enable very precise scanning thanks to accurate and precise movements on (electronic) command. According to the configuration described above, the tip-sample interaction is transduced into changes of the motion of cantilever, which is a macro scale phenomenon. Several different aspects of the cantilever motion can be used to quantify the interaction between the tip and sample, most commonly the value of the deflection, the amplitude of an imposed oscillation of the cantilever, or the shift in resonance frequency of the cantilever. The detector of AFM measures the deflection (displacement with respect to the equilibrium position) of the cantilever and converts it into an electrical signal. The intensity of this signal will be proportional to the displacement of the cantilever. AFM is uniquely positioned to provide structural, mechanical, and, when using conductive probes, electrical characterization of graphene and related two-dimensional materials. Some of the utility of AFM simply derives from its impressive height sensitivity. Going beyond simple topography measurements, there are a myriad of mechanical and electrical characterization techniques that are based on the AFM's cantilever [158]. In this work, AFM images were acquired using a Nanowizard III (JPK Instruments, Germany) mounted on an Axio Observer D1 (Carl Zeiss, Germany) inverted optical microscope. The scan rate for the acquisition of images was 0.6 Hz. The samples were prepared by drop-casting the exfoliated InSe flake dispersions onto mica sheets (G250-1, Agar Scientific Ltd., Essex, UK) and subsequently drying them under vacuum overnight. Thickness statistic is fitted with log-normal distribution [117].

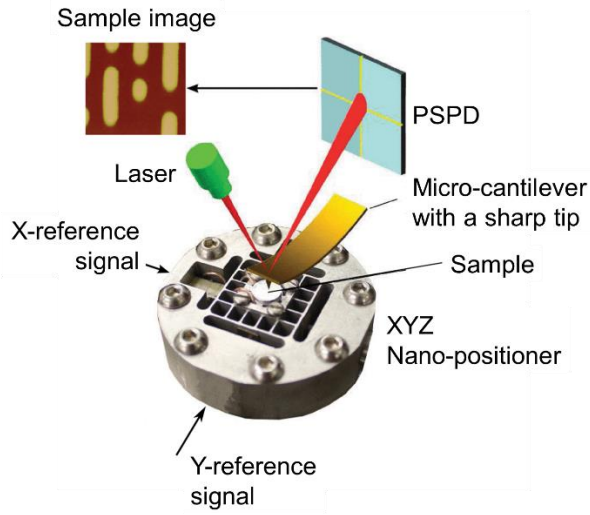

Figure 16 - Layout of the main components in an AFM system [159].

3.6 Rheological measurements

Generally speaking, a printable ink should possess proper fluidic properties, specifically the most suitable η and γ, depending on the considered application [160]. Moreover, the deposition can be performed exploiting a variety of techniques. For these reasons, rheological studies of the inks must be carried out in order to tune the fluidic properties on demand. In the case of 2d material-based inks, the rheological properties can be controlled through both the selection of the solvents and the parameters of the exfoliation process (e.g., sonication time, speed and time of centrifugation), and they can be measured using a rheometer [96]. Different typologies of measurements can be carried out. In peak−hold measurements, η is measured through a temporal range at fixed temperature and shear rate. In flow−ramp measurements, η is instead measured as a function of shear rate at fixed temperature. In temperature−ramp measurements, η is measured as a function of temperature at a fixed shear rate.

4 RADIO FREQUENCY ELECTROMAGNETIC DEVICES

From a classical and macroscopic point of view, an electromagnetic wave is generated by free charge ρ and current density **j** distributions. Such interactions can be described by Maxwell's macroscopic equations [161]:

$$\nabla \cdot \boldsymbol{D}(\boldsymbol{r},t) = 4\pi\rho(\boldsymbol{r},t) \quad \text{Eq. 11}$$

$$\nabla \cdot \boldsymbol{B}(\boldsymbol{r},t) = 0 \quad \text{Eq. 12}$$

$$\nabla \times \boldsymbol{E}(\boldsymbol{r},t) = -\frac{1}{c}\frac{\partial}{\partial t}\boldsymbol{B}(\boldsymbol{r},t) \quad \text{Eq. 13}$$

$$\nabla \times \boldsymbol{H}(\boldsymbol{r},t) = \frac{1}{c}\frac{\partial}{\partial t}\boldsymbol{D}(\boldsymbol{r},t) + \frac{4\pi}{c}\boldsymbol{j}(\boldsymbol{r},t) \quad \text{Eq. 14}$$

written in Gaussian units, where **E** is the electric field, **D** is the electric displacement field, **H** is the magnetic field, **B** is the magnetic induction, and *c* is the speed of light in vacuum. By combining Equations 11-14, continuity equation can be found [161]:

$$\frac{\partial}{\partial t}\rho(\boldsymbol{r},t) + \nabla \cdot \boldsymbol{j}(\boldsymbol{r},t) = 0 \quad \text{Eq. 15}$$

The dependence of polarization and magnetization inside a material on the electromagnetic field can be expressed by the effects of the bound charge and current densities in matter, leading the so-called constitutive relations expressed by **D** and **B** in terms of **E** and **H** [161]. In particular, in a homogenous, isotropic, non-magnetic, and linear material, the constitutive relations can be expressed as

$$\boldsymbol{D}(\boldsymbol{r},t) = \iint \varepsilon(\boldsymbol{r} - \boldsymbol{r}_0, t - t_0)\, \boldsymbol{E}(\boldsymbol{r}_0,t_0)\, d\boldsymbol{r}_0 dt_0 \quad \text{Eq. 16}$$

$$\boldsymbol{B}(\boldsymbol{r},t) = \boldsymbol{H}(\boldsymbol{r},t) \quad \text{Eq. 17}$$

where $\varepsilon(\mathbf{r} - \mathbf{r}_0, t - t_0)$ is the dielectric function of the material [161].

4.1 Antennas

Wireless systems play an increasingly important role in society [162]. Whether used to assist in the distribution and collection of large amounts of information or to make home entertainment systems more affordable, wireless systems are becoming increasingly integrated into everyday activities [162]. There is a wide range of antennas needed to interface with the commercial market. The growing diffusion of wireless technologies such as Wi-Fi [162], Bluetooth [162], radio-frequency identification (RFID) [163] and near field communication (NFC) [164] in handheld and portable devices, e.g., mobile phones, PDAs, electronic wristbands [164], is pushing the research on scalable production of low-cost and highly efficient antennas [162], [164]. A particularly appealing application is their use for intelligent and smart packaging [165], package tracking [165] and tracing [165]. Carbon-based conductive RFIDs are emerging as a viable alternative to the current metal-based technology [164]. However, there are some key features to be addressed, and a compromise between the various properties is necessary to ensure that the solution chosen works in the best possible way [162].

4.1.1 Size

The size of the antenna and its overall impact on the surrounding environment are extremely important for most wireless communication systems. Antennas must be unobtrusive and extremely small, without compromise their performance (typically return loss bandwidth and gain) [162], [166]. Limits to the size of the antenna must be taken into account, so an efficient solution is required [162]. However, reducing the dimensions of the antennas can be very complicated (if not impossible) if the antennas are planar [162]. Furthermore, for some applications (such as RF front-ends), the antennas cannot be too small, because of the realization restrictions due to the supply network [162], [166].

4.1.2 Integration

The ease of integration is a very important property in antenna technology. Generally, efficiency is proportional to integration, which is very important for wireless applications in the high-frequency microwave bands [162], [166].

4.1.3 Efficiency

Efficiency is a very important feature for any antenna. The dimensions and the material used to implement the antenna are key factors that affect efficiency [162]. For printed antennas, low-loss dielectric support substrate is required, particularly for high-frequency applications. Small antennas can be developed thanks to dielectric substrates with high dielectric constant (high-ε) [162]. Low loss high-ε materials are needed since in general the loss-tangents (δ) of high-ε materials are higher than their low dielectric constant counterparts and therefore the overall impact on radiation performance can be severe [162], [166].

4.1.4 Bandwidth

The designed antenna must meet the bandwidth requirements for the wireless system [162], [166]. Although there is no universal definition that can be applied to all wireless systems, generally the return loss bandwidth is defined as the frequency range in which the return loss is larger than 10 dB, which means that less than 10% of the power is reflected in the RF circuits [162].

4.1.5 Polarization

The polarization of an antenna is an interesting issue [162]. Polarization is defined as the path traced by the electric field vector as a function of time. There are three forms of polarization: linear, circular and elliptic [162]. Linear polarization occurs when the phase difference of the components of the electric field between them is 0° or 180°. Circular polarization occurs when there are two components of the electric field, they are equal in magnitude and one of the components differs the other by 90°. Circular polarization can be right-handed or left-handed, depending on the direction in which the field rotates over time. Elliptical polarization occurs when the components of the electric field do not have the same amplitude and arbitrary phase difference between them [162].

4.2 Electromagnetic measurements

To describe the electrical behaviour in radiofrequency (RF) networks (such as antennas, lumped elements and transistors), scattering parameters (S_{mn}) are required [167]. In the S-parameter approach, an electrical network is considered a "black box" containing several components of interconnected electrical circuits interacting each other through ports [167]. For example, in Figure 17 is shown a 2-port network, where V_n^+ is the amplitude of the voltage wave incident on port n, V_n^- is the amplitude of the voltage wave reflected from port n and Z_A, Z_B and Z_C are the impedances of the network.

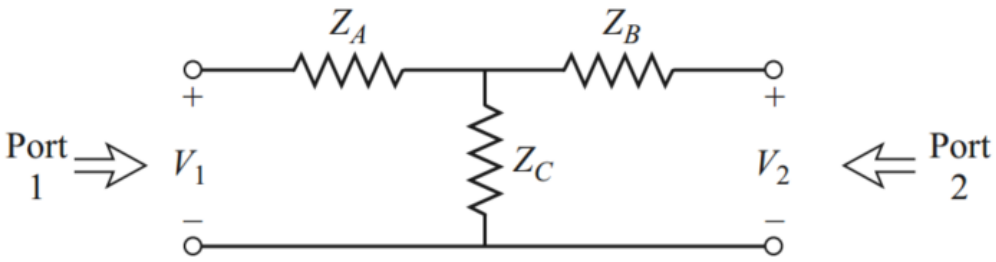

Figure 17 - A 2-port microwave network.

This network is completely characterized by a square matrix of complex numbers called the S-parameter matrix, which can be used to calculate its response to the signals applied to the ports [167]. The S-parameter matrix, is defined in relation to the incident and reflected voltage waves as [168]:

$$\begin{bmatrix} V_1^- \\ V_2^- \end{bmatrix} = \begin{bmatrix} S_{11} & S_{12} \\ S_{21} & S_{22} \end{bmatrix} \begin{bmatrix} V_1^+ \\ V_2^+ \end{bmatrix} \qquad \text{Eq. 18}$$

Many electrical properties of component networks can be expressed using the S-parameters, such as gain, return loss (S_{11}), transmission coefficients (S_{12} and S_{21}) and amplifier stability [167]. In the next sections, basic concepts and techniques of antenna pattern measurement will be explained as well as their benefits and drawbacks. The concepts relating to near-field and far-field pattern testing will be discussed as well.

4.2.1 Impedance Measurements

The impedance is fundamental to an antenna that operates at RF [167]. If the impedance of an antenna is not "close" to that of the transmission line, then very little power will be transmitted by the antenna (if the antenna is used in the transmit mode), or very little power will be received by the antenna (if used in the receive mode) [167]. Hence, without proper impedance matching network, the antenna will not work properly. A Vector Network Analyzer (VNA) is a measuring tool that can be used to measure the input impedance as a function of frequency. Alternatively, it can plot the S-parameters, in particular the S_{11} (return loss), that are frequency-dependent functions of the antenna impedance [167].

4.2.2 Radiation pattern and gain

The polarization and antenna gain (for the fields radiated toward the test antenna) of the source antenna are the measurements needed to determine the directional (angular) dependence of the strength of the radio waves from the antenna and how well the antenna converts input power into radio waves headed in a specified direction respectively [167]. Due to reciprocity, the radiation pattern from the test antenna is the same for both the receive and transmit modes. Consequently, we can measure the radiation pattern in the receive or transmit mode for the test antenna. It is possible to measure the gain from the S_{21} parameter [167].

4.2.3 Phase measurement

Phase is an important feature to completely specify the antenna radiation pattern beyond the magnitude of the power received or transmitted [167]. Phase measurements are made using S-parameters, just like gain measurements. The phase is a relative quantity that must be measured relative to some fixed reference [167]. The response signal can be either reflected or transmitted. Assuming an accurate calibration has been performed, the difference in phase between the two signals (known as phase shift) is a result of the electrical characteristics of the antenna under test (AUT) [167].

4.2.4 Polarization Measurements

Fundamental to an antenna radiation pattern is its polarization [167]. The polarization varies depending on the direction of radiation from an antenna. To perform the measurement, the test antenna must be use as the source and a linearly polarized antenna as the receiving antenna [167]. By rotating the receive antenna, it is possible to record the power as a function of the angle and have the information on the polarization of the test antenna [167].

5 POWER SUPPLY DEVICES

In view of the implementation of an embedded device that can receive a signal from the sensor (e.g., photodetector) and send it from an antenna, it is necessary to feed the system and/or store the energy through power suppliers such as batteries, solar cells or supercapacitors. In this context, thin and printable devices must be designed to be integrated with the sensor and the antenna. The use of supercapacitors and solar cells can be a valid solution to feed this kind of systems.

5.1 Supercapacitor

In order to supply power to the antenna-sensor system, lithium-ion (Li-ion) batteries can be a solution, but their overall size combined with their limited capacity is a problem for this kind of application [169]. Two possible FoMs that can be used to compare batteries and supercapacitors (SCs) are the Energy Density (E_d) and the Power Density (P_d). E_d represents the amount of energy that can be stored within each kg of device [169]. In the case of electrochemical double-layer capacitors it is given by

$$E_d = \frac{1}{2} Q \cdot \mathrm{V}^2 \qquad \text{Eq. 19}$$

where Q is the specific capacitance, expressed in Ah kg^{-1} and V is the voltage applied to the SC. E_d is expressed in Wh kg^{-1}. P_d corresponds to the power that each kg of the device can produce during the discharge. It depends on the current that the battery must supply. Usually P_d is expressed in W kg^{-1}. To characterize the compromise between effective capacity and power handling it is possible to relate E_d and P_d (Figure 18). For example, considering a device that is charged with E_d = 100 Wh kg^{-1} in 1 hour, if a connected load requires P_d = 100 W kg^{-1}, the device is discharged in 1 hour while if the load requires 1 kW kg^{-1}, the device lasts only 6 minutes. Commercially available batteries are in the middle of this graph (Figure 18 in blue for Li-ion batteries and red for Ni-Cd and Pb-Acid batteries), the typical time for their charge and discharge is around a few hours. A SC is defined as an electrochemical capacitor with values of specific capacitance 2 to 5 orders of magnitude larger than conventional capacitors [169]. This increase in capacitance is made possible by the formation of electrostatic double layers directly at the interface between the electrolyte and electrodes with a high specific surface area. Compared to electrolytic capacitors, SCs have lower voltage limits due to the occurrence of electrochemical side reactions at high voltages, although with the use of anhydrous

ionic liquid electrolytes the operating voltage can exceed 3.5 V [169]. Usually a SC stores 10 to 100 times more energy per unit of volume or mass than the electrolytic capacitors [169], it can accept and supply much faster than the batteries [169] and it tolerates many more charge and discharge cycles than rechargeable batteries [169] so as to bridge the gap between electrolytic capacitors and rechargeable batteries. On the other hand, the SCs (Figure 18, green) could fill the gap between batteries and capacitors which are chargeable and dischargeable in few ms [169]. The most interesting feature of SCs is that they have high specific powers, but low specific energy compared to batteries. Consequently, they are good for applications that require concentrated power in short time. In the antenna data transmission scenario, SCs may be the best choice to feed the antenna-sensor system.

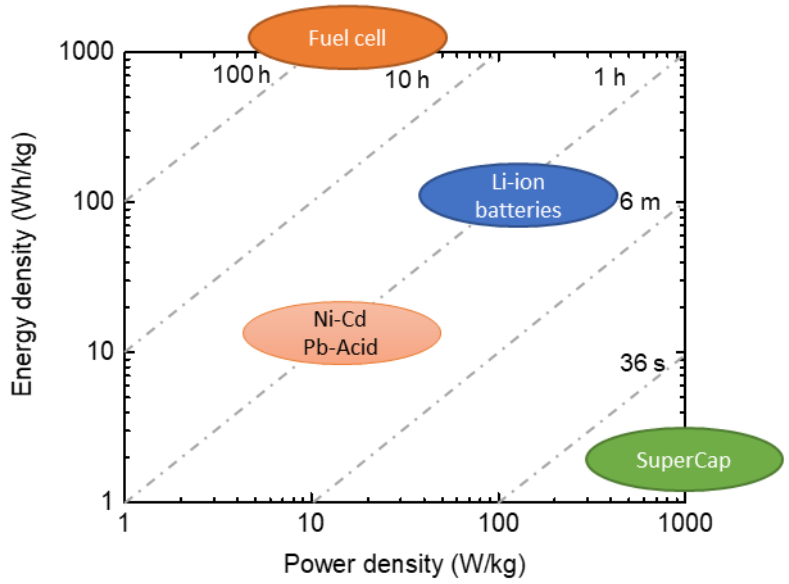

Figure 18 - E_d vs P_d plot of common energy storage devices. Data taken from Ref. [169]

5.2 Electrochemical measurements

In order to evaluate the SC performances, the cyclic voltammetry (CV) and the electrochemical Impedance Spectroscopy (EIS) can be used [170]. CV is a three-electrode measurement in which the potential of a test electrode, with respect to reference electrode, is swept cyclically at a constant rate between two potential limits while allowing current to flow between the test electrode and a counter-electrode [170]. The potential provides the driving force for reactions at the test electrode, while the current is proportional to the rate of these reactions. CV identifies the presence of electrochemical reactions and provides information on the reversibility of the reactions, the quantity of electroactive

material on the electrode, and the stability of the electrode [170]. It is important to appreciate that the CV response, for any electrode material, can appear very different depending on the sweep rate, the geometric area of the electrode, and the roughness of the electrode, even though the electrochemical reactions are unchanged [170]. EIS involves measuring the electrical impedance and phase angle obtained with sinusoidal voltage or current excitation of the electrode [170]. The measurement is made over a broad frequency range (typically < 1 Hz to 10^5 Hz), and the magnitude of the excitation is sufficiently small that a linear current-voltage response is obtained at each frequency [170]. For voltage excitation, the root-mean-square magnitude of the excitation source is typically ~10 mV, and generally not more than 50 mV [170].

6 (OPTO)ELECTRONIC DEVICES

Many methodologies for the characterization of conductive patterns, semiconductor and RF devices have been developed over the years. This chapter presents some procedures to measure useful parameters such as resistivity (ρ), sheet resistance (R_s), scattering parameters (S_{mn}) radiation pattern and gain, to characterize the devices shown in this thesis. Basic theory would be presented to help to better understand the characterization process.

6.1 Photodetectors

A photodetector is a device that can convert a light signal into an electrical signal [171]. There are two types of photocurrent generation mechanisms. One is related to the excitation of free carriers following the optical transition, including the photovoltaic effect, the photoconductor effect and the photogating effect [172]. The other is attributed to the thermal effect, including the photothermoelectric effect (PTE) and bolometric effect [172]. High performance photodetectors play important roles in many fields of our life, including electro-optical displays, imaging, environment monitoring, optical communication, military and security checking [172]. Traditional photodetectors such as silicon (Si) photodetectors [173] and InGaAs photodetectors [174], [175] continue to dominate the commercial photodetector market due to their high performance, proficient integration technology and large-scale production [172]. They work at room temperature (RT) in the visible and near-infrared (IR) range [176]. However, high performance mid-wave infrared and long-wave infrared photodetectors based on HgCdTe [177] GaSb/InAs [178]–[180] and InSb [181] must operate at liquid nitrogen temperature (77 K). Despite traditional 3D photodetectors are still widely applied in our daily life, novel 2D layered material-based photodetectors have emerged. Thanks to the unique electronic and optoelectronic properties of some 2D materials many achievements of 2D based photodetectors have been reported, including physical flexibility [182], ultrahigh photoresponsivity [183], ultrafast photoresponse [184], ultrabroad detecting band (from UV to terahertz (THz) frequencies) [185], and ultrasensitive photodetection [186]. A particular type of photodetector is the phototransitor. A phototransistor is nothing more than a Field Effect Transistor (FET) designed so that light can reach the light-sensitive semiconductor. To better compare the performance of photodetectors with different sizes and operating conditions, a set of figures of merit are defined. In the following section these important parameters will be briefly introduced.

6.1.1 Photoresponsivity (R)

Photoresponsivity is defined as the ratio between the photocurrent or photogenerated voltage to the incident light power, expressed as:

$$R_i = \frac{I_P}{P} \text{ or } R_v = \frac{V_P}{P} \qquad \text{Eq. 20}$$

where P is the incident light power defined as $P = I_r S$. I_r is the irradiance [W m^{-2}] and S is the active area of the device [172]. Photoresponsivity depends on the wavelength due to the semiconductor energy gap and wavelength-dependence of light absorption. For commercially available photodetectors, the response is typically from 405 to 1100 A W^{-1} (@ 200-1000 nm) for Si [172], [173], from 870 to 1700 A W^{-1} (@ 200-2000 nm) for InGaAs [172], [175], and from 1100 to 3000 A W^{-1} (@ 1000-20000 nm) for HgCdTe [172], [177].

6.1.2 External Quantum Efficiency (EQE)

External quantum efficiency (EQE) is the ratio between the number of the collected charge carriers (N_C) and the number of photons N_I which illuminates the device that produces the photocurrent [172]. EQE can be expressed as:

$$EQE = \frac{N_C}{N_I} = \frac{hc}{e\lambda} R_i \qquad \text{Eq. 21}$$

where h is the Planck constant, c is the speed of light, e is the electron charge, and λ is the wavelength of the incident light [172]. When the light illuminates the sample, only a part of the photons is absorbed [172]. The number of absorbed photons can be expressed as $N_A = N_I \eta_A$, where η_A is the light absorption efficiency [172]. The internal quantum efficiency (IQE) is measured in a similar way except that only the absorbed light power is used for calculation. Hence IQE is defined as $IQE = \frac{N_C}{N_A} = \frac{EQE}{\eta_A}$ [172].

6.1.3 Response Time and Cut-off Frequency

The response time is one of the important operating parameters of a photodetector [172]. It includes the rise time τ_r (and fall time τ_f) which are usually defined as the time measured from 10% (90%) to 90% (10%) of the net photocurrent after switching on (off) the light excitation [172]. Photoresponsivity depends on the light modulation frequency. As the modulation frequency increases, the photoresponsivity decreases [172]. The frequency at which the photoresponsivity is reduced to 0.707 R_0 (3 dB - R_0 is photoresponsivity measured under static illumination) is called the cut-off frequency f_C [172].

6.1.4 Photoconductive Gain (G)

Photoconductive gain is a feature to evaluate the number of generated multiple carriers from a single incident photon [172]. A photogenerated electron or hole can circulate several times in the channel and this phenomenon is related to a long life-time (τ_{life}) and a short drift transit time (τ_{tran}) and determines the photoconductive gain [172]. The photoconductive gain produced by the long carrier life time is given as $G = \frac{\tau\ life}{\tau\ tran}$. The transit time depends on the applied bias voltage (V_{bias}), carrier mobility (μ) and the length of the channel (L) and is given by $\tau_{tran} = \frac{L^2}{\mu V_{bias}}$ [172].

6.1.5 Noise Equivalent Power (NEP)

Noise equivalent power (NEP) is the minimum light signal power that determines in a photodetector a ratio of signal to noise (S/N) of unity at 1 Hz bandwidth [172]. The NEP is regarded as the minimum light intensity that can be detected or distinguished from the total noise (e.g., ambient induced noise, internally generated noise) by a photodetector [172]. It can be expressed as:

$$NEP = \frac{i_N}{R} \qquad \text{Eq. 22}$$

where i_N is the noise current spectra at 1 Hz bandwidth with units of $A \cdot Hz^{-0.5}$, R is the responsivity of a device. Hence NEP has a unit of $W \cdot Hz^{-0.5}$. For a commercial Si detector, NEP is on the order of 10^{-14} $W \cdot Hz^{-0.5}$ [172].

6.1.6 Specific Detectivity (D)*

The sensitivity of a photodetector is represented by the specific detectivity [172]. It is one of the most important figures of merit, which, for a better comparison among detectors, excludes the influence of bandwidth, geometry, and area of device [172]. Specific detectivity is defined as:

$$D^* = \frac{\sqrt{S}}{NEP} \qquad \text{Eq. 23}$$

where S is the active area of device and NEP is defined above. D* is measured in cm $Hz^{0.5} \cdot W^{-1}$ (Jones). In a commercial Si photodetector, D* is on the order of 10^{12} Jones [172]. For other commercial detectors, the D* of InGaAs is on the order of 10^{12} – 10^{14} Jones, [86, 87] 10^{11} for HgCdTe, 10^{10} for HgCdTe, [9] and 10^{14} for GaN/AlGaN [86].

6.2 DC electrical measurements

In order to measure the electrical resistivity, Two Probe (TP) and Four Probe (FP) methods can be used. Many factors affect the suitability of these methods, i.e. two important parameters to take into account are the contact resistance and shape/dimension of the sample. TP configuration is one of the standards and most commonly used method for the measurement of resistivity of very high resistivity samples (near insulators) and it is the simplest configuration to measure resistivity. Voltage drop (V) across the sample and current (I) through the sample are measured. In this way, resistivity is defined as $\rho = \frac{VA}{IL}$, where V is the voltage probes, A is the cross-sectional area of the sample under measurement, I is the current flowing through it and L is the length of the sample. On the other hand, FP configuration is the most widely used method for resistivity measurements. FP sensing is used to measure sheet resistance of thin films (particularly semiconductor thin films) [187]. This technique uses separate pairs of current-carrying and voltage-sensing. Separation of current and voltage

electrodes eliminates the lead and contact resistance from the measurement [187]. This is an advantage for precise measurements, especially in materials having low resistance [187]. Current (I) that passes through the outer probes induces a voltage drop (V) between the two inner probes (Figure 19). When the probe spacings are equal and small compared to the lateral dimensions of the sample being measured, the voltage difference between the inner probes may be defined as [188]:

$$V = \frac{IRs}{\pi}\ln(2) \qquad \text{Eq. 24}$$

giving:

$$R_s = \frac{V}{I}\frac{\pi}{\ln(2)} \approx \text{V/I} \times 4.53 \qquad \text{Eq. 25}$$

R_s measurements need to be carried out avoiding the sample edges in order to verify the approximation of the four-probe method.

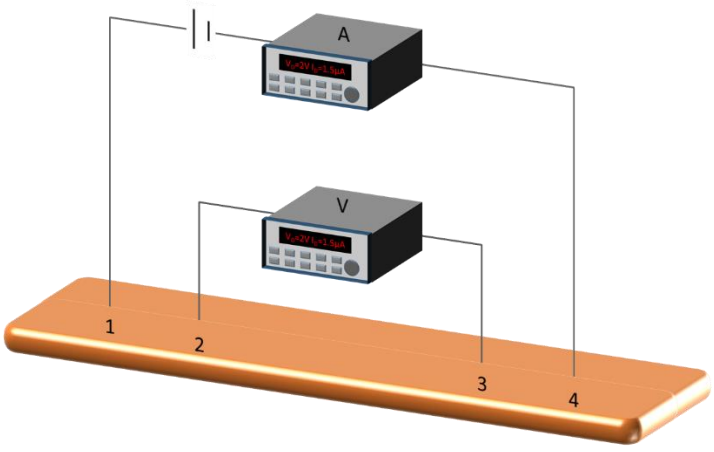

Figure 19 - Four-point measurement of resistance between voltage sense connections 2 and 3. Current is supplied by connections 1 and 4.

6.3 Photodetector characterization

A photodetector can be characterized in dark condition by performing a DC electrical measurement. In the case of FET photodetector, a standard FET characterization is used. In order to determine the performance of the FET, DC Parameters are important features to consider. Breakdown voltage and leakage current are two common parameters that are normally characterized [189]. Breakdown Voltage indicates the voltage at which "avalanche breakdown" and "thermal runaway" take place. The leakage currents indicate currents within the safe operating region of reverse voltage [189]. To define, determine and understand the basic parameters of a transistor operation within an electrical circuit, a set of curves called I-V Characteristic Curves are used. The current through the channel is defined as [189]:

$$I = \mu W C_i (V_{GS} - V_T)\, {}^{V_{DS}}/_{L} \qquad \text{Eq. 26}$$

assuming $V_{DS} << V_T$ in which V_{DS} is the drain-source voltage, V_T is the threshold voltage and V_{GS} is the gate-source voltage [189]. W is the device width, μ is the charge carrier mobility and C_i is the gate oxide capacitance per unit area. The ability of FET to amplify the signal is given by the output/input ratio (transconductance), $g_m = dI/dV_{GS}$ [189].

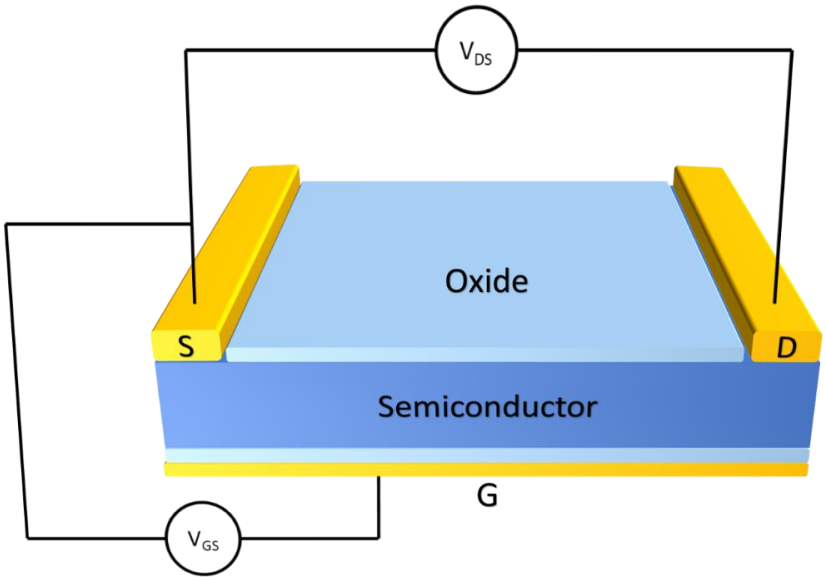

Figure 20 - FET measurement setup.

For FET photodetectors, in case of light condition, it is possible to perform the same characterization seen with the dark condition but with both persistent light signal or ON-OFF transitions at different wavelengths [172]. It is possible to examine the amount of current flowing through the photodetector, depending on the value of light intensity [172].

7 DEVICE FABRICATION TECHNIQUES

7.1 Deposition techniques

The following section introduces the coating / printing techniques. Nowadays, a major research effort is needed to find suitable nanomaterials and optimize printing processes for low-cost applications. For electrical applications, for example, it is necessary to optimize the electrical, optical and mechanical properties of the printed material in view of low-cost and large-scale production, besides the biocompatible properties in the case of wearable applications.

7.1.1 Spray coating

Spray coating is a typical industrial coating technique used for fast deposition of inks on both rigid and flexible large area (> several cm) substrates [136], [190]. The spray coating technique consists in spraying the ink by applying pressure through a transporting gas (i.e., nitrogen). Thus, an aerosol is formed when the pressurized ink passes through a nozzle [190]. Despite the process is simple, the subsequent drying process needs many processes and many parameters, such as the η and polarity of the solvent, the flow rate, the distance substrate/spray-nozzle, must be fine-controlled in order to obtain a uniform film [190]. The nature of the solvent is another critical parameter in the spraying process because its evaporation rate determines the homogeneity of the deposition on the substrate surface. In solvents with high vapor pressure solvents (i.e., isopropyl alcohol – IPA, and toluene – > 20 mmHg @25°C), a faster solvent evaporation is promoted, and a more uniform deposition is obtained, increasing the final devices performance. On the other hand, in the case of solvents with low vapor pressure such NMP (0.5 mmHg @25°C), a higher substrate temperature is needed, and spray coating does not allow a reproducible deposition of material due to the coalescence of the aerosol droplets on the substrate before they evaporate [190]. A non-uniform coating is also given by small nozzle size and low pressure due to the low flow regime, formed by scattered droplets on the substrate. On the contrary, high deposition rates determine the formation of a continuous film coating [190]. The substrate-nozzle distance is another important parameter for obtaining a uniform coating during the deposition process [190]. If this distance is small, the ink already deposited onto the substrate could be removed by the incoming flow. On the contrary, if the substrate/nozzle distance is too high, the solvent evaporates before reaching the substrate.

7.1.2 Inkjet printing

Inkjet printing is an ideal technique to print low-cost electronic components on both rigid and flexible substrates [191] as demonstrated for several applications including thin field-effect transistor (TFT) [192], light emitting diodes (LEDs), (opto)electronic devices such as sensors, [193], photovoltaics, [194] and capacitors. Up to date, several attempts have been made in order to develop inkjet-printed devices. For example, Coleman's group shows a TFTs with organic semi conductive inks, but the electron mobility is still very low compared to the one achieved with silicon ($\mu < 0.5$ $cm^2\,V^{-1}\,s^{-1}$). Carbon nanotubes (CNTs) or metal nanoparticles have been used to overcome this problem, but there are various limitations which are mainly represented by an instability of the inks or from undesired chemical reactions, such as oxidation [96]. Graphene and other 2D materials seem to be ideal candidates for further developments in this field [134], [191]. In the inkjet printing process, small ink droplets (e.g., 50-80 μm diameter), ejected from a print-head nozzle, are applied onto the target substrate with high spatial precision [140]. It is possible to adjust the voltage waveform acting on the transducers that cause the ejection of the ink from each individual nozzle, according to the rheological properties of the liquid or the size of the particles in suspension. During an inkjet process, regular jetting and the impact velocity of the droplet (*i.e.*, 5-10 ms^{-1}) onto the substrate influence the final resolution of the printed feature [140]. In addition, an appropriate distance nozzle-substrate (e.g., 1-3 mm) together with a good wetting and adhesion [96] to the substrate are other requirements for optimal printing. A typical printer used for the printing of electronic applications is the Fujifilm Dimatix shown is Figure 21. It is composed by a platen on which the printing substrate is positioned, being designed to handle flexible films as well. A vacuum system holds the material securely, ensuring adhesion. A maximum temperature of 333K can be set to assist the evaporation of the solvent. A fundamental element of the printer is the print carriage, which is the moving constitutive component of the device, on which a cartridge is mounted; the cartridge can be filled with 0.2-1.5 mL of ink. In the cartridge, there are 16 silicon nozzles arranged in line and connected to a microfluidic circuit, where the liquid is pumped by a piezoelectric actuator causing the ejection of the ink at a velocity of 5 μL per second. The nozzle diameter is 21.5 μm and the nozzle-nozzle distance is 254 μm. It is possible to set the z-axes printing distance between the cartridge and the substrate (usually set at 1 mm). A fiducial camera is mounted in the print carriage; in order to orientate the print carriage, thus providing an image of the substrate when printing. It is also possible to set the reference points that can be memorized in the software and used if the substrate needs to be removed. This allows the possibility to set the printing origin. On the printer there is also the maintenance station (Blotting Pad), in which the cartridge holder is placed in a default position when it is not operating and where

the nozzle cleaning cycles are performed. The cleaning cycles of the nozzles are of great importance and to do this it is necessary to use a pad. The obstruction of the printing nozzles is one of the problems affecting the uniformity of the print. To prevent this, the recommended size of the flakes in suspension is estimated to be maximum 1/50 of the diameter of the nozzle [96]. Finally, a drop watcher gives a real-time view of jetting nozzles, which allows to select the nozzles that have a regular jetting and optimize the parameters. Different kinds of fluids are jettable with this device (from aqueous and solvent based fluids to particle suspensions) within a η range from 2 to 30 mPa·s [195] and a Z number from 1 to 14 [96], [134]. With the help of the Fiducial Camera and of the software provided, different patterns can be set, such as spots, lines or films [196].

Figure 21 - Dimatix Materials Printer DMP-2800 [197].

7.1.3 Screen Printing

In the screen-printing technique a mesh is used to transfer the paste to be printed onto a substrate [136]. The screen is composed of an interlaced mesh of synthetic fabric or steel mesh, which is combined with a masking material called a stencil that defines the areas where the ink should be transferred [136]. There are several mesh counts that can be used based on the detail of the design to be printed. When the screen is ready, a blade or a squeegee is moved on the screen to fill the open mesh with the paste [136]. This causes the paste to wet the substrate and then be removed from the mesh during the inverse passage when the screen returns after the blade has passed [136]. The final thickness of the print, t, is determined by the following relationship [136]:

$$t = V_{screen}\, k_p\, \frac{c}{\rho} \qquad \text{Eq. 27}$$

where c is the concentration (g cm^{-3}) of the solid material in the ink, ρ is the density (g cm^{-3}) of the material in the final film, k_p is the pick-out ratio (which depends on parameters such as squeegee force, printing speed, and snap-off angle/distance), and V_{screen} is the volume of the ink per area of open screen (cm^3 m^{-2}) [136].

7.2 Microfabrication processes

Microfabrication is the process of fabricating miniature structures of micro- and nano- scales. To fabricate a device, many and repeated processes must be performed. These processes typically include depositing a photoresist film, patterning the film with the desired features, and removing (or etching) portions of the film.

7.2.1 Preparation

In order to promote the resist adhesion, substrates must be previously cleaned by ultrasonication in acetone and isopropanol (IPA) [198], [199]. A spin coater is used to deposit the photoresist on the substrate. There are various recipes for obtaining a photoresist layer of the desired thickness provided by the producer of the photoresist and in the literature [198]. The typical parameters to be set on the spin coater are the type of photoresist to be used, the rotation speed, the acceleration and the process time [198]. As a rule of thumb, a thinner resist film usually improves resolution. Positive photoresists also improve resolution compared to negative photoresists [198]. The deposited resist is baked to drive off any remaining solvent before being exposed to intense UV light or to electron beam [199].

7.2.2 Photolithography

UV lithography is a micro-fabrication process used to transfer a geometric pattern from a photomask to a light sensitive polymer-film (photoresist) deposited on the substrate [198], [199]. Quartz masks, transparent to UV, are coated with chromium. Chromium is opaque to the UV light, blocking it from irradiating the resist where present. The process is relatively quick and easy [198]. The exposure to UV light causes a chemical change in the exposed areas which allows removal of the polymer by an alkaline corrosive developer solution (e.g., AZ303 developer) exposing underlying substrate [198],

[200]. Care must be taken at this point not to over or under develop the sample which will lead to either patchy electrodes or else short them out [198], [199]. Metal can then be deposited on the sample, followed by lift-off in another solvent that depends on the resist used, to leave behind the desired metal pattern. The maximum pattern resolution depends by the diffraction limit of the system. For UV light the diffraction limit is defined as $d = \frac{\lambda}{2NA}$ where λ is the wavelength (i.e., λ_{UV} = 100-400 nm) and NA is the numerical aperture [198], [199].

7.2.3 Electron-beam lithography

Electron beam lithography (EBL) is the practice of drawing custom shapes on a surface covered by the photoresist thanks to a focused electron beam [201] in ultrahigh vacuum. The electron beam changes the solubility of the resist, allowing the selective removal of the exposed or unexposed regions of the resist by immersing it in a solvent (under development) [202]. The purpose, as for photolithography, is to create micro- and nano- structures but unlike the latter technique, the diffraction limit is much lower due to the electron wavelength is smaller than that of the UV photons, achieving sub-10 nm resolution [202]. On the other hand, among the disadvantages, EBL has a low throughput, limiting its use to the manufacture of photomasks [202], to the low volume production of semiconductor devices and to research and development.

7.2.4 Metallization

Metallization is the general name for the technique of coating metal on the surface of objects [203]. Vacuum metallization involves heating the desired metal to its melting point in a vacuum chamber, then letting condensation of vaporized metal on the substrate's surface [203]. Alternatively, metal films of higher roughness can be deposited by sputtering a metallic target with energetic ions and exposing the sample to the beam of sputtered metal atoms [203]. Many processes are possible to melt the metals. In the case e-beam metallization, the electrons are generated by a heated filament, extracted and directed to the metal under a high vacuum [203]. The kinetic energy of the electron beam is transformed into thermal energy when in contact with the metal, resulting in a concentrated heat source for melting [203]. Low pressures are needed to allow molecular flow conditions for the metal vapours so that the film forms uniformly on the substrate [203]. The vacuum system consists of a compression pump and a turbomolecular pump to reach pressures in the order of 10^{-7} Torr to

allow passage of electrons from the electron gun to the evaporation material. A magnetic field is used to direct the electron beam from its source to the ingot location.

8 2D CRYSTAL-BASED INKS FOR ELECTRONIC DEVICES

This chapter provides a detailed morphological and structural characterization of 2D crystal-based inks (graphene pastes for antennas and supercapacitors and InSe-based ink for photodetectors). The samples were produced using both sonication-assisted and WJM-assisted LPE. Several techniques have been used to study the physical and chemical properties of crystals. The morphology was evaluated in terms of lateral dimensions (TEM) and thickness (AFM) while the structural properties were carried out by Raman spectroscopy. Furthermore, a rheological study has been required to evaluate the suitability of 2D crystal-based inks for the application under consideration. The information obtained from the characterization techniques allow a complete evaluation of the properties of the materials, providing an in-depth understanding of their morphological properties.

In this thesis, exfoliation of graphite in N-methyl-2-pyrrolidone (NMP) by WJM has been performed in order to obtain the graphene dispersion used in my applications. A mixture of the bulk layered crystals (200 g of graphite flakes +100-mesh from Sigma Aldrich) and the solvent (20 L of NMP, Sigma Aldrich) was prepared. The mixture was placed in the container and mixed with a mechanical stirrer (Eurostar digital Ika-Werke). For the +100-mesh graphite the 0.30 mm nozzle aperture was used. The piston-pass, defined as the number of times the piston was charged and discharged with solvent/layered crystal, was set to 1000 passes (10 mL per pass). The processed sample was then collected in a second container. The wet-jet milling process was repeated passing the sample through the 0.15 mm nozzle. Finally, the nozzle was changed to 0.10 mm diameter and a third exfoliation step was carried out.

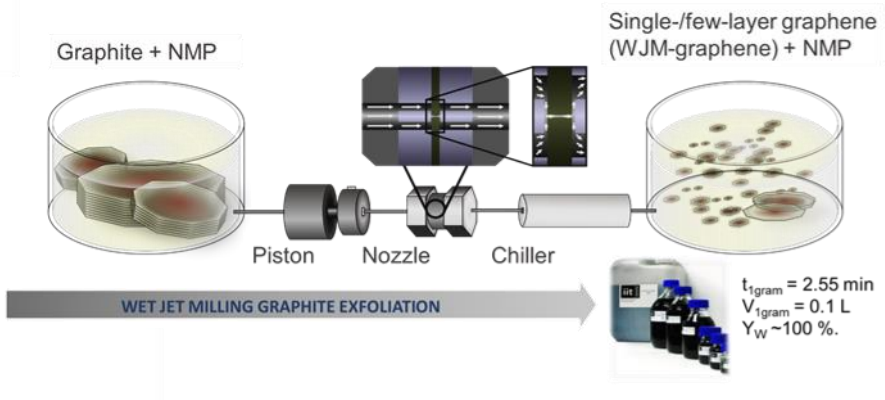

Figure 22 - Schematic illustration of the production of single-/few-layer graphene by wet-jet milling (WJM) exfoliation of graphite (WJM-graphene) [119].

On the other hand, β-InSe single-crystals, produced by modified Bridgman-Stockbarger method [72], are exfoliated by ultrasonicated-assisted LPE followed by SBS, in IPA (ACS Reagent, ≥ 99.8%, Sigma-Aldrich). The choice of IPA as a solvent is due to its nontoxicity and low boiling point, aiding the material processing and deposition [204]. Additionally, IPA has been successfully used to exfoliate other layered crystals such as GaS [67], [205], GaSe [205], and TMDs [110]. 40 mg of β-InSe single crystals have been pulverized in a mortar and ultrasonicated in a sonic bath (Branson 5800 cleaner, Branson Ultrasonics) for 6 h, after the addition of 20 mL of IPA. During the ultrasonication process the bath temperature has been kept in the 25 - 35 °C range. Sonication and ultra-centrifugation at 1000×g of β-InSe single-crystals are performed to obtain a stable dispersion of exfoliated β-InSe flakes.

8.1 Graphene-based pastes for printed bow-tie antennas

In order to develop a light, cheap and low-energy consuming antennas, graphene is a suitable candidate thank to its unique properties (see Graphene properties at page 12). In fact, metals are expensive [206] and metal production and processing activities can cause significant pollution. The production and processing of metals can cause air pollution, diseases related to the presence of waste products, and contamination from accidental chemical spills. Therefore, new technological solutions would be needed to replace metal circuits with disposable and environmentally friendly materials [206]. From the point of view of the materials used, an alternative to metal-based antennas is the use of conductive graphene-pastes due to their low cost, their low toxicity compared to many metals (for example, nickel [207]) and their stability over time.

8.1.1 Graphene-based ink production and characterization

Firstly, a few layer graphene (FLG) dispersion in N-methyl pyrrolidone (NMP) is produced by WJM-assisted LPE. The flake lateral size and thickness are analysed by TEM and AFM respectively. Examples of TEM and AFM images, as well as the results of the corresponding statistical analyses on flake lateral size and thickness, are reported in Figure 23. From lateral size and thickness statistics it is found that flakes are 460 nm large (Figure 23b) and 1.6 nm thick (Figure 23d). Although the thickness of SLG is ~ 0.3 nm [208], we need to consider its interaction with the substrate interface resulting in an AFM thickness of ~ 0.9 nm when deposited on a SiO_2 substrate [209]. Therefore, the thickness value obtained validates the predominant presence of FLG in the dispersion. The structural

properties of the produced flakes are also characterised by Raman spectroscopy to confirm the flake thickness and get information about the presence of defects. The Raman spectrum of graphene presents characteristic features (see Raman spectroscopy at page 31).

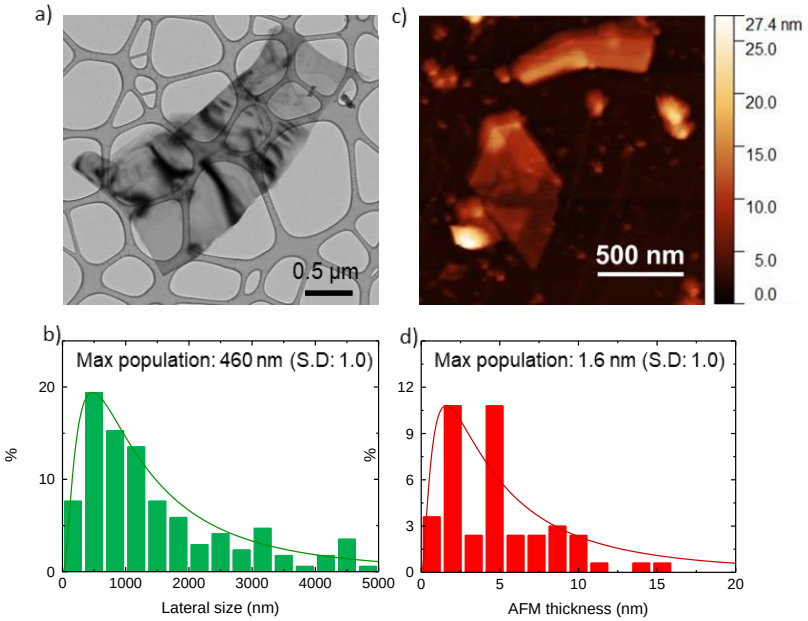

Figure 23 - a) Representative TEM image of graphitic flakes obtained by LPE and b) corresponding statistical analysis of the lateral size distribution. c) Representative AFM image of the graphitic flakes and d) AFM statistical analysis of the thickness distribution [210].

Figure 24a shows a typical Raman spectrum of FLG (light blue line) produced as shown above as well as the starting graphite spectrum (dark blue line) for comparison, while the Figure 24b shows that the dispersion is mainly composed of FLG flakes.

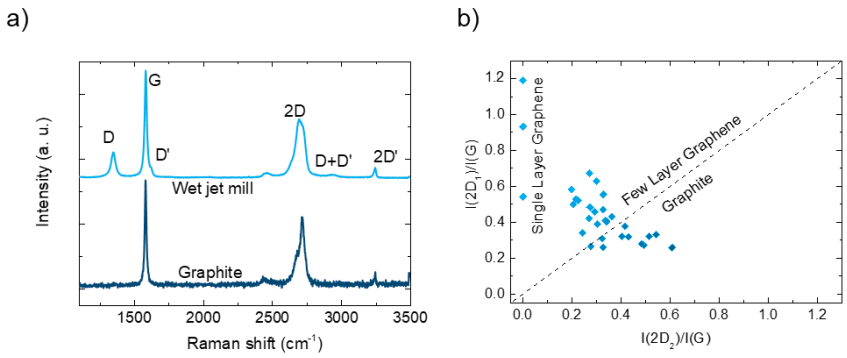

Figure 24 - a) Raman spectra of graphite and of the as-prepared sample. The most typical Raman modes of graphite and graphene are indicated. b) Plot of the intensity of the $2D_1$ component vs $2D_2$. In graphite samples $2D_2$ is twice as intense as $2D_1$, while in SLG the $2D_2$ intensity is negligible [210].

This result validates the result of the AFM analysis. Although exfoliation with NMP is very advantageous in terms of yield, stability and concentration [118], its use is strictly regulated due to its teratogenic effects. Currently, it is listed in the ECHA's Candidate List of substances of very high concern and in 2017 EPA limited its use in paints and coatings [211], [212]. As a result, the use of NMP must be limited due to safety measures and pollution control. In this work, its use has been limited only in the exfoliation phase and a FLG powder has been produced using the process described in the following section.

8.1.2 Paste production and characterization

Initially, the FLG dispersion obtained by LPE has been dried by means of a rotary evaporator (Heidolph Hei-vap precision) at 70°C and 2 mbar. The obtained suspension is then washed with acetone and dried again in the rotavapor at 40°C and 400 mbar. The resulting dry crust is then dispersed again in dimethylsulfoxide (DMSO) and the resulting suspension is lyophilized (Martin Christ, Alpha 2-4 LDplus) to obtain a graphene powder. The higher melting point of DMSO (19°C) and its lower boiling point (189°C) [204] make it more suitable for lyophilization than NMP (melting and boiling points -21°C and 202°C, respectively) [204]. The powder obtained by freeze-drying is gradually mixed with a commercial acrylic overprint varnish (Hydrolac 610 L, Eston Chimica). For a better homogeneity the mixture has been kept under stirring during the mixing process. The concentration of graphene in solution is 115 g L^{-1}. Finally, 25 g of commercial silver (Ag) solvent-based ink for flexographic printing (Sun Chemicals, silver T312) are added to the acrylic-based graphene-based ink to further increase its conductivity. During this phase, the viscosity was reduced compared to the original mixture, adding 50 ml of IPA. The results of the rheological characterization of all inks are shown in Figure 25a. All the measurements were performed with a rheometer equipped with a concentric cylinder geometry (TA Instruments HR-2). The FLG dispersion obtained from WJM is about two orders of magnitude less viscous than the silver ink used in flexographic printing (2.4 mPa s and 0.20 Pa s at 100 s^{-1}, black and blue lines, respectively) while the overprint varnish viscosity is only slightly lower than that of the silver ink (~ 0.16 Pa s, green line). The graphene/silver mix and the commercial silver ink show a very similar viscosity for shear rates between 20 and 200 s^{-1}. The solid content of both the commercial and the FLG/Ag inks are estimated by thermogravimetric analysis (TGA). The TGA was performed using a TGA Q500-TA instrument. The samples are heated from 30°C to 800°C at the heating rate of 10 °C min^{-1} under nitrogen atmosphere (N_2 flow rate 50 ml min^{-1}).

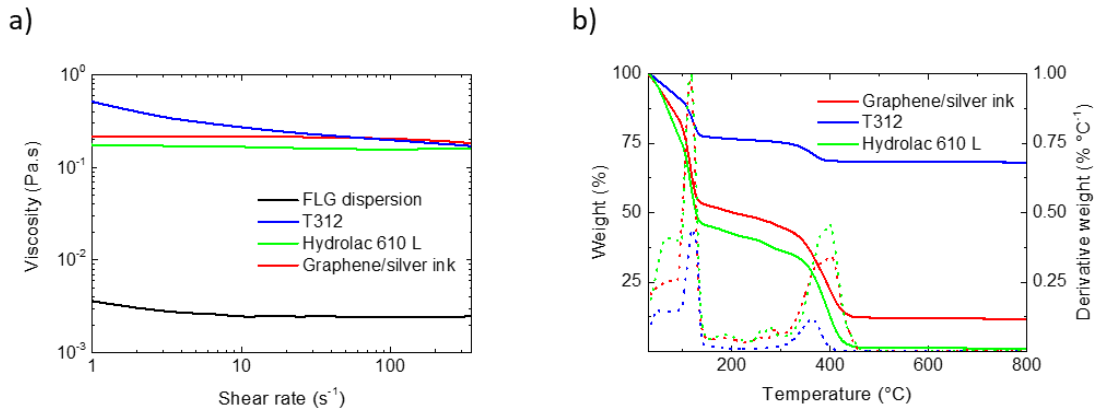

Figure 25 - a) Viscosity of the different inks used, as a function of the shear rate. The FLG dispersion obtained by WJM is shown in black while blue, green and red lines represent the commercial silver ink (T312), the acrylic overprint varnish (Hydrolac 610 L), and the final FLG/silver ink, respectively. b) Weight percents (solid lines) and derivative weight percents (dashed lines) estimated by TGA, as a function of temperature. Blue and green lines represent the commercial silver ink and the acrylic overprint varnish, respectively, while the graphene/silver ink is shown in red [210].

The measured weights and their derivatives are shown in Figure 25b as a function of temperature, while the residual solid contents at 750°C are reported in Table 1, column 1. Data reported in Table 1, column 2 shows that the ratio between silver and FLG is ~ 14.8% by weight. From the data it is possible to estimate the solid content of FLG/silver ink. In fact, solid content of Hydrolac 610L is 39 ± 1% by weight, while the percentages by weight of silver and FLG in dry printing they are ~ 3.1% by weight% and 21.1% by weight respectively, so FLG/silver ink is ~ 45.5% (see Table 1, columns 3-4).

Table 1 - Ink composition and dry content estimated by TGA

	Solid content (@750°C)	*Ink formulation*		*Ink solid content*	*Dry content*
Hydrolac 610L	1.0 wt%	1060 g	(88.3 wt%)	34.5 wt%	75.8 wt%
T312	68.2 wt%	25 g	(2.1 wt%)	1.4 wt%	3.1 wt%
WJM Graphene	--	115 g	(9.6 wt%)	9.6 wt%	21.1 wt%
FLG/silver ink	11.8 wt%	1200 g	(100 wt%)	45.5 wt%	100.0 wt%

8.2 Graphene-based pastes for screen-printed supercapacitors

Scalable production of materials for their application on supercapacitors, as well as the implementation of high-performance production techniques, is crucial for their diffusion. WJM has been used to produce graphene ink to be used for screen-printed SCs on flexible substrates. The formulation of aqueous alcohol graphene inks, as well as the addition of single walled-carbon nanotubes (SWCNTs), allows for the screen printing of interdigitated structure on plastic substrate for metal-free, flexible, solid-state and washable SCs.

8.2.1 WJM graphene dispersion production and characterization

By processing graphite through WJM, graphene dispersion has been obtained as nanostructured active material for supercapacitors. The lateral size and thickness of the as-produced WJM-graphene dispersion have been characterized by means of TEM (Figure 26a) and AFM (Figure 26c) finding irregularly shaped (Figure 26a) and nm-thick flakes. Statistical analysis indicated flakes with a thickness of ~ 1.1 µm and a lateral size of ~ 3.2 nm. Raman spectroscopy characterization has been carried out in order to evaluate the structural properties and the quality of the as-produced WJM-graphene dispersion. Figure 27 shows the comparison between the Raman spectra of the graphite taken as a reference and WJM-graphene.

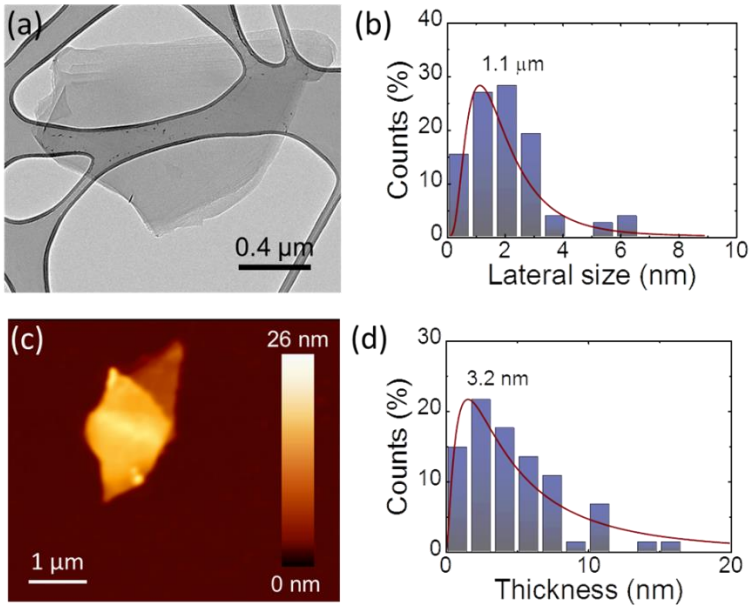

Figure 26 - (a) TEM image and (b) statistical analysis of the lateral dimension of WJM-graphene (acquired on 80 flakes). (c) AFM image and (d) statistical AFM analysis of the thickness of the WJM-graphene (acquired on 80 flakes) [119].

From Figure 27 it is possible to see that the intensity of D and D' bands in WJM-graphene is bigger than the intensity in graphite. Moreover, Raman statistical analysis shows that I(D)/I(G) ranges from 0.1 to 1.2 for WJM-graphene, while in graphite I(D)/I(G) approaches to 0 (Figure 28a). For WJM-graphene, Pos(G) and FWHM(G) range from 1578 to 1583 cm^{-1} (Figure 28b) and from 14 to 25 cm^{-1} (Figure 28c), respectively.

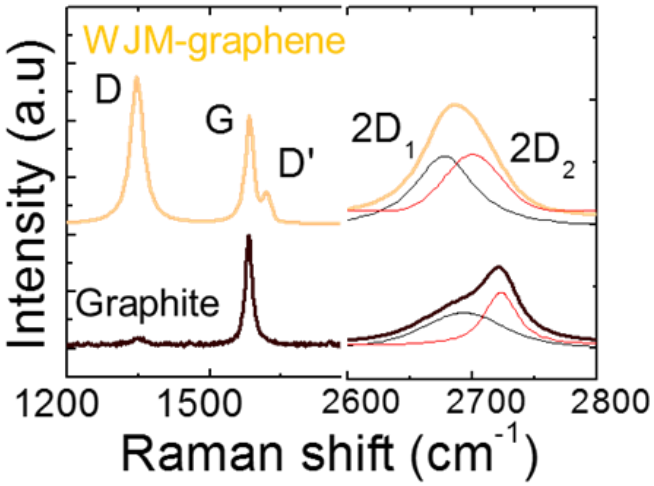

Figure 27 - Comparison between the Raman spectra of the graphite (black) and WJM-graphene (orange), with their multi-peak Lorentzian fitting showing the contribution of the individual modes (black line: $2D_1$; red line: $2D_2$) [119].

The plot of I(D)/I(G) vs. FWHM(G) (Figure 28d) shows the absence of any correlation, which means that the WJM process has not induced in-plane defects [213], [214]. The normalized intensity ratios $I(2D_1)/I(G)$ vs. $I(2D_2)/I(G)$ gives a view of the flakes thickness (Figure 28e). The dashed line $I(2D_1)/I(G) = I(2D_2)/I(G)$ in Figure 28e roughly represents the multilayer condition. These results, together with the AFM measurements, confirmed that WJM-graphene is enriched in single-/few-layers graphene flakes. The chemical composition of the WJM-graphene has been determined by X-ray photoelectron spectroscopy (XPS) measurements. Figure 29 reports the C 1s spectrum of WJM-graphene, which can be decomposed into different components. The main one peaks at 284.4 eV and is referred to sp^2 carbon with the corresponding feature due to π-π^* interactions at 290.8 eV.

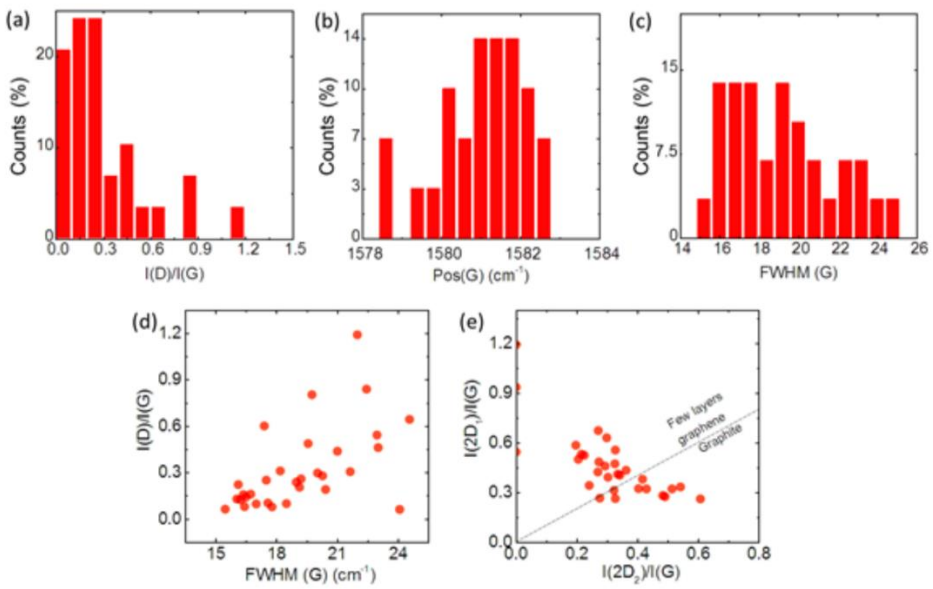

Figure 28 - Raman spectroscopy measurements analysis for WJM-graphene. Statistical analysis of: (a) I(D)/I(G). (b) Pos(G) and (c) FWHM(G). (d) Plot of I(D)/I(G) vs. FWHM(G). (e) Plot of $I(2D_1)/I(G)$ vs. $I(2D_2)/I(G)$. The dashed line $I(2D_1)/I(G) = I(2D_2)/I(G)$, representing the multilayer condition (~5 layers), is also shown [119].

A second component, centred at 284.8 eV, refers to the sp^3 carbon and is due to flake borders and solvent residuals. Two other weak contributions, equal to ~10 % of the total carbon amount, can be ascribed to C-N and C=O groups (peaks at binding energies of 286.3 eV and 287.7 eV, respectively) [215], [216]. Likely sp^3 carbon, these nitrogen and oxygen groups come from residual NMP molecules [215]. These results confirm that high-quality graphene flakes are effectively obtained by WJM, in accordance with the previous analysis.

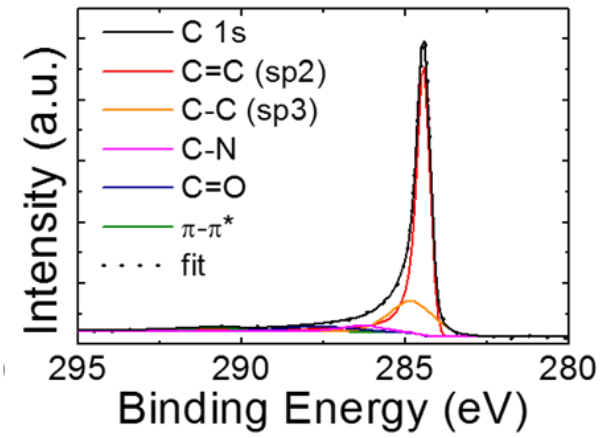

Figure 29 - C 1s XPS spectrum of the WJM-exfoliated. Its deconvolution is also shown (dashed black line), evidencing the bands ascribed to: C=C (red line), C-C (orange line), C-N (magenta line), C=O (navy line), π-π (olive line)* [119].

8.2.2 Paste production and characterization

Screen printing technique requires careful tailoring of the viscosity and surface tension of the ink formulation in order to provide non Newtonian fluids with pseudoplastic and thixotropic properties [217], [218]. The latter allow the ink to be optimally transferred on the substrates, with the ink only flowing only when sheared by the squeegee and minimal spreading once printing [217], [218]. Furthermore, the ink must be sufficiently volatile in order to facilitate the drying and curing process of the printed device, potentially improving the process productivity (i.e., the ultimate profitability), [217], [218] retaining the ink viscosity [219], [220] during the printing as well as avoiding the so-called "drying-in effect" (i.e., the drying of the ink in the mesh) [219], [220].

Then, in order to obtain a printable ink, the as produced WJM-graphene was dried and re-dispersed in a mixture of H_2O/EtOH (70:30) and terpineol (1 wt%) (solvent exchange process) [221] with a concentration of 80 g L^{-1}. Terpineol was used for adjusting the ink surface tension to suitable values for printing on plastic substrates, in agreement with previous reports on graphene-based ink [196], [222]. The addition of SWCNTs (25 wt%) into WJM-graphene ink was also evaluated as active ink. The SWCNT were prepared by dissolving as-purchased SWCNTs in EtOH at a concentration of 10 g L^{-1} using ultrasonication based debundling. The dispersion was sonicated using a horn probe sonic tip (Vibra-cell 75185, Sonics) with a vibration amplitude set to 45% and a sonication time of 30 min. The sonic tip was pulsed at a rate of 5 s ON and 2 s OFF to avoid damage to the processor and to reduce any solvent heating. An ice bath was used during sonication in order to minimize heating effects.

8.3 InSe-based inks for photodetector devices

In order to evaluate the concentration of the dispersed β-InSe flakes, optical extinction measurements have been performed using a Cary Varian 5000 UV-Vis. Exfoliated β-InSe flake dispersions in IPA were diluted 1:10 with the pure solvent. The extinction spectra of the pure IPA (baseline) has been subtracted from the sample spectrum. Figure 30 shows a typical β-InSe extinction spectrum. It is characterized by two picks at ~ 275 nm and at ~ 360 nm. They are related to the maxima in the imaginary part of the dielectric function connected to the direct transitions from the valence band to the conduction band [223]. The concentration of the dispersion is estimated by the Beer-Lambert law, with ε = 580 L g^{-1} m^{-1} @ 600 nm [224], obtaining a concentration of 0.11 g L^{-1}.

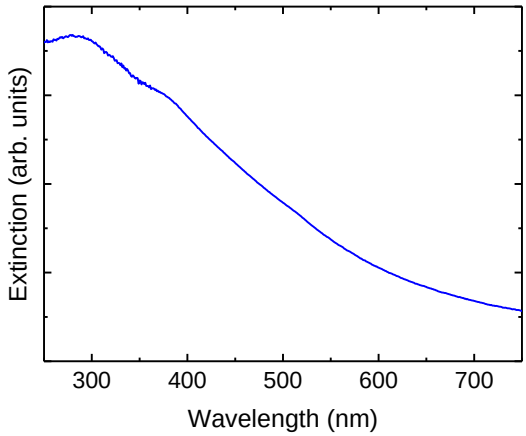

Figure 30 - Extinction spectrum of the β-InSe sample.

Morphological, chemical and structural analyses as well as the elemental composition and lattice structure analysis of β-InSe have been evaluated. Representative TEM and AFM images for β-InSe are reported in Figure 31a and Figure 31b, respectively.

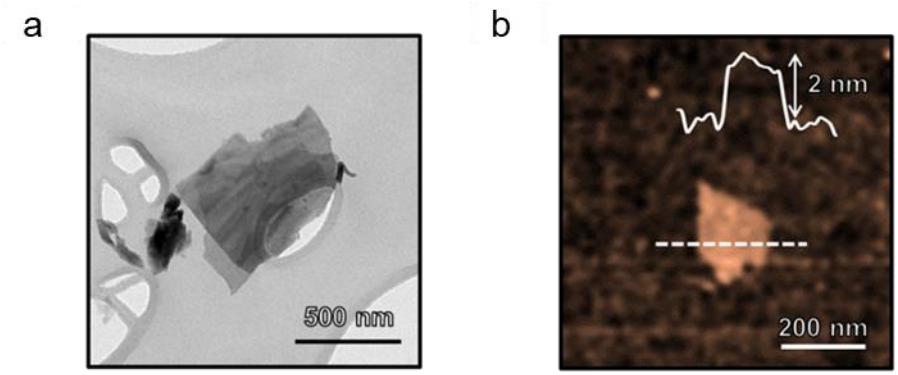

Figure 31 - a) Representative TEM image of an isolated β-InSe flake; b) Representative AFM image of an isolated β-InSe flake [225].

Samples for the TEM measurements have been prepared by drop-casting the exfoliated InSe flake dispersions onto carbon-coated Cu grids with successive drying under vacuum overnight. From statistical analysis, fitted by a log-normal distribution [117] (Figure 32), it is found that β-InSe flakes have a lateral size of ~ 113 nm ($\sigma = 0.84$) and a thickness of ~ 4 nm ($\sigma = 0.54$). Therefore, according to a β-InSe monolayer thickness of about 0.9 nm [226], single/few-layer β-InSe flakes are actually produced with a Se–In–In–Se structure.

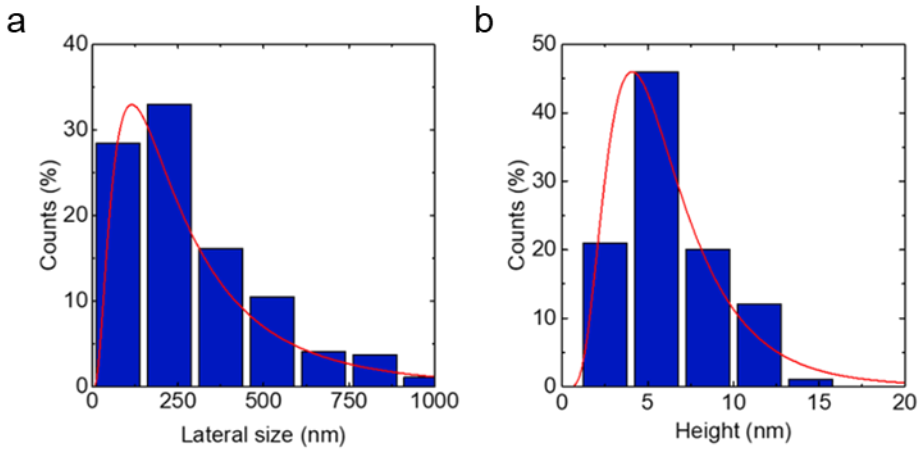

Figure 32 - a) Lateral size and b) thickness statistical analyses for β-InSe flake dispersion [225].

XRD measurements (Figure 33) confirm the presence of hexagonal β-InSe, both for bulk and for exfoliated samples, having calculated lattice parameters of a = b = 4.005 ± 0.004 Å and c = 16.660 ± 0.004 Å. The crystal structure has been characterized by XRD using a PANalytical Empyrean with Cu Kα radiation. The samples for XRD have been prepared by drop-casting exfoliated InSe flake dispersions onto Si substrates and drying them under vacuum. β -InSe bulk crystals present only peaks belonging to the plane family (00l), indicating the presence of crystalline flakes that are highly oriented along the c axis. On the other hand, the exfoliated β -InSe flakes, show planes with different orientations (e.g., 010, 011 and 110). This is due to disordered arrangement of the nanocrystals, while a strong preferential orientation of the (001) plane is still present.

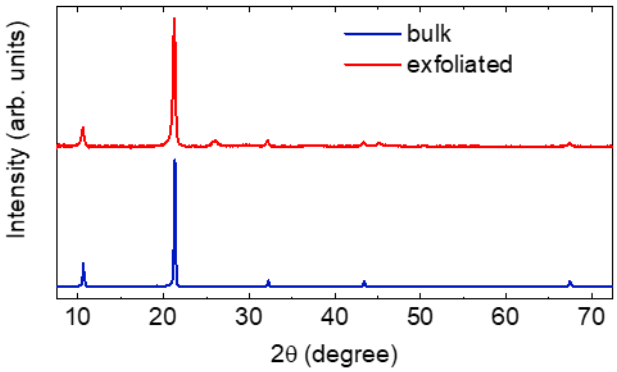

Figure 33 - XRD spectra for bulk β-InSe (blue trace) and exfoliated β-InSe (red trace) samples [225].

The absence of other chemical species, (e.g., In_2Se_3, In_2O_3) that could have been formed during the exfoliation process or during exposure to atmosphere has been demonstrated by Raman spectroscopy

measurements as shown in Figure 35. Exfoliated β-InSe flake dispersions have been drop-casted on Si/SiO_2 substrates and drying them under vacuum. The spectra were fitted with Lorentzian functions. Six Raman active vibrational modes ($2A_{1g}$, $2E_{1g}$, $E1_{2g}$, A2u - Figure 35) [224] have been found in both bulk and exfoliated β-InSe samples. The data confirms the absence of polymorph crystals. Peaks related to other In and Se compounds or oxidized phases are not present, suggesting that the exfoliated flakes keep their crystalline integrity.

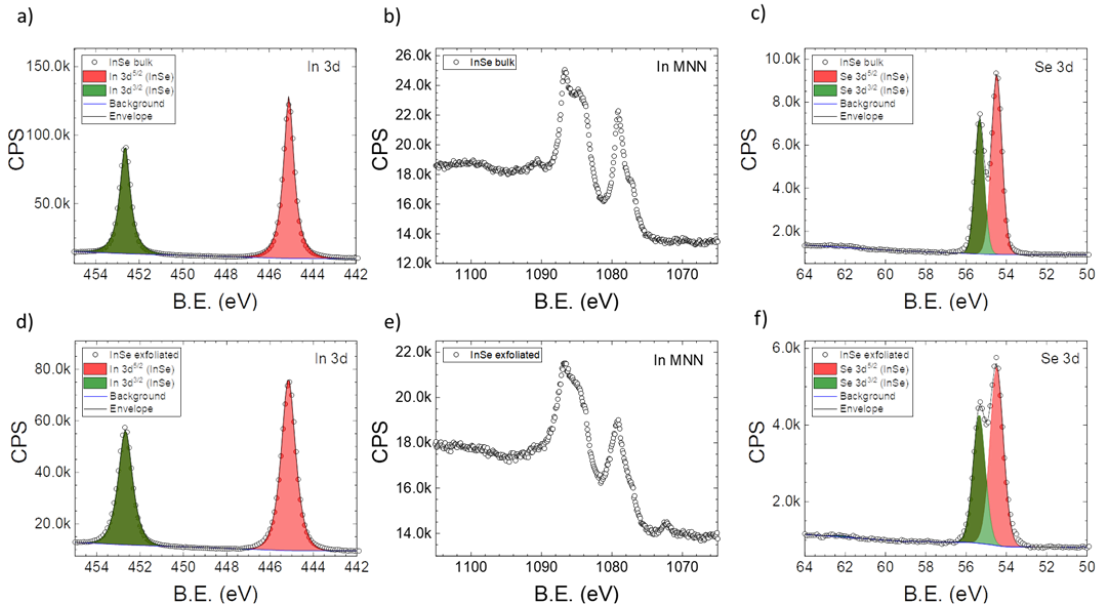

Figure 34 - X-ray photoelectron spectroscopy characterization of bulk (top) and exfoliated (bottom) β-InSe nanoflakes. The In 3d XPS region in the a) bulk and d) exfoliated material is characterized by a spin-orbit split doublet with components (3d5/2,3d3/2) at 445.1 eV and 452.7 eV. We observe a 0.2 eV increase in the width of the peak (FWHM) in the exfoliated material, that can be ascribed to slight oxidation and small fraction of defects, although we could not resolve more specific features of these species. The In MNN Auger region shows comparable structure in the b) bulk and e) exfoliated sample, confirming that the chemical state of In is not significantly perturbed by liquid phase exfoliation in IPA. Similarly, the Se 3d XPS region in the c) bulk and the f) flakes shows 3d5/2 and 3d3/2 components at 54.5 and 55.3 eV respectively, with a ~0.2 eV increase of the lineshape in the exfoliated sample. We did not detect oxidized Se species.

These conclusions are also supported by X-ray photoelectron spectroscopy (XPS) spectra of the In 3d and Se 3d regions (Figure 34), showing only a 0.2 eV broadening of the peaks in the exfoliated material, indicative of a minor increase in defects and oxide species compared to the bulk, and the XRD patterns shown in Figure 33, which agree with the diffraction of β-InSe (D_{46h} symmetry, P63/mmc space group, ICDD 98-018-5172). The XPS analysis has been performed on a Kratos Axis UltraDLD spectrometer at a vacuum better than 10^{-8} mbar, using a monochromatic Al K α source operating at 20 mA and 15 kV and collecting photoelectrons from a 300 × 700 μm^2 sample area. Wide

spectra were acquired at pass energy of 160 eV and energy step of 1 eV, while high-resolution spectra of were acquired at pass energy of 10 eV and energy step of 0.1 eV. The samples were prepared by drop-casting the dispersion of InSe nanoflakes on Au-coated Si chip in N_2 atmosphere while heating the substrate to 60°C. Bulk InSe crystals were sticked on conductive carbon tape and cleaved prior analysis. The samples were transferred to the XPS chamber in inert atmosphere.

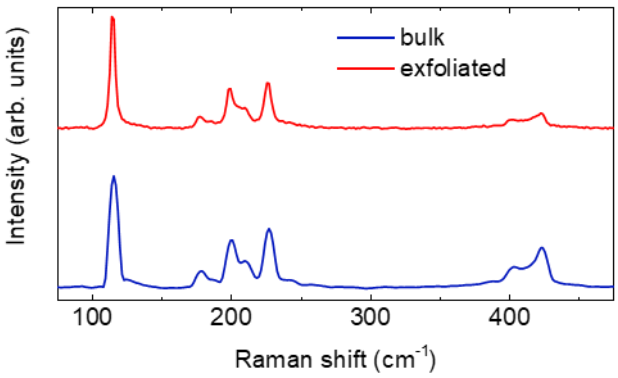

Figure 35 - Raman spectra for bulk β-InSe (blue trace) and exfoliated β-InSe (red trace) samples [225].

The ink has exhibited low viscosity ($\eta_{25°} \approx 3.2$ mPa · s @ 25°C), with Newtonian behaviour at shear rates between 0.2 and 300 s^{-1} (Figure 36), which makes them suitable for spray coating deposition [227].

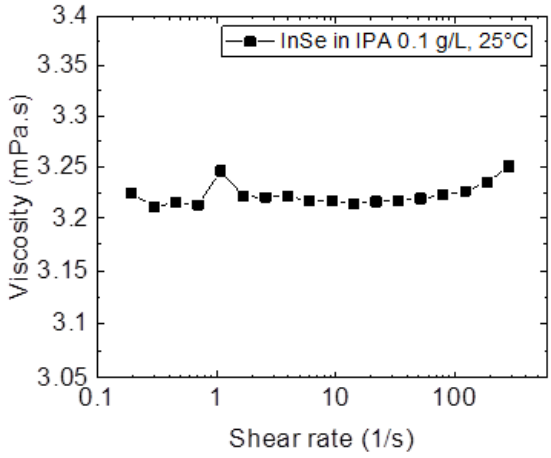

Figure 36 - Viscosity as a function of shear rate measurement of the InSe ink in IPA [225].

9 BOW TIE ANTENNA

In recent years, interest in Radio Frequency Identification (RFID) technology has increased [228] often claiming to have the potential of replacing barcodes [228]. The global RFID technology market is expected to reach $ 38.0 billion by 2021 from $ 16.2 billion in 2016 with a compound annual growth rate of 18.6%, from 2016 to 2021 [228]. Cost is currently considered the main limiting factor for the diffusion of RFID tagging in packaging and logistics, with a limiting target of 5 cents per tag for tracking of fast-moving consumer goods [228]. The RFID-tag costs can also be higher if used for valuables or in healthcare [229]. Usually, RFID tags consist of a flexible metal planar antenna connected to a silicon chip and laminated between two plastic films [164]. A pressure sensitive adhesive is applied to the back of the plastic film to create a sticker that can be attached [164]. The production of disposable antennas generally involves the patterning and chemical etching of metals to create the conductive circuits of the antenna [164]. Chemical etching is a process that includes many phases and requires numerous pollutants, which could also damage the underlying substrate and therefore limit the number of substrates suitable for producing antennas. A key goal for modern technology is to replace metals with lighter, less expensive materials less energy-consuming for antenna realization. This goal is challenging, due to the difficulty of achieving the high conductivity of metals ($> 10^7$ S m^{-1} for copper) and their excellent mechanical properties if shaped in thin films. Furthermore, the use of green technology-based approaches should be a must [230]. In this context, a way to overcome the use of techniques such as patterning and chemical etching is the printing of conductive ink solutions (see Deposition techniques at page 56). This approach has low production costs and may be suitable for industrial scale-up. The graphene-based paste produced in the previous chapter is a valid alternative to the current metal-based technology. In this work, the Bow-tie antenna design has been chosen for its optimal compromise between ease of implementation and efficiency [231]. For these reasons, Bow-Tie antennas can be used for the development of ultra-wideband RFID in intelligent printed electronic applications (e.g., personal wireless systems like Wi-Fi, Bluetooth, WiMAX and SWNs or sensing applications) since their low-cost [232], [233].

9.1 Design

The Bow-tie antenna (BTA) design is shown in Figure 37. BTA has been dimensioned to have an input impedance of 50 Ω using the graphene-based paste (section Graphene-based pastes for printed bow-tie antennas at page 63) as conductive material. The working frequency is 2 GHz, which is one

of the frequencies available for RFID (ISM radio band [234], [235]). The dimensions for the BTA are described in detail in Table 2. To contain production costs, it is desirable to minimize the amount of paint used per item, while maintaining good radiation efficiency. For this reason, a thickness of 130 µm has been chosen in order to optimize the quantity of graphene paste used while maintaining low ohmic losses.

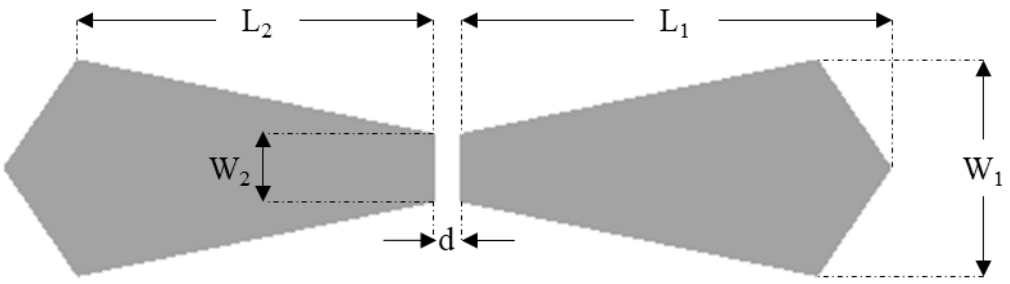

Figure 37 - Scheme of the bow-tie antenna [210].

To perform the RF measurement, the BTA have been fed with a coaxial cable soldered along the centre of the antenna in order to minimize the impact of the antenna feed cable on the BTA. For the use of the antenna in a commercial application, a chip (e.g., balun) should be connected to adapt a balanced line and an unbalanced line or to connect lines with different impedance.

Table 2 - Antenna dimensions

L_1	L_2	W_1	W_2	d
70 mm	57.8 mm	35 mm	11.5 mm	4 mm

9.2 Realization

To realize the BTA, the ink has been stencil printed on cardboard foil at room temperature. An acetate stencil (3M PP2410) having the BTA shape, has been placed over a cardboard paper. As shown in Figure 38, 2ml of ink have been spread on the cardboard by means of an adjustable gap applicator (ZUA 2000 Universal Applicator, Zenther). A thickness of 130 µm (with respect to the top of the stencil) has been set according with the specification chosen in the design phase (Design at page 75). The so produced BTA is then air-dried at room temperature overnight.

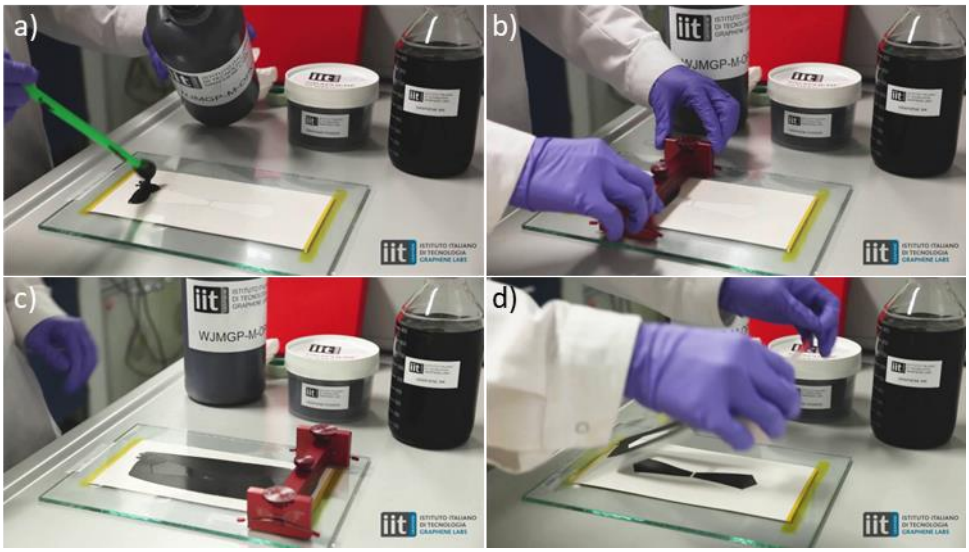

Figure 38 - Process steps. a) deposition of the graphene-based paste, b-c) spread of graphene-based paste on the paper cardboard, d) acetate stencil removal [210].

9.3 Morphological characterization

AFM and SEM pictures of a print are reported in Figure 39. The print surface appears relatively smooth (Figure 39a) with an RMS roughness, estimated by AFM, of ~ 0.7 µm. The SEM fractography (Figure 39b) shows a homogenous distribution of the flakes across the cross-section. The graphene flakes are mostly oriented parallel to the surface. Unfortunately, the mechanism that is responsible for flake orientation is far from clear [236].

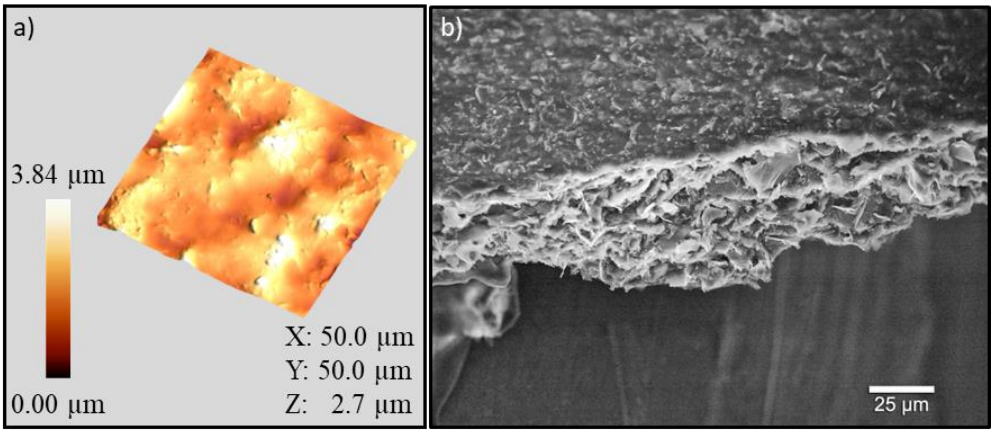

Figure 39 - a) AFM picture of the surface of the print. b) SEM fractography of the print. It can be noted how the graphene flakes are mostly oriented in-plane with respect to the layer [210].

9.4 DC and RF characterization

The printed pattern resistivity is measured in four-probe configuration by a RM3000 Test Unit (Jandel Engineering) equipped with a cylindrical probe having four in line electrodes spaced 1 mm apart. The average resistivity is 0.64 ± 0.06 Ω cm. The typical dry print thickness is about 125 ± 6 µm, resulting in a sheet resistance of ~50 Ω sq^{-1}. The electromagnetic behaviour of the antenna is studied by evaluating the return loss (S_{11}) and the radiation pattern analysis. S_{11} is measured using a Hewlett-Packard 8720C Vector Network Analyser (VNA). A LPRS Straight 50Ω SMA connector, welded to the terminal with the CircuitWorks silver-Epoxy conductive paste, has been used to connect and excite the bow-tie antenna (Figure 40). The measured return loss (S_{11}) of a printed antenna is reported in Figure 41. It presents a bandwidth of 900 MHz, corresponding to a reflected power lower than 10% around the centre frequency of 2 GHz, which covers the frequency range from 1.65 to 2.5 GHz in the L-band the and S-band [237] as shown in Figure 41. The nature of the bow-tie shape of the half-wavelength dipole antenna body allows for a broadband operation.

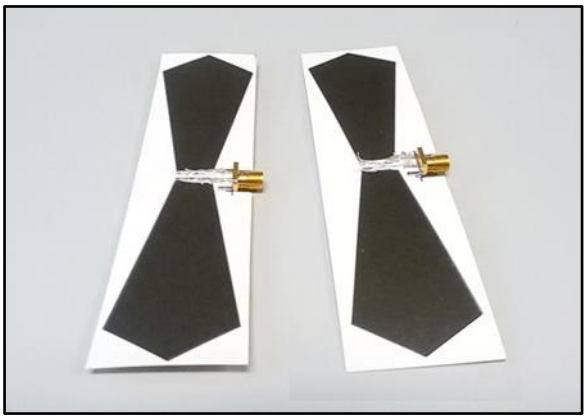

Figure 40 - Printed antennas with SMA connector assembled for electromagnetic measurements [210].

The radiation patterns of the printed antenna are measured in an anechoic chamber at 2 GHz. The measurement scenario and the radiation patterns on the two main polarization planes are reported in Figure 42. The antenna presents a dipole-like behaviour. In fact, the radiation pattern of the E-plane (Figure 42c) is almost uniform (omnidirectional) at 2 GHz with a maximum gain of 0.4 dBi, while the H-plane (Figure 42d) presents a minimum lobe at 90° and 270° and a maximum lobe at 0° and 180°.

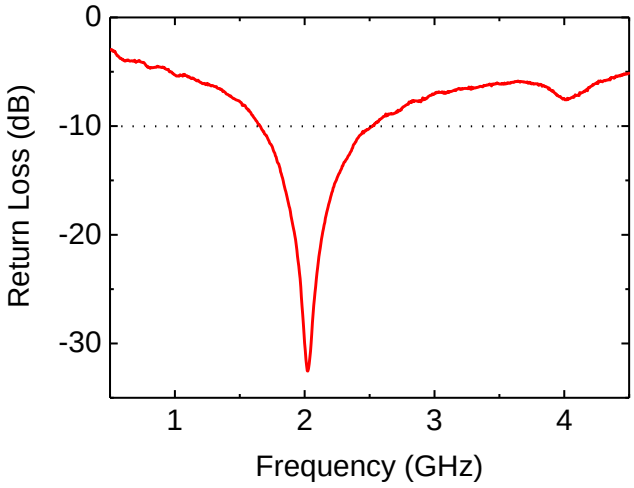

Figure 41 - Return loss (S_{11}) of a printed antenna [210].

The calculated efficiency is 33.2%, with a minimum gain of 1.1 dBi and 1.4 dBi in the H-plane and e E-plane, respectively. All these features demonstrate that the antenna is suitable for a wide variety of applications including satellite communications [238], mobile service [239], digital audio broadcasting [240], astronomy [234] and RFIDs [163], [228], [235].

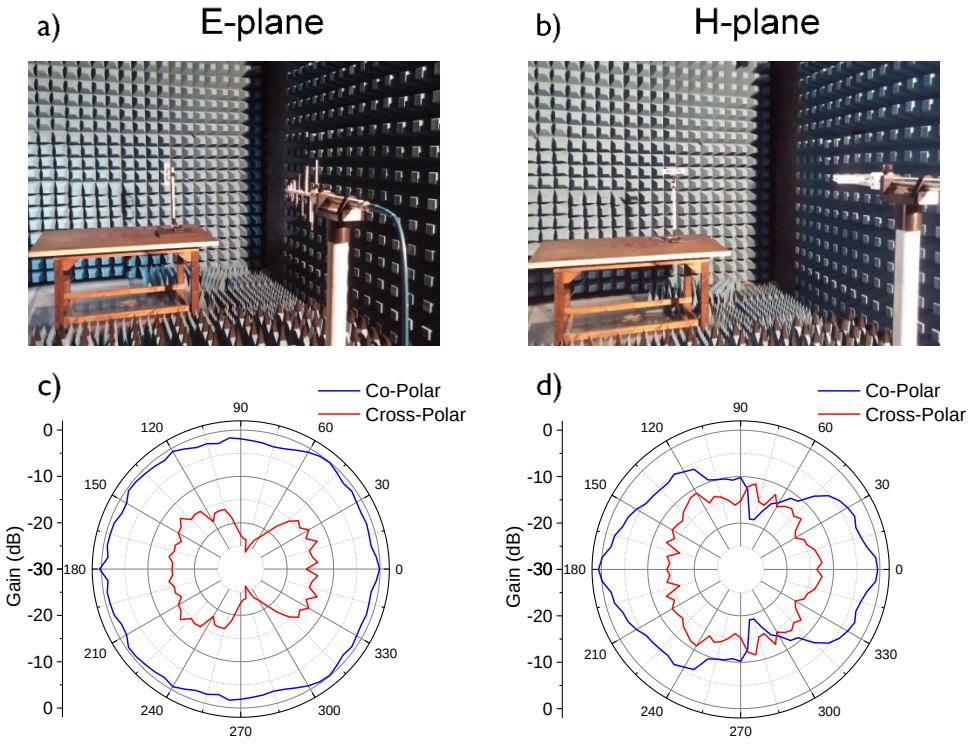

Figure 42 - Pictures of the measurement configuration (a,b) and of the radiation pattern of a printed antenna (c,d) in the E- and H-planes, respectively [210].

10 INSE PHOTODETECTOR

To use 2D materials in (opto)electronic applications, five requirements are necessary:

- high mobility of charge carriers;
- the bandgap range depending on the detector type and application;
- the possibility of obtaining highly crystalline samples by exfoliation;
- environmental stability;
- high flexibility combined with a sufficiently high fracture resistance.

Different classes of materials do not satisfy the above conditions for different reasons. For example, exfoliation of silicene [241] and germanene [242] has not yet been demonstrated for LPE; TMDs are characterized by a relatively low value of the mobility of charge carriers [7]; black phosphorus suffers from rapid oxidation in environmental conditions [243]; while bismuth chalcogenides have poor fracture resistance [244]. Furthermore, MLG does not show a band gap [3], which is indispensable for obtaining a high ON/OFF ratio in nano-optoelectronic devices. A suitable candidate for (opto)electronics is represented by InSe. The β polymorph of indium selenide (β -InSe) has recently been widely studied thanks to its interesting fundamental properties [53], such as a low-electron effective mass ($m^* = 0.143\ m_0$) [245] and a bandgap interval from 1.26 eV for the bulk to 2.11 eV for the monolayer at room temperature (RT) [246], [247]. As the thickness of the crystal increases (> 6 layers - ≈ 5 nm, each layer has a thickness of 0.84 nm), its bandgap shows an indirect-to-direct crossover [70], [78], [248].

10.1 Design

The optical microscope images of the device are shown in Figure 43. The electrodes of photodetector have been designed with an interdigitated structure allowing to achieve a low electrical resistivity, by reducing the gap between electrodes L and increasing the total width of the conduction channel W, in a more compact format compared to linear electrodes, by using a parallel array of finger electrodes.

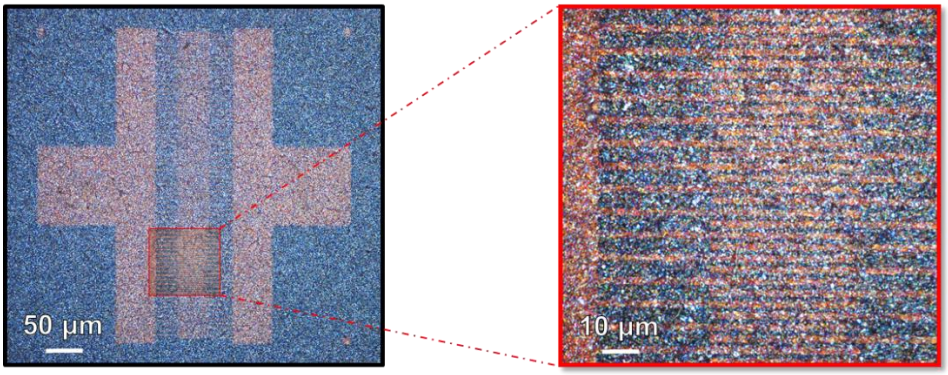

Figure 43 - Optical microscope image of the complete photodetector and magnified detail of the conducting channel region [225].

Additionally, the reduction of L leads to a faster response of the photodetector [249] by reducing the transit time of the carriers. The electrodes have been made up of 65 interdigitated fingers with an overlap of 40 µm and a gap L = 1 µm. The resulting channel width W = 5160 µm, provides an active area of W·L = 5160 μm^2 for photodetection.

10.2 Fabrication

In Figure 44 is shown a sketch of the spray coated β-InSe photodetector.

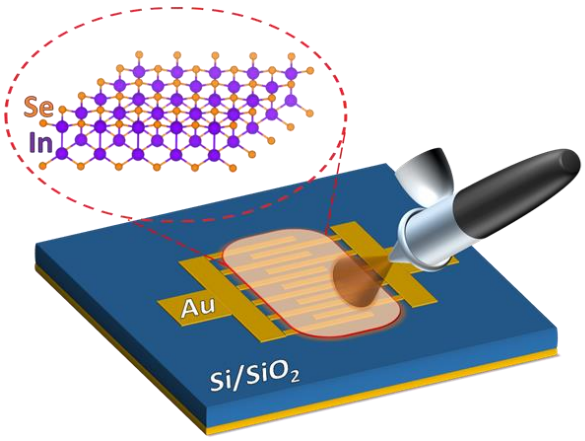

Figure 44 - Schematic illustration of the β-InSe photodetector [225].

The interdigitated gold electrode array has been implemented using e-beam lithography and lift-off (Microfabrication processes at page 59) on highly p-doped (boron) silicon (100) with 100 nm thermal oxide on the surface. During the same lithographic process, an array of 9 Au electrode has been

deposited by e-beam evaporation (Microfabrication processes at page 59) on the same substrate. In this way, it has been exploited the large area deposition capability of the spray coating process (Spray coating at page 56). A volume of ~ 30 ml of the β-InSe ink in IPA (InSe-based inks for photodetector devices at page 70) has been deposited by spray-coating onto the patterned substrate, which has been heated to 60°C to favour film drying during the deposition process. The coated sample has been placed under vacuum overnight at room temperature and then annealed at 200 °C for 30 min in argon atmosphere to stabilize the deposited film and remove residues of adsorbed solvent and moisture.

10.3 Morphological characterization

The film measured by profilometry is 515 ± 107 nm thick (Figure 45).

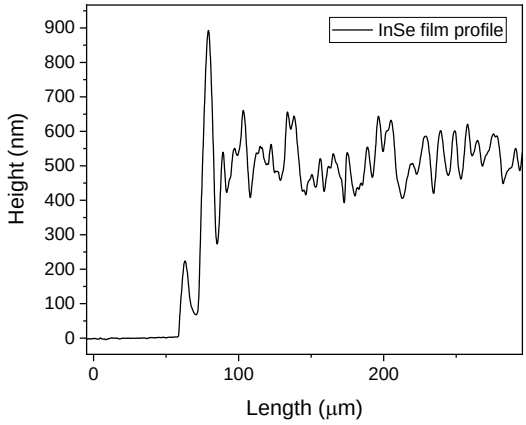

Figure 45 - Thickness profile of the InSe film measured near the active region of the photodetector. The measurement starts from a region where the substrate was exposed by scratching the film with a soft tip, in order to measure the thickness of the film [225].

Figure 46a shows the top-view scanning electron microscopy (SEM) image of the β-InSe film deposited on the electrodes, presenting a percolating network of flakes of lateral size < 500 nm. Energy-dispersive X-ray (EDX) spectroscopy (Figure 46b) was performed during SEM imaging, confirming the presence of β-InSe flakes in the film. From the EDX analysis on the device, it has been determined a ratio of 1:0.87 between In and Se. The elemental composition, within the experimental uncertainty of EDX, indicates the presence of selenium vacancies in the semiconductor film [224]. The signal from oxygen can be explained mostly by the SiO_2 layer on the surface of the substrate, although a superficial oxidation of the β-InSe flakes is also possible due to the processing in air.

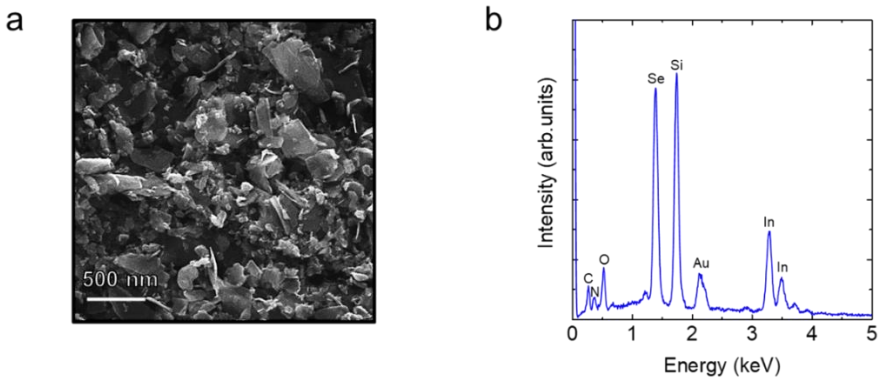

Figure 46 - a) HR SEM image of the β-InSe film in the conducting channel region of the device. b) EDX spectrum acquired from the active area of the photodetector. It is possible to observe In and Se signals, as well as Au from the electrodes, Si signal from the substrate, O signal due to both the SiO_2 and the partial oxidation of the InSe film [225].

10.4 Electrical characterization

In order to test the performance of the β-InSe photodetector, FoMs introduced in Photodetectors at page 49 have been calculated first in dark and then in light condition. Characteristic curves of the β-InSe photodetector have been measured at room temperature and under vacuum to avoid the influence of moisture and atmospheric gases. The doped silicon substrate has been electrically contacted to apply a gate bias V_G. In order to reveal the photodetection behaviour of the device, the electrical characteristics have been measured under the exposure to light of different wavelength and intensity.

10.4.1 Dark Current-Voltage Characteristics

The measure of drain–source current (I_D) vs the drain voltage (V_D) is shown in Figure 47a. It is possible to see that I_D varies with both drain (V_D) and gate (V_G) voltages (V_G ranging from -40 to 40 V). The I_D vs V_D vs V_G curve displays a gate-tuneable behaviour, indicating that the electrical characteristics of β-InSe device can be effectively controlled by electrostatic doping. For $0 < V_D < 0.5$ V it is found a quasi-linear regime (slope of the curve r = 1.2 - Figure 47b). This can be related to the presence of ohmic contacts between the gold electrode and β-InSe. At larger bias with $0.5 < V_D < 2$ V, a quadratic dependence of the drain current is observed, which can be explained by a space-charge limited current (SCLC) regime [250].

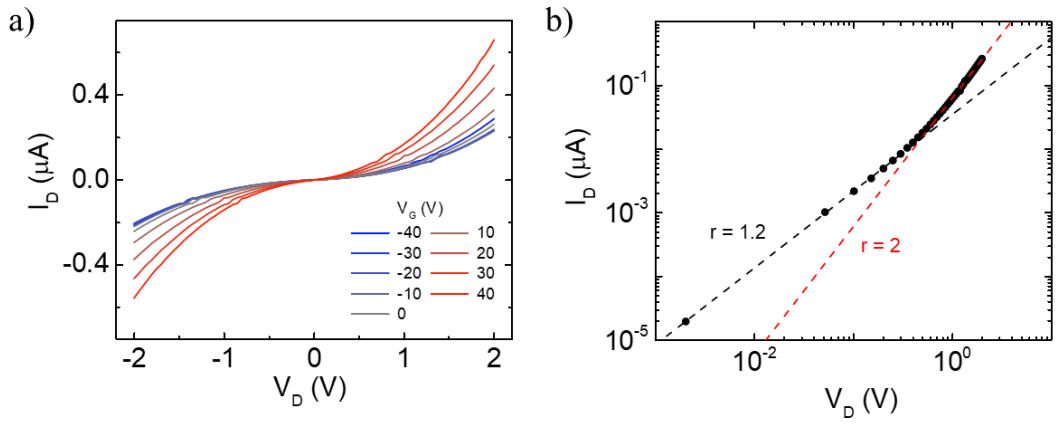

Figure 47 - a) Dark Source–drain current (I_D) versus source-drain voltage (V_D), at bottom-gate voltages between -40 and 40 V. b) log-log plot of I_D versus V_D (V_G = 0 V) is depicted, showing the transition from ohmic to space charge limited conduction [225].

SCLC becomes dominant when the injected electron concentration exceeds that of the thermally generated one. Charge-carrier traps within the semiconducting film, located for example in the partially oxidized surface of the flakes, are effective in immobilising most of the injected electrons [251], [252]. For shallow traps located at an energy E_t below the conduction band edge, the SCLC current density is given by a quadratic relation with respect to the voltage ($I_D \propto V_D^2$) [250]. The I_D–V_G transfer curve in Figure 48 has been measured at a drain bias voltage of 2 V.

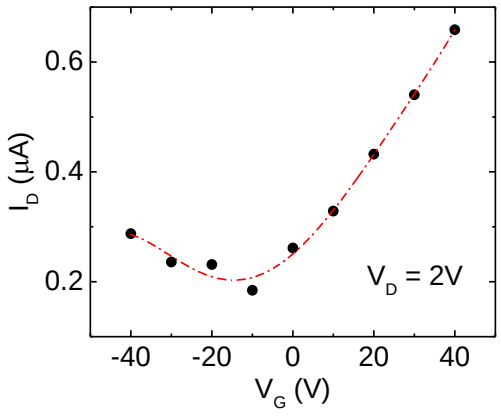

Figure 48 - Source–drain current (I_D) versus gate voltage (V_G) curve at V_D = 2V [225].

It shows an ambipolar behaviour with a minimum I_D current at $V_G \approx$ -10 V. In addition, the transistor presents a distinct asymmetry in electron and hole conduction being n-doped at V_G = 0 V. For this reason, no off-state condition can be measured. From the linear regions of the I_D-V_G curve it is possible to estimate the average mobility of the film resulting in $3 \cdot 10^{-5}$ cm^2 V^{-1}s^{-1} for the electrons

and $1 \cdot 10^{-5}$ cm^2 $V^{-1}s^{-1}$ for the holes. This phenomenon could be explained by the presence of the defect states in the gap of β-InSe.

10.4.2 Characterization under light

The dark photocurrent has been measured as a reference for measuring the photoresponsivity (R_{ph} – defined in Photoresponsivity (R) at page 50). In fact, R_{ph} is proportional to the photocurrent (I_{ph}), defined as the difference between the current measured (at V_D = 2 V, V_G = 0 V) under light and in the dark. Light intensities have been measured between 0.5 and 7.5 mW cm^{-2}. Figure 49a reports the photocurrent as a function of the light power on the device, using three different LEDs with emission peaks at 455, 530 and 625 nm (FWHM = 17, 42, 20 nm, respectively).

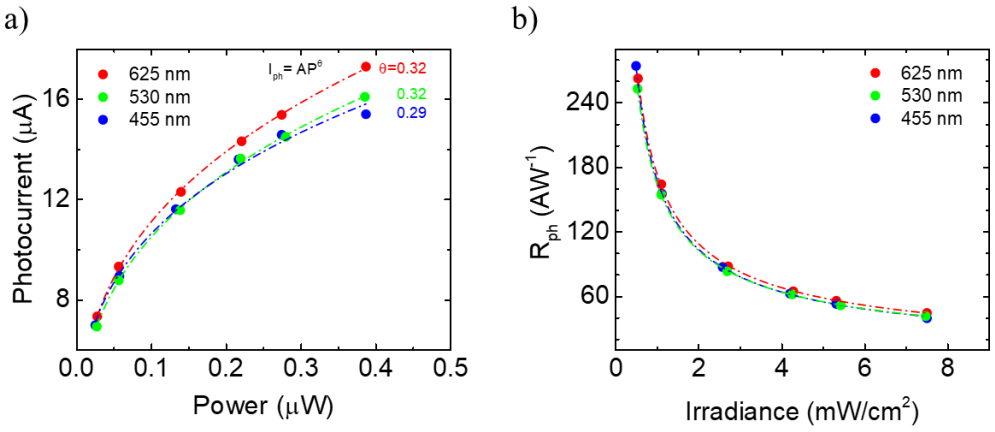

Figure 49 - a) Photocurrent response for varying incident light power on the active area of the device measured at three different wavelengths. The dashed lines represent a power-law fit to the data. b) The photoresponsivity R_{ph} versus the irradiance I_r [225].

The dependence on light power is sublinear, therefore, R_{ph} is decreasing as the power increases. The maximum measured responsivity at 455 nm is ~ 274 AW^{-1}, at ~ 0.53 mW cm^{-2} irradiance. The device maintained its functionality even in ambient conditions and after 1 year (Figure 52). To assess the minimum detectable light intensity, we calculated the detectivity the Specific Detectivity (D*) (shown at page 52) ~ 5.49×10^{12} Jones. We obtained a maximum value (corresponding to the maximum responsivity) of Noise Equivalent Power (NEP) (shown at page 51) ~ 1.31×10^{-15} W $Hz^{-0.5}$. These FoM values compare favourably with those reported in literature [172], [253]–[255]. The responsivity is at least one order of magnitude higher than those of photodetectors based on solution processed 2D crystals, and InSe in particular [256]. There are several factors that can cause the increased

responsivity of our device. The short length of the channel (L) increases the photoresponsivity of the device, since R_{ph} is proportional to L^{-2} [40]. Moreover, the highly-uniform coverage of β-InSe on the Si/SiO_2 substrate over the active area could promote the extraction efficiency of the photogenerated carriers as already suggested in literature for perovskite- [257], thin film CdTe- [258] and graphene-based devices [259]. The spectral response of the device is shown in Figure 50 from the visible to the NIR range, measured with mechanically-chopped light at 23 Hz at bias voltages V_D = 2V and gate voltage V_G = 0V.

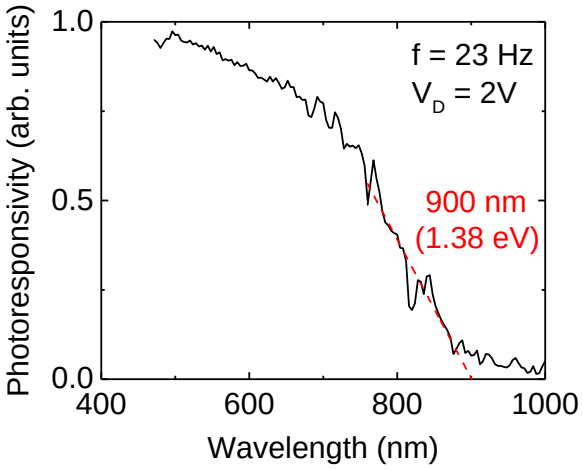

Figure 50 - Spectral responsivity of β-InSe photodetector. The dashed line is a linear fit of the tail of the spectrum; the onset of the photoresponse at ~900 nm (1.38 eV) is highlighted [225].

The responsivity is high at short wavelength (~ 400 nm) and decreases towards longer wavelength with a pronounced drop at ~ 800 nm. If the wavelength dependence is dominated by the absorption coefficient, it is possible to estimate the bandgap from the intercept with the wavelength axis of a linear fit of the spectral responsivity in the region near the photoresponse threshold wavelength (Figure 50). The resulting value of ≈ 900 ± 65 nm corresponds to a bandgap of ≈ 1.4 ± 0.1 eV, which is in the range between the values reported for single layer and bulk β-InSe (2.11 - 1.26 eV respectively), confirming that the film is composed by few layer flakes. In Figure 51a and Figure 51b it has been shown the time response of the device, obtained by measuring the current during pulsed light excitation. Excellent long-term stability is observed with a fast switching and reproducible transition from "ON" to "OFF" conditions. The measured rise (fall) time (Figure 51b), defined as the time to pass from 10% (90%) to 90% (10%) of the maximum photocurrent, is τ_R = 15.1 ms (τ_F = 63.7 ms), while other photodetectors made with films of LPE flakes of β-InSe reported response times of the order of seconds [256], [260]. In Figure 53, it has been reported the dependence of the photocurrent amplitude on the modulation frequency *f*.

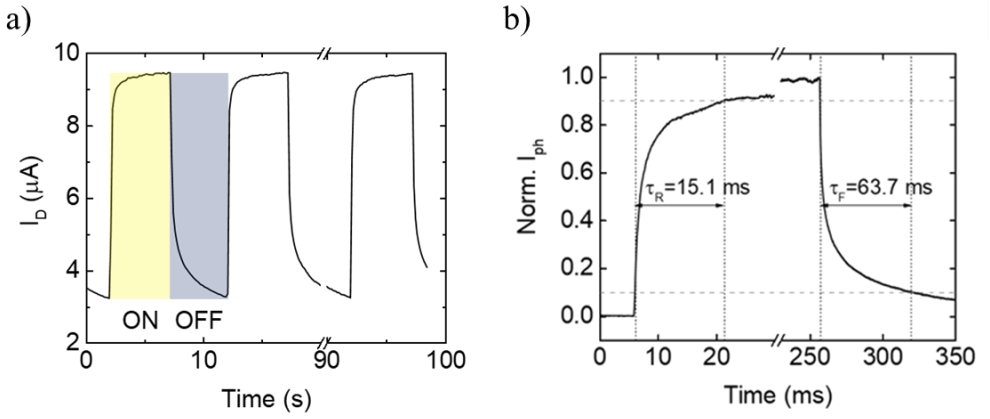

Figure 51 - a) The response to 0.1 Hz pulsed light (530 nm) b) Detail of photocurrent rise and decay during pulsed (2 Hz) 625 nm light excitation [225].

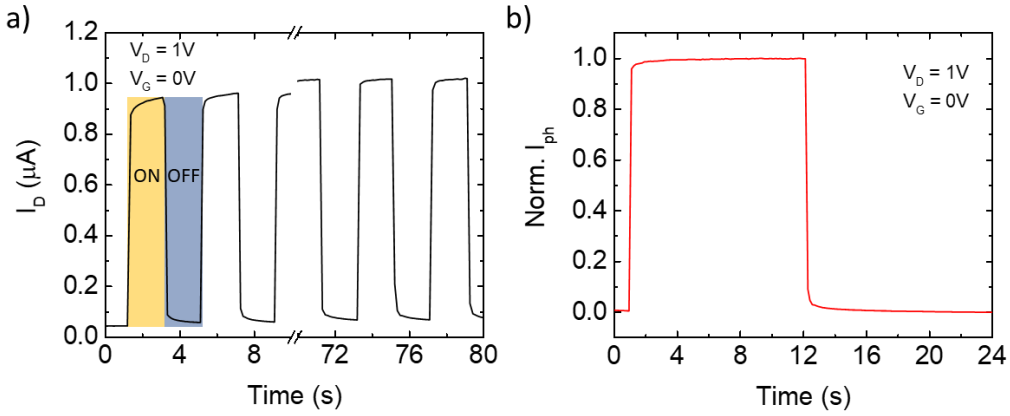

Figure 52 – a) Photocurrent measurement performed in air under white LED light (100 mW cm^{-2}), 1 year after the characterization in vacuum at 0.5Hz and b) at 0.2Hz (normalized).

The amplitude decreases with the increase of the frequency, and the signal is measurable up to 1 kHz; the functional dependence of the frequency does not follow a simple low-pass behaviour but exhibits richer features with complex power-law trends that follow a $f^{-0.5}$ and $f^{-0.2}$ dependence at low and high modulation frequency respectively, as shown by dashed lines in the panel. Such behaviour could indicate an energy distribution of trap states in the material.

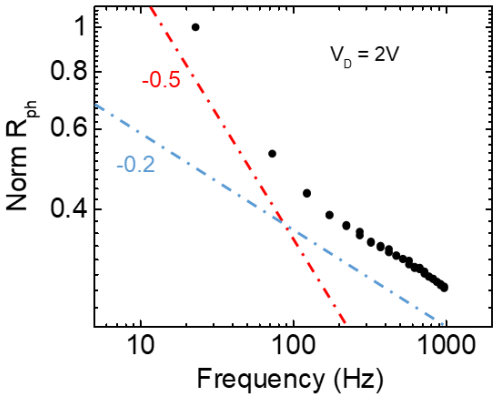

Figure 53 - Responsivity versus light chopping frequency under illumination at 625 nm. Dashed lines indicate the power laws $f^{-0.5}$ and $f^{-0.2}$ [225].

The time decay of photocurrent in Figure 51b can be investigated more in detail to understand the mechanism of charge recombination in our device. In general, the time derivative of the photoexcited charge density *n*, after turning off the light, is a function of *n* itself:

$$\frac{dn}{dt} = g(n) \qquad \text{Eq. 28}$$

If the photocurrent is proportional to *n*, the function g can be determined from the time dependence of I_{ph} during the decay measurement. In Figure 54 we plot the photocurrent derivative ($dI_{ph}(t)/dt$) versus I_{ph} after light was switched off.

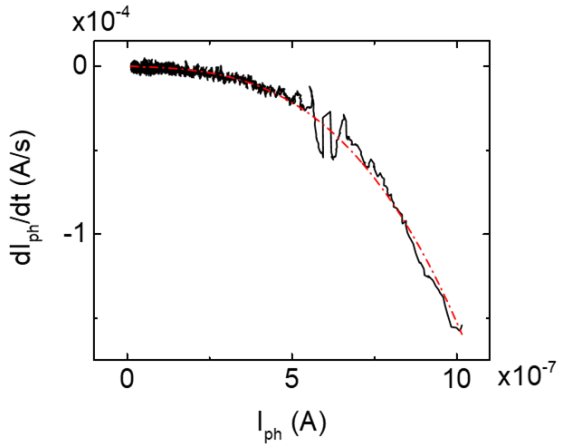

Figure 54 - Plot of the time derivative of the photocurrent versus the photocurrent after switching off the light [225].

A third-order polynomial yields an excellent fit to the data (dashed line in Figure 54), suggesting that the differential equation controlling generation-recombination under light is:

$$\frac{dn}{dt} = F - R_r n^3 \qquad \text{Eq. 29}$$

Here, F is the generation rate due to incoming light, and R_r is a constant controlling the recombination rate. This dependence is further confirmed by the photocurrent vs light power dependence (Figure 49a). If steady-state is reached for these measurements (dn/dt=0), by solving Eq. 29 it has been found a dependence as $I_{ph} \propto n \propto F^{\vartheta}$, with ϑ = 1/3. In fact, the fits shown in Figure 49a yield ϑ_{625} = 0.324 ± 0.003, ϑ_{530} = 0.318 ± 0.004, ϑ_{455} = 0.293 ± 0.013, confirming this prediction. The observed power-law dependence is related to the dynamics of the traps and recombination centres that enable the photoconduction in nanostructured materials. A nonlinear dependence of the photocurrent on the light intensity can arise from the distribution of traps and recombination centres within the band gap[91,92] and the saturation of these states under strong light excitation [256], [261]–[264], or even from the presence of a space charge region [265], [266]. The particular case of the third-order equation, as suggested in Ref.[267], can be related to the recombination assisted by doubly charged Se vacancies, which have been observed in our sample by EDX analysis and by previous studies on β-InSe [224], [251], [252]. We remark that doubly charged vacancies in CdS have been related to more complex processes involving not only charge excitation, but also charge-lattice coupling that lead to a thermally activated recombination behaviour [267], suggesting that further studies of these properties can lead to interesting physics of the material.

11 GRAPHENE-BASED SUPERCAPACITORS

The ever-increasing demand of multi-functional systems has drawn the attention towards planar micro-supercapacitors (MSCs) [119], [268]–[270], which can deliver all the benefits of supercapacitors in a much smaller, lighter device [119], [271], [272].

11.1 Design and fabrication

The screen printer technique (Screen Printing at page 58) was used to fabricate the interdigitated electrodes. The screen-printing setup consisted in a 58 × 48 cm 55T (threads per cm) aluminum frame, using polyester as a mesh material. The 55T aluminum frame had a single mesh opening of 0.1 mm, yielding a maximum resolution of 0.3 mm. The screen-printed MSCs configuration consisted of six fingers (1 mm thick) forming the interdigitated structure with an interspace between fingers of 600 µm, which is a sufficient distance in order to avoid short-circuits, providing an active area of 1 cm^2 (Figure 55).

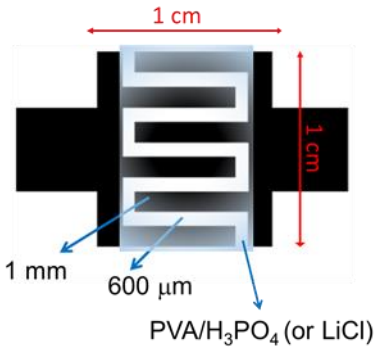

Figure 55 - Layout adopted as interdigitated electrodes for screen printing MSCs on plastic (PET) substrates [119].

Two different active materials have been used in order to product and investigate the performance of MSCs, a WJM-graphene-based paste and a WJM-graphene:CNTs-based paste. The printing strategy involved multiple printing passes until proper mass loading of active material was reached (1 mg for WJM-graphene and 1.5 mg for WJM-graphene:SWCNTs). The substrate was 1 µm-thick polyethylene terephthalate (PET) foil (Sigma Aldrich). Depending on the printed paste, the MSCs named WJM-graphene and WJM-graphene:SWCNTs were obtained. Electrodes of 10 µm-thick pyrolitic graphite (PG) paper (PGS, Panasonic) with the same interdigitated shape of screen printed electrodes were also evaluated as current collectors for WJM-graphene:SWCNTs-based MSCs. The

corresponding MSCs are herein named PG/WJM-graphene:SWCNTs. After printing the active materials, the structures were dried at 80 °C under vacuum for 1 h to remove solvents. The MSCs were then completed by coating the printed electrodes with a H_3PO_4-doped PVA-based electrolyte and dried in ambient conditions overnight. Therefore, washability test was also carried out on PG/WJM-graphene:SWCNTs. For washability test, the device was properly encapsulated with crosslinked ethylene vinyl acetate (EVA), *via* hot sealing process at 140 °C. The process in shown in Figure 56.

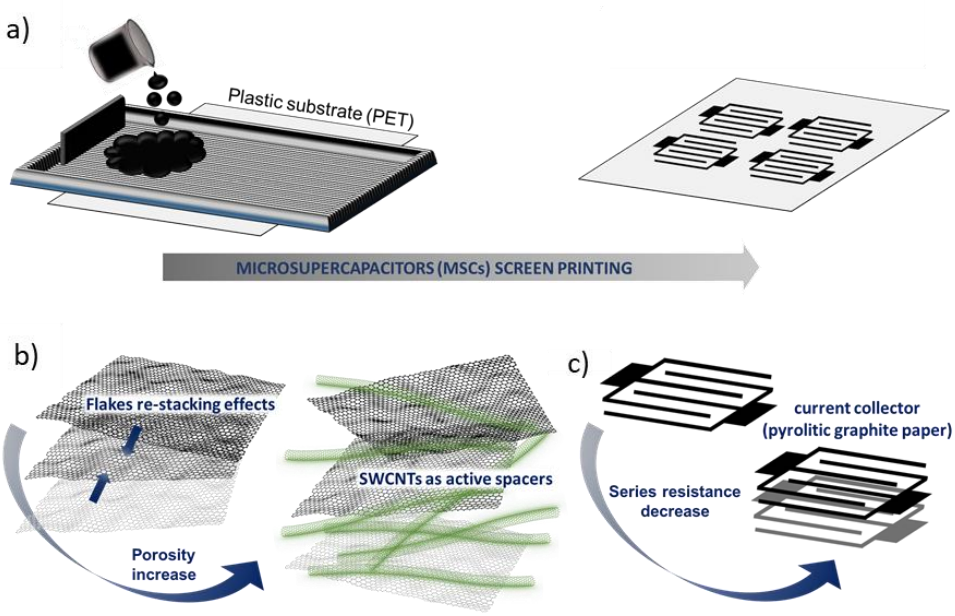

Figure 56 – a) Screen printing of MSCs onto plastic substrate (polyethylene terephthalate –PET–). (b) Addition of CNTs as active spacers for avoiding flakes re-stacking effects. (c) Utilization of pyrolytic graphite (PG) paper in order to decrease the series resistance of MSCs for high-power requirements [119].

11.2 Morphological characterization

Figure 57 shows representative top-view and cross-sectional SEM images of a PG/WJM-graphene:SWCNTs. In particular, Figure 57c,d show the layered structure of the electrode, as given by a ~27 ± 4 μm-thick film of WJM-graphene:SWCNTs onto PG paper. The morphology of the WJM-graphene:SWCNTs film consisted of a mesoporous network of WJM-graphene with dispersed SWCNTs acting as linker between the same flakes.

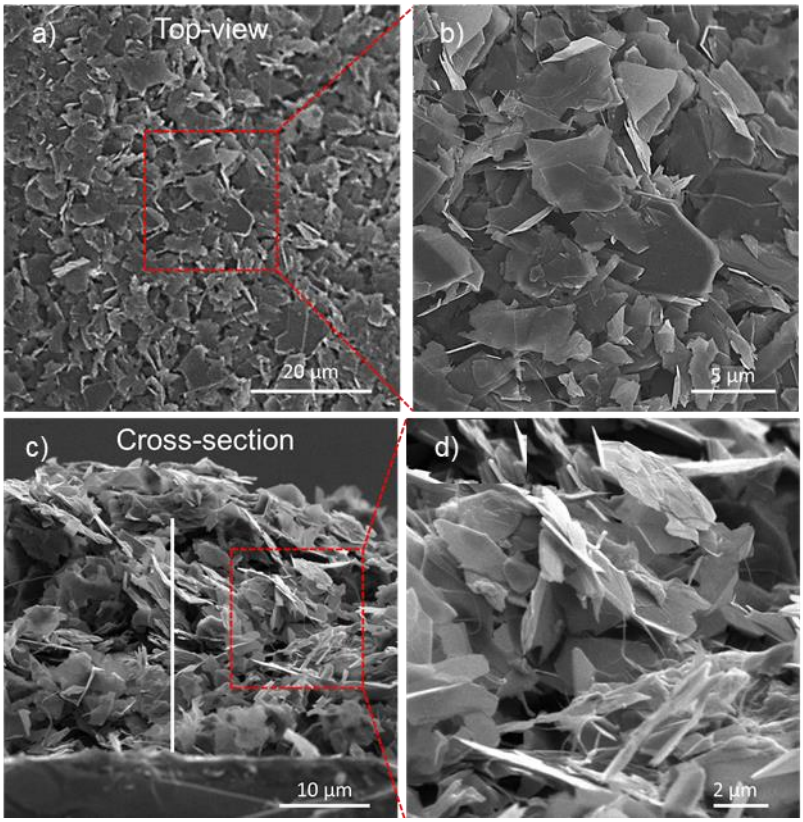

Figure 57 - a) Top-view SEM image, and b) the corresponding enlargement of the region delineated by red dashed lines, of a representative PG/WJM-graphene:SWCNTs. c) Top-view SEM image, and d) the corresponding enlargement of the region delineated by red dashed lines, of a representative PG/WJM-graphene:SWCNTs [119].

Figure 58 shows a digital photograph of a bended MSCs, evidencing the mechanical flexibility of the device.

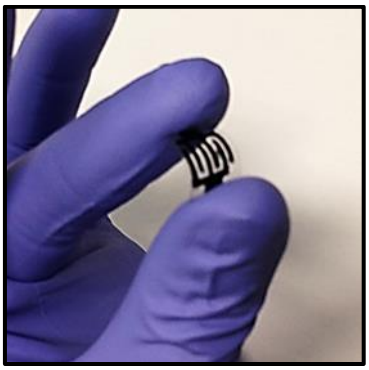

Figure 58 - Digital photograph of a screen-printed MSC. The electrode was manually bended in order to show its mechanical flexibility [119].

11.3 Electrochemical measurements

The electrochemical performances of the screen printed MSCs were evaluated by cyclic voltammetry (CV) and galvanostatic charge/discharge (CD) measurements.

11.3.1 Cyclic Voltammetry

Figure 59 shows the comparison between the CV curve of the different MSCs using PVA/H_3PO_4 as hydrogel-polymer electrolyte.

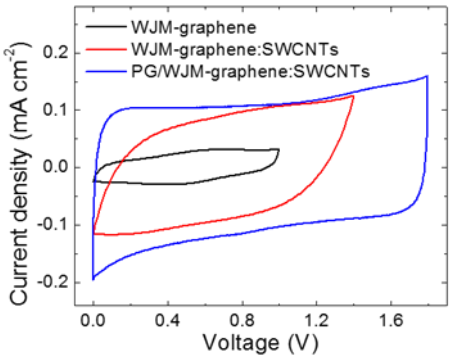

Figure 59 - Comparison between CV curves of WJM-graphene (black), WJM-graphene:SWCNTs (red) and PG/WJM-graphene:SWCNTs (blues) at a voltage scan rate of 100 mV s^{-1} [119].

The nearly-rectangular CV shapes and the absence of redox peaks indicate that the electrodes show double-layer capacitive behavior [273], [274] in the corresponding voltage range. The latter were properly selected in order to avoid parasitic chemical reactions (Figure 60). In fact, this peculiar shape is related to pseudo-capacity effects due to marginal presence of redox activities of the electrolyte [275].

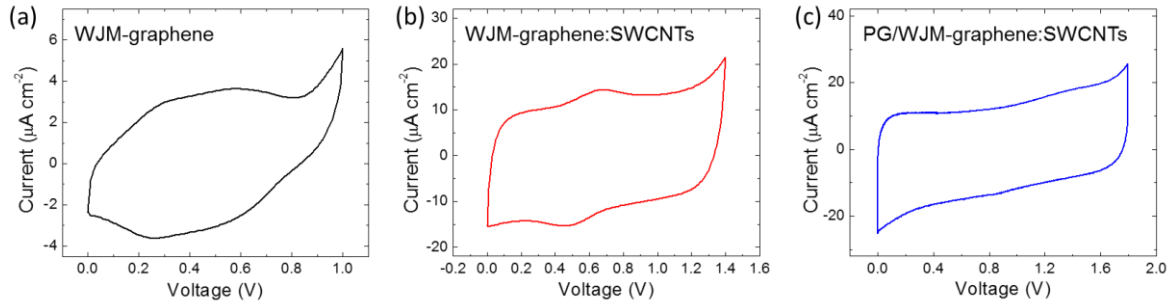

Figure 60 - Cyclic voltammetry curve of a) WJM-graphene, b) WJM-graphene:SWCNTs and c) PG/WJM-graphene:SWCNTs at a voltage scan rate of 10 mV s^{-1} [119].

The addition of SWCNTs into WJM-graphene remarkably increase the area of the voltammograms, thus meaning the capacitance increased with respect to that of WJM-graphene. This positive effect was attributed to the key-role of SWCNTs for eliminating the re-stacking of WJM-graphene flakes during film screen-printing process, which allow the specific surface area of the flakes to be accessible to the ions for the electrochemical double-layer formation [276]. In addition, the use of GP paper-based current collectors eliminated the biconvex shape featured by WJM-graphene and WJM-graphene:SWCNTs. Four-point probe measurements (Figure 61) clarified that the lens-shaped voltammograms of MSCs without current collectors were mainly attributed to the higher resistivity of mesoporous WJM-graphene and WJM-graphene:SWCNTs films (~ 0.8 Ω cm and ~ 0.1 Ω cm, respectively) with respect to that of GP paper.

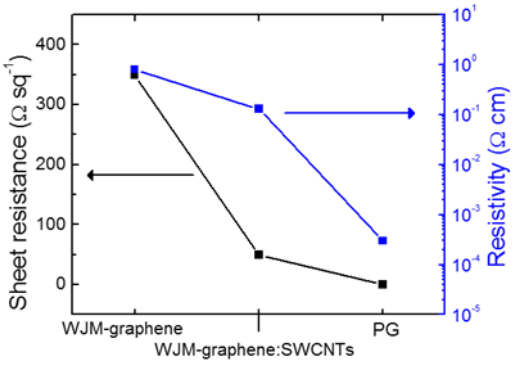

Figure 61 - Sheet resistance (left y-axis, black) and resistance (right y-axis, blue) of screen printed WJM-graphene and WJM-graphene:SWCNTs films (thickness of 27 ± 4 and 23 ± 3 μm, respectively, active material mass loading of 2 mg cm-2), as well as of GP paper (10 μm-thick) [119].

In fact, unpatterned WJM-graphene and WJM-graphene:SWCNTs films with mass loading of 2 mg cm^{-2} (comparable to that used for screen-printed MSCs) displayed sheet resistance as high as 350 and 50 Ω sq^{-1}, while GP paper showed sheet resistance of 0.042 Ω sq^{-1}. These results indicated that for high-power application of graphene-based MSCs, current collector are needed to transport the charge along the plane of the substrate, in agreement with previous literature reports [119], [277]–[280]. Lastly, it is noteworthy that the use of GP-based current collectors also enabled the operating voltage window to be extended up to 1.8 V.It has been speculated that efficient charge extraction hindered the formation in the active material of strong localized filed which could promote parasitic faradaic reaction.

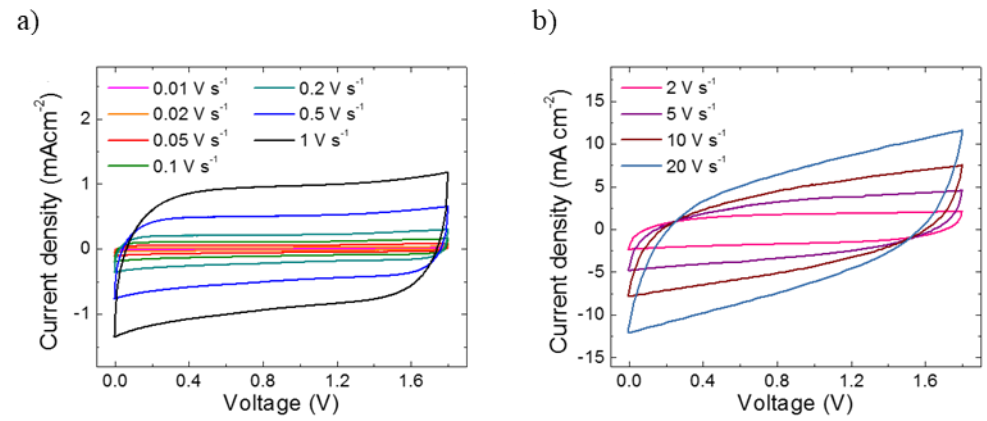

Figure 62 – a) Cyclic voltammetry curves of GP/WJM-graphene:SWCNTs for 0.01 V s^{-1} to 1 V s^{-1}, b) Cyclic voltammetry curves of GP/WJM-graphene:SWCNTs for 2 V s^{-1} to 20 V s^{-1} for panel [119].

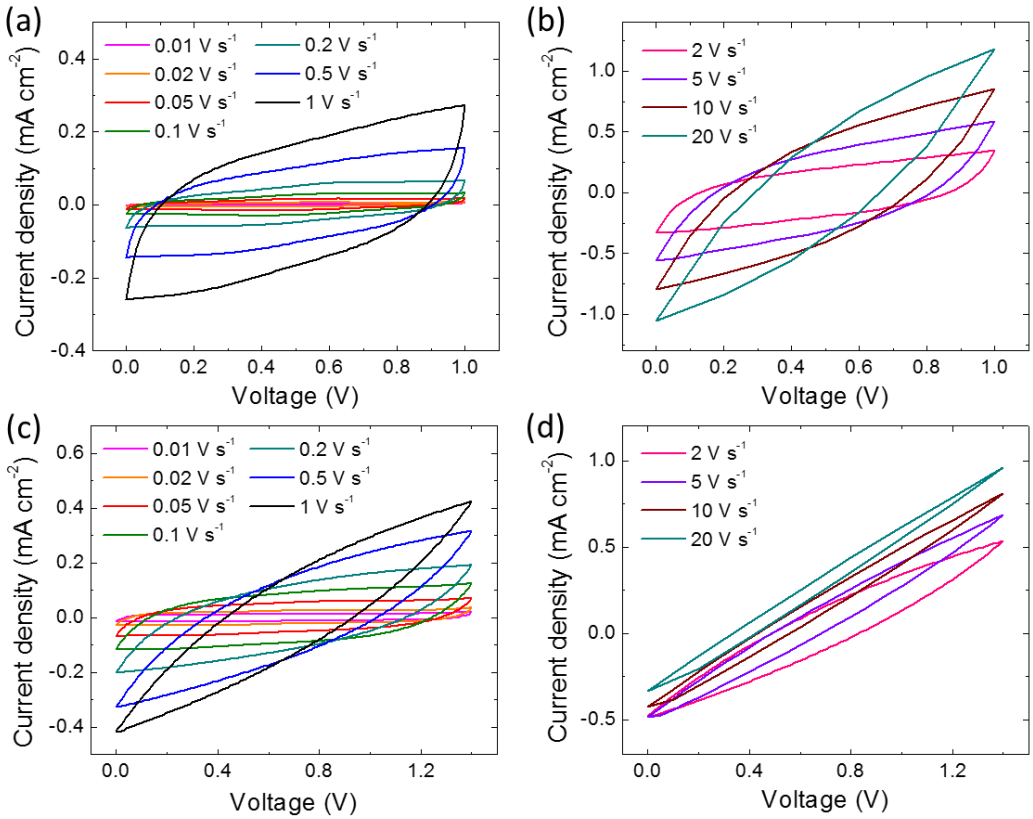

Figure 63 - Cyclic voltammetry characterization of WJM-graphene and WJM-graphene:SWCNTs. (a,b) Cyclic voltammetry curves of WJM-graphene at different voltage scan rate (from 0.01 V s-1 to 1 V s-1 for panel a, from 2 V s-1 to 20 V s-1 for panel b). (c,d) Cyclic vo voltammetry curves of WJM-graphene:SWCNTs at different voltage scan rate (from 0.01 V s^{-1} to 1 V s^{-1} for panel c, from 2 V s^{-1} to 20 V s^{-1} for panel d) [119].

Figure 62 reports the CV measurements for GP/WJM-graphene:SWCNTs at voltage scan rate ranging from 0.01 to 20 V s^{-1}. The devices exhibited a linear dependence of the maximum current density

even at a high voltage scan rate of 20 V s^{-1} (Figure 62b), indicating that they retained excellent capacitance also for high instantaneous power. Notably, such rate performance were achieved for MSCs with μm-thick active material, which are three order of magnitude higher than those reported for high-power graphene-based MSCs [119], [277]–[280]. The CV curves at different scan rate obtained for WJM-graphene and WJM-graphene:SWCNTs, thus in absence of current collector, are reported in Figure 63. In order to achieve valuable MSCs using solely WJM–graphene, active material mass loading was 50% higher that of WJM-graphene:SWCNTs in order to avoid excessive series resistance, which were cause of device failures with increasing the voltage scan rate. Clearly, this effects were reduced by using SWCNTs, which randomly bridge the graphene flakes to form a more electrically conductive network [119], [281]–[286], as also evidenced by SEM analysis (Figure 57).

11.3.2 Galvanostatic charge/discharge

Galvanostatic CD curves were recorded for practical capacitance evaluation (Figure 64). Figure 64a displays the comrparison between the CD curve obtained for the different MSCs at current density of 0.125 mA cm^{-2}. The MSCs showed nearly triangular shapes in the selected voltage windows. This confirms the double-layer capacitive behaviour of the devices, which is consistent with the results evidenced by CV measurements. Figure 64b shows the CD curve of PG/WJM-graphene:SWCNTs obtained at various current densities (from 0.0125 to 25 mA cm^{-2}). The CD curves for WJM-graphene and WJM-graphene:SWCNTs obtained at various current densities are shown in Figure 65. From CD curve data, the C_{areal} of the MSCs can be calculated by the equation $C_{areal} = (|i|t_d)/(A_{geom}\Delta V)$ [287], where |i| is the module of the applied current (i), t_d is the discharge time, A_{geom} is the geometrical area of the devices (calculated based on the active projected surface area, including the area of interdigitated fingers and the interspaces between them) and ΔV is the voltage window of the measurement. As shown in Figure 64c, C_{areal} values increased with the addition of SWCNTs to the WJM-graphene as active material. More in detail, C_{areal} of 1.324 mF cm^{-2} (5.296 mF cm^{-2} in electrode) was obtained for WJM-graphene:SWCNTs at current densitiy of 0.0125 mA cm^{-2}, which was 3.43-fold higher than that of WJM-graphene (0.385 mF cm^{-2}, 1.54 mF cm^{-2} in electrode). By adopting PG as current collectors, high capacitance was observed even when operated at high charge/discharge rates, up to 25 mA cm^{-2}. In particular, PG/WJM-graphene:SWCNTs showed a 2.88-fold increase of C_{areal} (equal to 1.033 mF cm^{-2}) with respect to that obtained for WJM-graphene:SWCNTs (0.359 mF cm^{-2}). Interestingly, PG/WJM-graphene:SWCNTs exhibited remarkable C_{areal} (> 0.140 mF cm^{-2}) even when operated at high charge/discharge current density (up to 25 mA cm^{-2}).

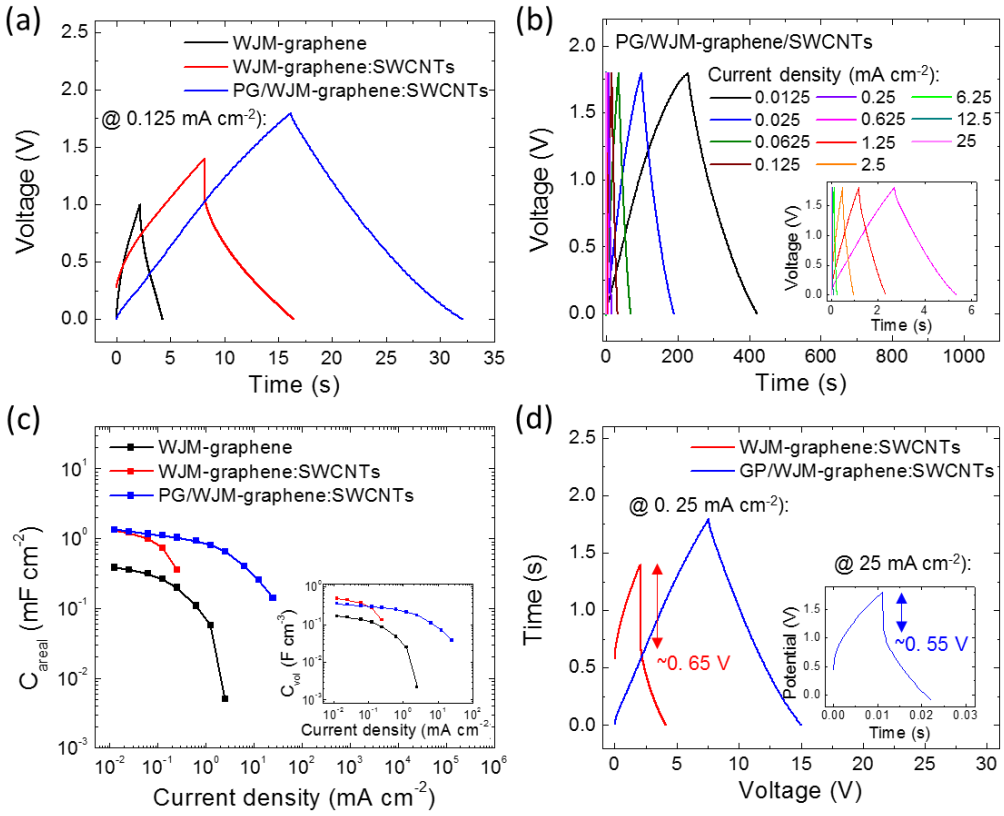

Figure 64 - Capacitance evaluation of screen-printed MSCs. (a) Comparison between galvanostatic CD curves of WJM-graphene (black), WJM-graphene:SWCNTs (red) and PG/WJM-graphene:SWCNTs (blue) at a current density of 0.125 mA cm-2. (b) Galvanostatic CD cu rves of GP/WJM-graphene:SWCNTs at different current density (from 0.0125 mA cm^{-2} to 25 mA cm^{-2}. (c) Value of the C_{areal} plotted as a function of the current density for WJM-graphene (black), WJM-graphene:SWCNTs (red) and PG/WJM-graphene:SWCNTs (blue). The inset shows the values of the C_{vol} plotted as a function of the current density different for the same MSCs. (d) Comparison of the galvanostatic CD curves WJM-graphene:SWCNTs (red) and PG/WJM-graphene:SWCNTs (blue) at a current densities of 0.25 mA cm^{-2}. The inset panel shows the galvanostatic CD curve of the PG/WJM-graphene:SWCNTs at current density of 25 mA cm^{-2}. The voltage drop at half cycle, which was used for ESR estimation, is indicated for each curve [119].

The inset of Figure 64c shows the volumetric capacitances (Cvol), calculated by considering the whole volume of the interdigitated fingers (including GP-based current collectors when used) and the interspaces between them, for the tested MSCs at various current densities.

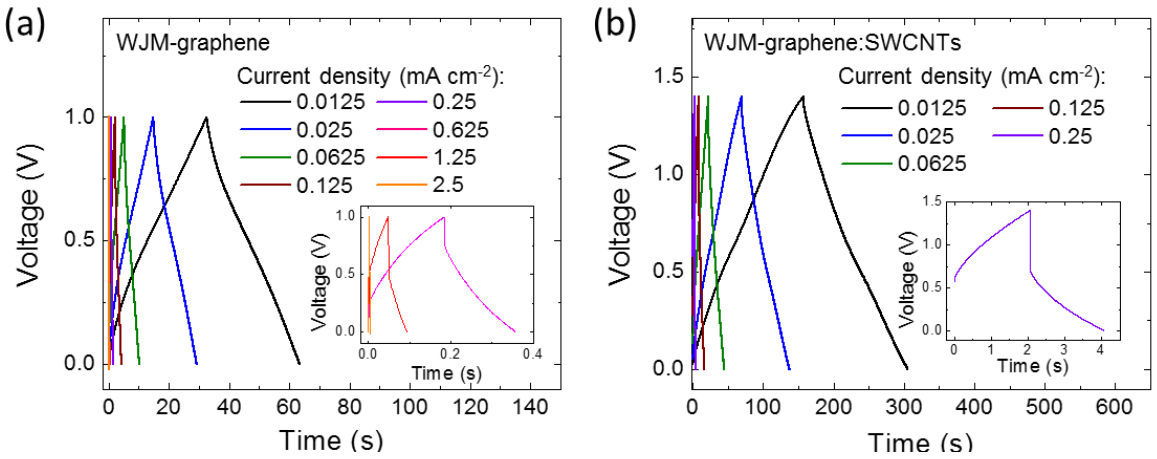

Figure 65 - Galvanostatic CD measurements for WJM-graphene and WJM-graphene:SWCNTs. (a) Galvanostatic CD curves of WJM-graphene at various current density (from 0.0125 mA cm-2 to 2.5 mA cm-2). The inset shows the temperal enlargement of the CD curve obt ained at current density of 0.625, 1.25 and 2.5 mA cm^{-2}. (b) Galvanostatic CD curves of WJM-graphene:SWCNTs at various current density (from 0.0125 mA cm^{-2} to 2.5 mA cm^{-2}). The inset shows the temperal enlargement of the CD curve obtained at current density of 0.625, 1.25 and 2.5 mA cm^{-2} [119].

At the lowest current density (0.0125 mA cm^{-2}), C_{vol} was 0.112 F cm^{-3} (0.448 F cm^{-3} in electrode) and 0.490 F cm^{-3} (1.961 F cm^{-3} in electrode) for WJM-graphene and WJM-graphene:SWCNTs, respectively. These values approached to the order magnitude of the C_{vol} values exhibited by state-of-the art ultrathin MSCs adopting tens nm-thick reduced graphene oxide as active materials (C_{areal} up to 17.9 F cm^{-3}) [277], [288]. At low current density (< 0.1 mA cm^{-2}), the use of PG as current collector decrease the C_{vol} of PG/WJM-graphene:SWCNTs with respect that of WJM-graphene:SWCNTs because of the increase of the overall thickness of the interdigitated electrodes, which also include that of GP paper (10 μm). However, the use of GP paper still allowed remarkably C_{vol} (up to 0.362 F cm^{-3} at current density of 0.0125 mA cm^{-2}) to be reached, especially at high charge/discharge current densities (> 0.25 mA cm^{-2}) where WJM-graphene:SWCNTs showed a resistive behavior. The capacitive losses observed with increasing the current density were ascribed to the potential drops in the equivalent series resistance (ESR) of the MSCs [119], [273], [274]. ESR can be calculated by the galvanostatic CD curves, using the equation ESR = $V_{drop}/|i|$, where V_{drop} is the voltage drop at half-cycle of the CD curve [119], [273], [274]. As shown in Figure 64d, in absence of GP paper as current collector, the in-plane electrical resistance of the interdigitated mainly contributed to the overall ESR, whose value (~ 3.2 kΩ) is orders of magnitude higher than that of GP/WJM-graphene:SWCNTs (~ 22 Ω). Therefore, depending on the final requirement in terms of volume and operating power, the use of GP paper as current collector can be assessed whether advantageous. It is worth noting that the so-obtained volumetric performance allowed state-of-the-arte MSC areal capacitance, which is the most relevant supercapacitor performance for wearable

application, to be reached by adopting higher mass loading (milligram-scale)/thickness (ten micrometer-scale) of active materials than those used in competing MSC technologies (ten μg-/ten nanometer-scale) [268]–[272]. Consequently, GP/WJM-graphene:SWCNTs allowed for a power density of 20.13 and 1.13 mW cm^{-2} at energy density of 0.064 and 0.361 μWh cm^{-2}.

11.3.3 Durability and mechanical properties

In order to prove the durability and the mechanical properties of the as-produced MSCs, galvanostatic CD cycling was carried out over 10000 cycles (Figure 66a) and different bending-type stresses with different radii of curvature (R) and bending angle (θ) (Figure 66b). As shown in Figure 66a, PG/WJM-graphene:SWCNTs exhibited excellent cycling stability. In fact, up to 98.0% of capacitance was maintained after 10000 cycles at a current density of 0.1875 mA cm^{-2}. Notably, the high Coulombic efficiency (ranging from 93% in the first cycles to more than 96% after stabilization) indicated that the double-layer formation is highly reversible, without the occurrence of parasitic faradaic reactions. Similar results were also obtained for WJM-graphene, as shown in the inset of Figure 66a. The high-durability of the devices was attributed to the in-plane interdigitated graphene-based structures which allow for a favorable ultrafast uptake of the flow of electrolyte ions into or removal from the graphene layers in a short diffusion pathway [277], [278]. Figure 66c shows the capacitance retention plots over bending with radius of curvature (R) of 1 cm for PG/WJM-graphene:SWCNTs. The inset panel of Figure 66c shown the same test with R equal to 2 cm. For R = 1 cm, the device retained more the 97% of the initial capacitance, with Coulombic efficiency more than 95%. For a less invasive R of 2 cm, a negligible capacitance loss (~1%) was observed with a Coulombic efficiency exceeding 95%. The devices were also tested at different bending angles ranging from 0° (unbent) to 90° and 180° (folded) /Figure 66d). After folding at both bending angle, the device exhibited a 6% increase of the capacitance, without significant variation of Coulombic efficiency.

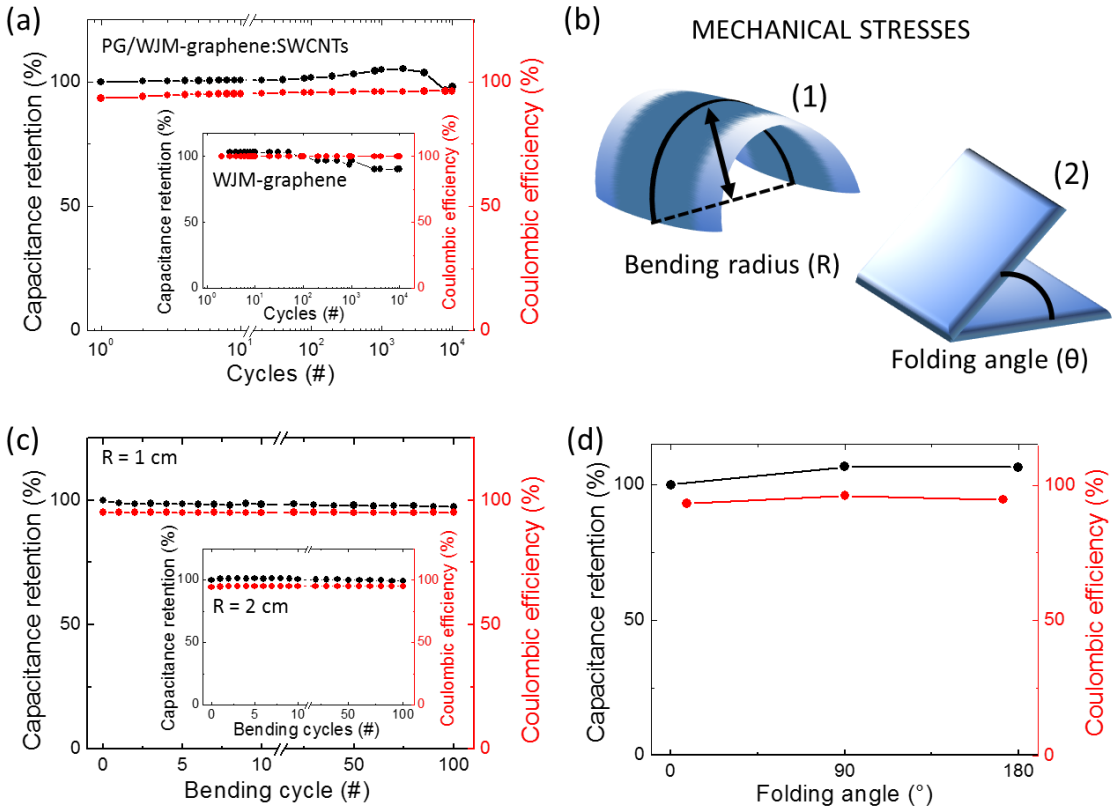

Figure 66 - Durability and mechanical flexibility of screen-printed MSCs. (a) Capacitance retention of PG/WJM-graphene:SWCNTs over 10000 CD cycles at current density of 0.125 mA cm-2. (b) Schematic illustration of the adopted mechanical stresses: (1) be nding and (2) folding. (c) Capacitance retention of PG/WJM-graphene:SWCNTs over 100 bending at bending radius (R) of 1 cm and 2 cm (inset panel) (black, left y-axis). The Coulombic efficiency is also plotted as a function of the bending cycles (red, right y-axis). (d) Capacitance retention of folded PG/WJM-graphene:SWCNTs at angle (θ) of 90° and 180° (black, left y-axis). The Coulombic efficiency is also plotted as a function of the folding angle (red, right y-axis) [119].

11.3.4 Washability test

For wearable application, waterproof property is also crucial [289] because wearable devices often face wet environment such as sweat and rain, as well laundry cycles [290], [291]. Therefore, washability test was also carried out on PG/WJM-graphene:SWCNTs. Before to undergo a washing cycle, the device was properly encapsulated with crosslinked ethylene vinyl acetate (EVA), which is an encapsulant material benchmark with both waterproof properties and stress-crack resistance (*i.e.*, mechanical flexibility) [292], [293], *via* hot sealing process at 140 °C. For the waterproof test, we measured the CV and CD curves after a washing cycle in home-laundry conditions. In order to simulate practical home-laundry conditions, the device was accommodated into microfleece garment (Figure 67a) and the washing cycle was carried out using both detergent and fabric softener at 60 °C, followed by centrifugation at 1200 rpm to remove water excess and fasten the laundry drying.

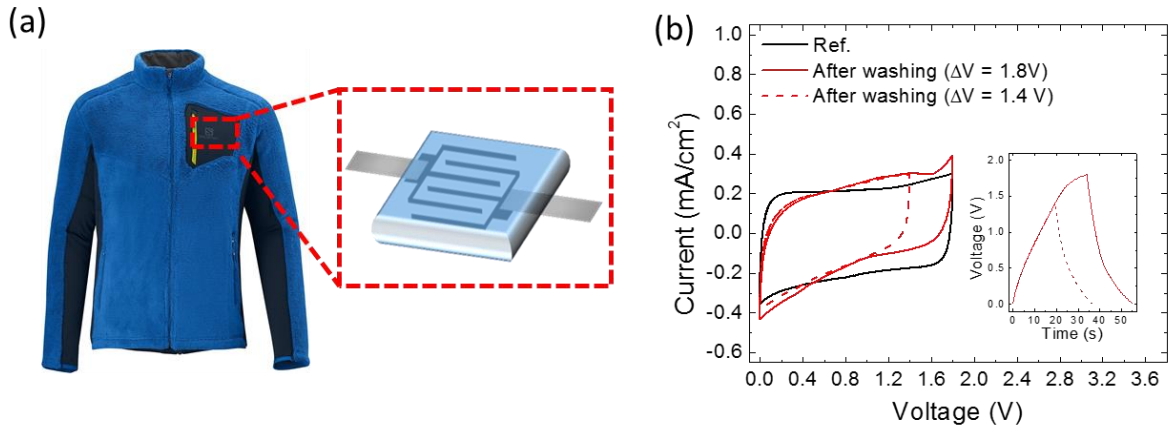

Figure 67 - Washability tests of EVA-sealed screen-printed MSCs. (a) Schematic illustration of the MSCs accommodation into microfleece garment simulating practical home-laundry conditions. (b) Electrochemical characterization (CV and CD measurements) of the MSCs after washing cycle using both detergent and fabric softener at 60 °C, followed by centrifugation at 1200 rpm [119].

As shown in Figure 67b, comparable current density was recorded by CV measurements. The occurrence of parasitic faradaic reaction in the voltage window of 1.8 V could be ascribed to the sealing process, which could partially alter the hydrogel-polymer electrolyte. Alternative low-temperature sealing methods are currently under investigation. As obtained from CD curves recorded at 0.1 mA cm^{-2} (inset of Figure 67b), C_{areal} values of 1.21 and 1.17 mF cm^{-2} were obtained in a voltage windows of 1.4 and 1.8 V, respectively. Notably, these values are comparable to those measured on reference device before sealing and washing processes (1.10 mF cm^{-2} at current density of 0.1 mA cm^{-2}).

CONCLUSIONS

In summary, in this thesis I explored the implementation of printed 2D materials devices such as graphene-based antennas and supercapacitors as well as InSe-based photodetectors, representing potential building blocks of a printed wireless sensing system.

The successful introduction of 2D materials in the context of electronic applications, strongly depends not only on the identification of disruptive products for radically new applications, but also on the ability to produce the materials in large quantities and at a reasonable cost. For this reason, I investigated an innovative method to exfoliate bulk materials by wet-jet milling technology. Wet-jet milling exfoliation of graphite in NMP allowed for production of large volumes (litre-scale) of concentrated high quality (single-/few-layers graphene) graphene dispersions (gram per litre-scale) in short times (second-scale). More in detail, the time required to obtain 1 g of exfoliated material was 2.55 min g^{-1}, while the volume of solvent required to produce 1 g of exfoliated material with 100% yield was 0.1 L g^{-1}. By additivation of these graphene dispersions, I developed pastes suitable for printing antennas and supercapacitors. One formulation, suitable for printing bow-tie antennas on cardboard, included graphene powder with a small amount of silver ink, to improve conductivity, and an overprint varnish as binder, in order to guarantee the adhesion of the pattern to the paper and the durability of the print. Mass loading of both graphene (9.6 wt%) and silver (1.4 wt%) was much lower than the commercial silver inks (~79% wt%). The resulting antennas showed an ultra-wideband behaviour (fractional band 45%) centred at 2 GHz. This novel approach opens the route to low cost printed antennas based on graphene that do not require thermal post treatment and are suitable for a wide variety of applications including satellite communications, mobile service, digital audio broadcasting, astronomy and RFIDs.

On the other hand, the WJM-graphene dispersion has been used for the realization of solid-state and washable micro-supercapacitors (MSCs) printed by screen printing technique. In order to provide a screen printable ink to fabricate flexible solid-state MSCs on plastic substrate, a simple solvent-exchange process was carried out to re-disperse the WJM-graphene in H_2O/EtOH (70:30) and terpineol (1 wt%). The addition of single-walled carbon nanotubes (SWCNTs) dispersion in EtOH to WJM-graphene ink and the use of pyrolytic graphite (PG) paper as current collector were also evaluated for increasing the active film porosity and decrease the electrical equivalent series resistance (ESR) of the MSCs, respectively. The optimized MSCs exhibited areal capacitance (C_{areal}) up to 1.324 mF cm^{-2} (5.296 mF cm^{-2} for a single electrode) and volumetric capacitance (C_{vol}) of 0.490 F cm^{-3} (1.961 F cm^{-3} in electrode). The screen-printed MSCs also showed high-rate performance

(voltage scan rate > 10 V s^{-1} and charge/discharge current density up to 25 mA cm^{-2}) which allowed for a power density of 20.13 and 1.13 mW cm^{-2} at energy density of 0.064 and 0.361 μWh cm^{-2}, respectively. The devices also exhibited excellent electrochemical and mechanical properties over charge-discharge cycling (10000 times), bending cycles (100 times under bending radius of 1 cm), and folding (up to angles of 180°). Moreover, water-proof ethylene vinyl acetate (EVA)-encapsulated MSCs fully retained their electrochemical properties after a home-laundry cycle, providing washable properties for prospective wearable electronics.

Finally, I exfoliated beta-phase indium selenide by liquid phase exfoliation driven by ultrasounds, using a low environmental impact solvent such as isopropanol. This ink was successfully sprayed onto gold electrodes on silicon substrates. I demonstrated that spray coated liquid phase exfoliated β -InSe films can be used as semiconductor channel material in phototransistors, obtaining a potentially high-throughput and low-cost method to implement photodetectors with high sensitivity (maximum $D^* \sim 5.49\ 10^{12}$ Jones, $R_{ph} \sim 274$ A W^{-1} @ 455 nm illumination) and fast response time (τ_R ~15 ms, $\tau_F \sim 64$ ms). The devices showed good photosensitive responsivity to visible and NIR (< 900 nm) light. These FoMs represent an improvement of over one order of magnitude with respect to reported photodetectors based on percolating networks of solution processed 2D flakes and are competitive with the values reported for transition metal dichalcogenide single flake devices. The use of spray coating and environmentally friendly solvents in the fabrication process make this material suitable for the implementation of flexible-photodetectors and in applications where contamination by toxic organic solvents can be a problem.

In conclusion, the work in this thesis dealt with the development of printed components of an integrated sensing system from solution processed exfoliated crystals. This field is very promising and will play an important role on the development of versatile wireless technologies which can find application in many fields, ranging from healthcare, safety, security, environmental monitoring, food and pharmaceutical inspection to data communication, smartphone cameras, night vision, and automotive sensor systems. However, the project is still in its early stages and further steps must be taken towards the integration of the devices into a standalone system. As for the implementation of a flexible and wearable system, InSe photodetector should be fabricated on a plastic substrate using printed electrodes. Furthermore, the addition of other types of energy suppliers besides supercapacitors (such as printed solar cells) can bring numerous benefits, including the possibility to feed the system continuously through light. Finally, future work should concentrate on the challenges related to the interconnection of the various components in a single system, which were not possible to address during the PhD.

REFERENCES

[1] D. Akinwande *et al.*, "A review on mechanics and mechanical properties of 2D materials—Graphene and beyond," *Extrem. Mech. Lett.*, vol. 13, pp. 42–77, May 2017.

[2] K. S. Novoselov *et al.*, "Two-dimensional atomic crystals," *Proc. Natl. Acad. Sci.*, vol. 102, no. 30, pp. 10451–10453, Jul. 2005.

[3] A. H. Castro Neto, F. Guinea, N. M. R. Peres, K. S. Novoselov, and A. K. Geim, "The electronic properties of graphene," *Rev. Mod. Phys.*, vol. 81, no. 1, pp. 109–162, Jan. 2009.

[4] A. C. Ferrari *et al.*, "Science and technology roadmap for graphene, related two-dimensional crystals, and hybrid systems," *Nanoscale*, vol. 7, no. 11, pp. 4598–4810, 2014.

[5] F. Bonaccorso *et al.*, "2D materials. Graphene, related two-dimensional crystals, and hybrid systems for energy conversion and storage," *Science*, vol. 347, no. 6217, p. 1246501, 2015.

[6] E. Gao, S.-Z. Lin, Z. Qin, M. J. Buehler, X.-Q. Feng, and Z. Xu, "Mechanical exfoliation of two-dimensional materials," *J. Mech. Phys. Solids*, vol. 115, pp. 248–262, Jun. 2018.

[7] M. S. Fuhrer and J. Hone, "Measurement of mobility in dual-gated MoS2 transistors," *Nat. Nanotechnol.*, vol. 8, no. 3, pp. 146–147, Mar. 2013.

[8] C. R. Dean *et al.*, "Boron nitride substrates for high-quality graphene electronics," *Nat. Nanotechnol.*, vol. 5, no. 10, pp. 722–726, 2010.

[9] R. D. Y. Hills *et al.*, "FROM GRAPHENE AND TOPOLOGICAL INSULATORS TO WEYL SEMIMETALS," in *Symmetry, Spin Dynamics and the Properties of Nanostructures*, 2015, pp. 277–315.

[10] M. C. dos Santos, M. C. Maynart, L. R. Aveiro, E. C. da Paz, and V. dos Santos Pinheiro, "Carbon-Based Materials: Recent Advances, Challenges, and Perspectives," in *Reference Module in Materials Science and Materials Engineering*, Elsevier, 2017.

[11] M. S. Dresselhaus, G. Dresselhaus, and R. Saito, "Physics of carbon nanotubes," *Carbon N. Y.*, vol. 33, no. 7, pp. 883–891, Jan. 1995.

[12] M. F. L. De Volder, S. H. Tawfick, R. H. Baughman, and A. J. Hart, "Carbon Nanotubes: Present and Future Commercial Applications," *Science*, vol. 339, no. 6119, pp. 535–539, Feb. 2013.

[13] Z. Han and A. Fina, “Thermal conductivity of carbon nanotubes and their polymer nanocomposites: A review,” *Prog. Polym. Sci.*, vol. 36, no. 7, pp. 914–944, Jul. 2011.

[14] Y.-S. Kim, K. Kumar, F. T. Fisher, and E.-H. Yang, “Out-of-plane growth of CNTs on graphene for supercapacitor applications,” *Nanotechnology*, vol. 23, no. 1, p. 015301, Jan. 2012.

[15] K. S. Ibrahim, “Carbon nanotubes-properties and applications: a review,” *Carbon Lett.*, vol. 14, no. 3, pp. 131–144, Jul. 2013.

[16] B. Arash, Q. Wang, and V. K. Varadan, “Mechanical properties of carbon nanotube/polymer composites,” *Sci. Rep.*, vol. 4, no. 1, p. 6479, May 2015.

[17] Y. Omata, Y. Yamagami, K. Tadano, T. Miyake, and S. Saito, “Nanotube nanoscience: A molecular-dynamics study,” *Phys. E Low-dimensional Syst. Nanostructures*, vol. 29, no. 3–4, pp. 454–468, Nov. 2005.

[18] S. Iijima, “Helical microtubules of graphitic carbon,” *Nature*, vol. 354, no. 6348, pp. 56–58, Nov. 1991.

[19] “Contents of Volume I,” *Spin Arrange. Cryst. Struct. Domains, Micromagnetics*, p. xiii, Jan. 1963.

[20] Z. Liu, S.-M. Zhang, J.-R. Yang, J. Z. Liu, Y.-L. Yang, and Q.-S. Zheng, “Interlayer shear strength of single crystalline graphite,” *Acta Mech. Sin.*, vol. 28, no. 4, pp. 978–982, Aug. 2012.

[21] P. L. de Andres, R. Ramírez, and J. A. Vergés, “Strong covalent bonding between two graphene layers,” *Phys. Rev. B*, vol. 77, no. 4, p. 045403, Jan. 2008.

[22] J. C. Meyer, A. K. Geim, M. I. Katsnelson, K. S. Novoselov, T. J. Booth, and S. Roth, “The structure of suspended graphene sheets,” *Nature*, vol. 446, no. 7131, pp. 60–63, Mar. 2007.

[23] W. Wang, S. Dai, X. Li, J. Yang, D. J. Srolovitz, and Q. Zheng, “Measurement of the cleavage energy of graphite,” *Nat. Commun.*, vol. 6, no. 1, p. 7853, Nov. 2015.

[24] A. S. Mayorov *et al.*, “Micrometer-Scale Ballistic Transport in Encapsulated Graphene at Room Temperature,” *Nano Lett.*, vol. 11, no. 6, pp. 2396–2399, Jun. 2011.

[25] J. Moser, A. Barreiro, and A. Bachtold, “Current-induced cleaning of graphene,” *Appl. Phys. Lett.*, vol. 91, no. 16, p. 163513, Oct. 2007.

[26] Y. Zhang, Y.-W. Tan, H. L. Stormer, and P. Kim, “Experimental observation of the quantum Hall effect and Berry’s phase in graphene,” *Nature*, vol. 438, no. 7065, pp. 201–204, Nov. 2005.

[27] K. S. Novoselov *et al.*, “Room-temperature quantum Hall effect in graphene.,” *Science*, vol. 315, no. 5817, p. 1379, Mar. 2007.

[28] A. A. Balandin *et al.*, “Superior Thermal Conductivity of Single-Layer Graphene,” *Nano Lett.*, vol. 8, no. 3, pp. 902–907, Mar. 2008.

[29] E. Pop, V. Varshney, and A. K. Roy, “Thermal properties of graphene: Fundamentals and applications,” *MRS Bull.*, vol. 37, no. 12, pp. 1273–1281, Dec. 2012.

[30] M. Sang, J. Shin, K. Kim, and K. Yu, “Electronic and Thermal Properties of Graphene and Recent Advances in Graphene Based Electronics Applications,” *Nanomaterials*, vol. 9, no. 3, p. 374, Mar. 2019.

[31] V. Singh, D. Joung, L. Zhai, S. Das, S. I. Khondaker, and S. Seal, “Graphene based materials: Past, present and future,” *Prog. Mater. Sci.*, vol. 56, no. 8, pp. 1178–1271, Oct. 2011.

[32] K. F. Mak, C. H. Lui, and T. F. Heinz, “Thermal conductance at the graphene-SiO2 interface measured by optical pump-probe spectroscopy,” Sep. 2010.

[33] K. F. Mak, J. Shan, and T. F. Heinz, “Electronic Structure of Few-Layer Graphene: Experimental Demonstration of Strong Dependence on Stacking Sequence,” *Phys. Rev. Lett.*, vol. 104, no. 17, p. 176404, Apr. 2010.

[34] A. K. Geim and K. S. Novoselov, “The rise of graphene,” *Nat. Mater.*, vol. 6, no. 3, pp. 183–191, 2007.

[35] R. R. Nair *et al.*, “Fine Structure Constant Defines Visual Transparency of Graphene,” *Science*, vol. 320, no. 5881, pp. 1308–1308, Jun. 2008.

[36] V. G. Kravets *et al.*, “Spectroscopic ellipsometry of graphene and an exciton-shifted van Hove peak in absorption,” *Phys. Rev. B*, vol. 81, no. 15, p. 155413, Apr. 2010.

[37] A. B. Kuzmenko, E. van Heumen, F. Carbone, and D. van der Marel, “Universal Optical Conductance of Graphite,” *Phys. Rev. Lett.*, vol. 100, no. 11, p. 117401, Mar. 2008.

[38] N. Savage, “Materials science: Super carbon,” *Nature*, vol. 483, no. 7389, pp. S30–S31, Mar. 2012.

[39] F. Guinea and T. Low, “Band structure and gaps of triangular graphene superlattices,” *Philos. Trans. R. Soc. A Math. Phys. Eng. Sci.*, vol. 368, no. 1932, pp. 5391–5402, Dec. 2010.

[40] A. C. Ferrari *et al.*, “Science and technology roadmap for graphene, related two-dimensional crystals, and hybrid systems,” *Nanoscale*, vol. 7, no. 11, pp. 4598–4810, Mar. 2015.

[41] W. Choi, N. Choudhary, G. H. Han, J. Park, D. Akinwande, and Y. H. Lee, “Recent development of two-dimensional transition metal dichalcogenides and their applications,” *Mater. Today*, vol. 20, no. 3, pp. 116–130, Apr. 2017.

[42] V. Nicolosi, M. Chhowalla, M. G. Kanatzidis, M. S. Strano, and J. N. Coleman, “Liquid Exfoliation of Layered Materials,” *Science*, vol. 340, no. 6139, pp. 1226419–1226419, Jun. 2013.

[43] M. Chhowalla, H. S. Shin, G. Eda, L.-J. Li, K. P. Loh, and H. Zhang, “The chemistry of two-dimensional layered transition metal dichalcogenide nanosheets,” *Nat. Chem.*, vol. 5, no. 4, pp. 263–275, Apr. 2013.

[44] C.-H. Lee *et al.*, “Tungsten Ditelluride: a layered semimetal,” *Sci. Rep.*, vol. 5, no. 1, p. 10013, Sep. 2015.

[45] A. B. Laursen, S. Kegnæs, S. Dahl, and I. Chorkendorff, “Molybdenum sulfides—efficient and viable materials for electro - and photoelectrocatalytic hydrogen evolution,” *Energy Environ. Sci.*, vol. 5, no. 2, p. 5577, 2012.

[46] B. Hinnemann *et al.*, “Biomimetic Hydrogen Evolution: MoS 2 Nanoparticles as Catalyst for Hydrogen Evolution,” *J. Am. Chem. Soc.*, vol. 127, no. 15, pp. 5308–5309, Apr. 2005.

[47] A. Kuc, N. Zibouche, and T. Heine, “Influence of quantum confinement on the electronic structure of the transition metal sulfide,” *Phys. Rev. B*, vol. 83, no. 24, p. 245213, Jun. 2011.

[48] W. Bao, X. Cai, D. Kim, K. Sridhara, and M. S. Fuhrer, “High mobility ambipolar MoS 2 field-effect transistors: Substrate and dielectric effects,” *Appl. Phys. Lett.*, vol. 102, no. 4, p. 042104, Jan. 2013.

[49] M. R. Islam *et al.*, “Tuning the electrical property via defect engineering of single layer MoS 2 by oxygen plasma,” *Nanoscale*, vol. 6, no. 17, p. 10033, Jun. 2014.

[50] K. F. Mak, C. Lee, J. Hone, J. Shan, and T. F. Heinz, “Atomically Thin MoS2: A New Direct-Gap Semiconductor,” *Phys. Rev. Lett.*, vol. 105, no. 13, p. 136805, Sep. 2010.

[51] N. Choudhary, M. R. Islam, N. Kang, L. Tetard, Y. Jung, and S. I. Khondaker, "Two-dimensional lateral heterojunction through bandgap engineering of MoS 2 via oxygen plasma," *J. Phys. Condens. Matter*, vol. 28, no. 36, p. 364002, Sep. 2016.

[52] K. Feng, D. Mei, L. Bai, Z. Lin, J. Yao, and Y. Wu, "Synthesis, structure, physical properties, and electronic structure of KGaSe2," *Solid State Sci.*, vol. 14, no. 8, pp. 1152–1156, Aug. 2012.

[53] D. Boukhvalov *et al.*, "The Advent of Indium Selenide: Synthesis, Electronic Properties, Ambient Stability and Applications," *Nanomaterials*, vol. 7, no. 11, p. 372, Nov. 2017.

[54] S.-R. Zhang, S.-F. Zhu, B.-J. Zhao, L.-H. Xie, and K.-H. Song, "First-principles study of the elastic, electronic and optical properties of ε-GaSe layered semiconductor," *Phys. B Condens. Matter*, vol. 436, pp. 188–192, Mar. 2014.

[55] S. M. Tan, A. Ambrosi, Z. Sofer, Š. Huber, D. Sedmidubský, and M. Pumera, "Pristine Basal- and Edge-Plane-Oriented Molybdenite MoS 2 Exhibiting Highly Anisotropic Properties," *Chem. - A Eur. J.*, vol. 21, no. 19, pp. 7170–7178, May 2015.

[56] S. M. Tan, C. K. Chua, D. Sedmidubský, Z. Sofer, and M. Pumera, "Electrochemistry of layered GaSe and GeS: applications to ORR, OER and HER," *Phys. Chem. Chem. Phys.*, vol. 18, no. 3, pp. 1699–1711, 2016.

[57] J.-H. Park, M. Afzaal, M. Helliwell, M. A. Malik, P. O'Brien, and J. Raftery, "Chemical Vapor Deposition of Indium Selenide and Gallium Selenide Thin Films from Mixed Alkyl/Dialkylselenophosphorylamides," *Chem. Mater.*, vol. 15, no. 22, pp. 4205–4210, Nov. 2003.

[58] D. M. Rowe, *CRC Handbook of Thermoelectrics*. .

[59] Y. Ni, H. Wu, C. Huang, M. Mao, Z. Wang, and X. Cheng, "Growth and quality of gallium selenide (GaSe) crystals," *J. Cryst. Growth*, vol. 381, pp. 10–14, Oct. 2013.

[60] S. Asanabe and A. Okazaki, "Electrical Properties of Germanium Selenide GeSe," *J. Phys. Soc. Japan*, vol. 15, no. 6, pp. 989–997, Jun. 1960.

[61] T. P. Gujar, V. R. Shinde, J.-W. Park, H. K. Lee, K.-D. Jung, and O.-S. Joo, "Electrodeposition of photoactive 1D gallium selenide quantum dots," *Electrochim. Acta*, vol. 54, no. 2, pp. 829–834, Dec. 2008.

[62] J.-H. Jeong, D.-W. Jung, and E.-S. Oh, "Lithium storage characteristics of a new promising

gallium selenide anodic material," *J. Alloys Compd.*, vol. 613, pp. 42–45, Nov. 2014.

[63] S. Gedi, V. R. Minnam Reddy, C. Park, J. Chan-Wook, and R. R. K.T., "Comprehensive optical studies on SnS layers synthesized by chemical bath deposition," *Opt. Mater. (Amst).*, vol. 42, pp. 468–475, Apr. 2015.

[64] H. Li, J. Ji, X. Zheng, Y. Ma, Z. Jin, and H. Ji, "Preparation of SnS quantum dots for solar cells application by an in-situ solution chemical reaction process," *Mater. Sci. Semicond. Process.*, vol. 36, pp. 65–70, Aug. 2015.

[65] A. Srivastava and R. Chandiramouli, "Band structure and transport studies on impurity substituted InSe nanosheet – A first-principles investigation," *Superlattices Microstruct.*, vol. 79, pp. 135–147, Mar. 2015.

[66] A. G. Kunjomana, K. A. Chandrasekharan, and M. Teena, "Physical properties of vapour grown indium monotelluride platelets," *J. Cryst. Growth*, vol. 411, pp. 81–87, Feb. 2015.

[67] A. Harvey *et al.*, "Preparation of Gallium Sulfide Nanosheets by Liquid Exfoliation and Their Application As Hydrogen Evolution Catalysts," *Chem. Mater.*, vol. 27, no. 9, pp. 3483–3493, May 2015.

[68] K. Ariga *et al.*, "Layer-by-layer Nanoarchitectonics: Invention, Innovation, and Evolution," *Chem. Lett.*, vol. 43, no. 1, pp. 36–68, Jan. 2014.

[69] † Hailin Peng, † Stefan Meister, ‡ Candace K. Chan, § and Xiao Feng Zhang, and † Yi Cui*, "Morphology Control of Layer-Structured Gallium Selenide Nanowires," 2006.

[70] S. Lei *et al.*, "Evolution of the Electronic Band Structure and Efficient Photo-Detection in Atomic Layers of InSe," *ACS Nano*, vol. 8, no. 2, pp. 1263–1272, Feb. 2014.

[71] G. Han, Z.-G. Chen, J. Drennan, and J. Zou, "Indium Selenides: Structural Characteristics, Synthesis and Their Thermoelectric Performances," *Small*, vol. 10, no. 14, pp. 2747–2765, Jul. 2014.

[72] B. Gürbulak, M. Şata, S. Dogan, S. Duman, A. Ashkhasi, and E. F. Keskenler, "Structural characterizations and optical properties of InSe and InSe:Ag semiconductors grown by Bridgman/Stockbarger technique," *Phys. E Low-dimensional Syst. Nanostructures*, vol. 64, pp. 106–111, Nov. 2014.

[73] G. W. Mudd *et al.*, "Quantum confined acceptors and donors in InSe nanosheets," *Appl. Phys. Lett.*, vol. 105, no. 22, p. 221909, Dec. 2014.

[74] J. F. Sánchez-Royo *et al.*, “Electronic structure, optical properties, and lattice dynamics in atomically thin indium selenide flakes,” *Nano Res.*, vol. 7, no. 10, pp. 1556–1568, Oct. 2014.

[75] C.-H. Ho, “Thickness-dependent carrier transport and optically enhanced transconductance gain in III-VI multilayer InSe,” *2D Mater.*, vol. 3, no. 2, p. 025019, May 2016.

[76] W. Jie *et al.*, “Layer-Dependent Nonlinear Optical Properties and Stability of Non-Centrosymmetric Modification in Few-Layer GaSe Sheets,” *Angew. Chemie Int. Ed.*, vol. 54, no. 4, pp. 1185–1189, Jan. 2015.

[77] W. Feng, X. Zhou, W. Q. Tian, W. Zheng, and P. Hu, “Performance improvement of multilayer InSe transistors with optimized metal contacts,” *Phys. Chem. Chem. Phys.*, vol. 17, no. 5, pp. 3653–3658, 2015.

[78] G. W. Mudd *et al.*, “Tuning the Bandgap of Exfoliated InSe Nanosheets by Quantum Confinement,” *Adv. Mater.*, vol. 25, no. 40, pp. 5714–5718, Oct. 2013.

[79] C. M. Julien and M. Balkanski, “Lithium reactivity with III–VI layered compounds,” *Mater. Sci. Eng. B*, vol. 100, no. 3, pp. 263–270, Jul. 2003.

[80] L. Viti *et al.*, “Black Phosphorus Terahertz Photodetectors,” *Adv. Mater.*, vol. 27, no. 37, pp. 5567–5572, Oct. 2015.

[81] “Optical Nonlinearities in Chalcogenide Fibres,” in *Optical Nonlinearities in Chalcogenide Glasses and their Applications*, Berlin, Heidelberg: Springer Berlin Heidelberg, pp. 107–128.

[82] G. Shen, D. Chen, P.-C. Chen, and C. Zhou, “Vapor−Solid Growth of One-Dimensional Layer-Structured Gallium Sulfide Nanostructures,” *ACS Nano*, vol. 3, no. 5, pp. 1115–1120, May 2009.

[83] N. B. Singh *et al.*, “Far-infrared conversion materials: Gallium selenide for far-infrared conversion applications,” *Prog. Cryst. Growth Charact. Mater.*, vol. 37, no. 1, pp. 47–102, Jan. 1998.

[84] F. Bonaccorso and Z. Sun, “Solution processing of graphene, topological insulators and other 2d crystals for ultrafast photonics,” *Opt. Mater. Express*, vol. 4, no. 1, p. 63, Jan. 2014.

[85] F. Bonaccorso, A. Lombardo, T. Hasan, Z. Sun, L. Colombo, and A. C. Ferrari, “Production and processing of graphene and 2d crystals,” *Mater. Today*, vol. 15, no. 12, pp. 564–589, 2012.

[86] K. S. K. S. Novoselov *et al.*, “Electric field effect in atomically thin carbon films.,” *Science*,

vol. 306, no. October, pp. 666–669, 2004.

[87] M. J. Allen, M. Wang, S. A. V. Jannuzzi, Y. Yang, K. L. Wang, and R. B. Kaner, "Chemically induced folding of single and bilayer graphene," *Chem. Commun.*, vol. 0, no. 41, p. 6285, Oct. 2009.

[88] F. Bonaccorso, A. Lombardo, T. Hasan, Z. Sun, L. Colombo, and A. C. Ferrari, "Production and processing of graphene and 2d crystals," *Mater. Today*, vol. 15, no. 12, pp. 564–589, Dec. 2012.

[89] A. K. Geim, "Graphene: status and prospects.," *Science*, vol. 324, no. 5934, pp. 1530–4, Jun. 2009.

[90] Y. Chen *et al.*, "Mechanically exfoliated black phosphorus as a new saturable absorber for both Q-switching and Mode-locking laser operation," *Opt. Express*, vol. 23, no. 10, p. 12823, May 2015.

[91] Y. Chen, X.-L. Gong, and J.-G. Gai, "Progress and Challenges in Transfer of Large-Area Graphene Films," *Adv. Sci.*, vol. 3, no. 8, p. 1500343, Aug. 2016.

[92] C. Casiraghi, S. Pisana, K. S. Novoselov, A. K. Geim, and A. C. Ferrari, "Raman fingerprint of charged impurities in graphene," *Appl. Phys. Lett.*, vol. 91, no. 23, p. 233108, Dec. 2007.

[93] A. C. Ferrari and D. M. Basko, "Raman spectroscopy as a versatile tool for studying the properties of graphene," *Nat. Nanotechnol.*, vol. 8, no. 4, pp. 235–246, Apr. 2013.

[94] A. C. Ferrari *et al.*, "Raman Spectrum of Graphene and Graphene Layers," *Phys. Rev. Lett.*, vol. 97, no. 18, p. 187401, Oct. 2006.

[95] V. Nicolosi, M. Chhowalla, M. G. Kanatzidis, M. S. Strano, and J. N. Coleman, "Liquid Exfoliation of Layered Materials," *Science*, vol. 340, no. 6139, 2013.

[96] F. Torrisi *et al.*, "Inkjet-Printed Graphene Electronics," *ACS Nano*, vol. 6, no. 4, pp. 2992–3006, Apr. 2012.

[97] Y. Hernandez *et al.*, "High-yield production of graphene by liquid-phase exfoliation of graphite," *Nat. Nanotechnol.*, vol. 3, p. 563, Aug. 2008.

[98] A. Capasso, A. E. Del Rio Castillo, H. Sun, A. Ansaldo, V. Pellegrini, and F. Bonaccorso, "Ink-jet printing of graphene for flexible electronics: An environmentally-friendly approach," *Solid State Commun.*, vol. 224, pp. 53–63, 2015.

[99] E. . Morgan, “Vogel’s textbook of practical organic chemistry. 5th edn.,” *Endeavour*, vol. 14, no. 3, p. 148, Jan. 1990.

[100] M. Yi, Z. Shen, X. Zhang, and S. Ma, “Achieving concentrated graphene dispersions in water/acetone mixtures by the strategy of tailoring Hansen solubility parameters,” *J. Phys. D. Appl. Phys.*, vol. 46, no. 2, p. 025301, Jan. 2013.

[101] J. N. Coleman and et al. et al., “ChemInform Abstract: Two-Dimensional Nanosheets Produced by Liquid Exfoliation of Layered Materials.,” *ChemInform*, vol. 42, no. 18, p. no-no, May 2011.

[102] Y. Yan, L. Piao, S.-H. Kim, W. Li, and H. Zhou, “Effect of Pluronic block copolymers on aqueous dispersions of graphene oxide,” *RSC Adv.*, vol. 5, no. 50, pp. 40199–40204, May 2015.

[103] U. Halim *et al.*, “A rational design of cosolvent exfoliation of layered materials by directly probing liquid–solid interaction,” *Nat. Commun.*, vol. 4, no. 1, p. 2213, Oct. 2013.

[104] E. Petroni *et al.*, “Liquid-Phase Exfoliated Indium-Selenide Flakes and Their Application in Hydrogen Evolution Reaction,” *Small*, vol. 1800749, p. 1800749, 2018.

[105] A. O’Neill, U. Khan, P. N. Nirmalraj, J. Boland, and J. N. Coleman, “Graphene Dispersion and Exfoliation in Low Boiling Point Solvents,” *J. Phys. Chem. C*, vol. 115, no. 13, pp. 5422–5428, Apr. 2011.

[106] F. Torrisi *et al.*, “Inkjet-printed graphene electronics,” *ACS Nano*, vol. 6, no. 4, pp. 2992–3006, 2012.

[107] M. Lotya *et al.*, “Liquid Phase Production of Graphene by Exfoliation of Graphite in Surfactant/Water Solutions,” *J. Am. Chem. Soc.*, vol. 131, no. 10, pp. 3611–3620, Mar. 2009.

[108] Y.-J. Wan *et al.*, “Improved dispersion and interface in the graphene/epoxy composites via a facile surfactant-assisted process,” *Compos. Sci. Technol.*, vol. 82, pp. 60–68, Jun. 2013.

[109] I. S. Khattab, F. Bandarkar, M. A. A. Fakhree, and A. Jouyban, “Density, viscosity, and surface tension of water+ethanol mixtures from 293 to 323K,” *Korean J. Chem. Eng.*, vol. 29, no. 6, pp. 812–817, Jun. 2012.

[110] J. N. Coleman *et al.*, “Two-Dimensional Nanosheets Produced by Liquid Exfoliation of Layered Materials,” *Science*, vol. 331, no. 6017, pp. 568–571, Feb. 2011.

[111] K. R. Paton *et al.*, “Scalable production of large quantities of defect-free few-layer graphene

by shear exfoliation in liquids," *Nat. Mater.*, vol. 13, no. 6, pp. 624–630, Jun. 2014.

[112] S. Biccai *et al.*, "Exfoliation of 2D materials by high shear mixing," *2D Mater.*, vol. 6, no. 1, p. 015008, Oct. 2018.

[113] Y. Yao, Z. Lin, Z. Li, X. Song, K.-S. Moon, and C. Wong, "Large-scale production of two-dimensional nanosheets," *J. Mater. Chem.*, vol. 22, no. 27, p. 13494, 2012.

[114] L. Hua Li, Y. Chen, B.-M. Cheng, M.-Y. Lin, S.-L. Chou, and Y.-C. Peng, "Photoluminescence of boron nitride nanosheets exfoliated by ball milling," *Appl. Phys. Lett.*, vol. 100, no. 26, p. 261108, Jun. 2012.

[115] A. E. Del Rio Castillo *et al.*, "High-yield production of 2D crystals by wet-jet milling," *Mater. Horizons*, vol. 5, no. 5, pp. 890–904, 2018.

[116] P. G. Karagiannidis *et al.*, "Microfluidization of Graphite and Formulation of Graphene-Based Conductive Inks," *ACS Nano*, vol. 11, no. 3, pp. 2742–2755, Mar. 2017.

[117] K. Kouroupis-Agalou *et al.*, "Fragmentation and exfoliation of 2-dimensional materials: a statistical approach," *Nanoscale*, vol. 6, no. 11, pp. 5926–5933, 2014.

[118] Y. Hernandez *et al.*, "High-yield production of graphene by liquid-phase exfoliation of graphite," *Nat. Nanotechnol.*, vol. 3, no. 9, pp. 563–568, Sep. 2008.

[119] S. Bellani *et al.*, "Scalable Production of Graphene Inks via Wet-Jet Milling Exfoliation for Screen-Printed Micro-Supercapacitors," *Adv. Funct. Mater.*, p. 1807659, Feb. 2019.

[120] K. O. Pedersen, "The development of svedberg's ultracentrifuge," *Biophys. Chem.*, vol. 5, no. 1–2, pp. 3–18, Jul. 1976.

[121] H. Freundlich, "The Ultracentrifuge. By The Svedberg and Kai O. Pedersen.," *J. Phys. Chem.*, vol. 44, no. 7, pp. 952–953, Jul. 1940.

[122] M. Behrens, "Über die Verteilung: der Lipase und Arginase zwischen Zellkern und Protoplasma der Leber. Mit 1 Figur im Text.," *Hoppe-Seyler´s Zeitschrift für Physiol. Chemie*, vol. 258, no. 1, pp. 27–32, Jan. 1939.

[123] F. Bonaccorso, A. Bartolotta, J. N. Coleman, and C. Backes, "2D-Crystal-Based Functional Inks," *Adv. Mater.*, vol. 28, no. 29, pp. 6136–6166, Aug. 2016.

[124] U. Khan, H. Porwal, A. O'Neill, K. Nawaz, P. May, and J. N. Coleman, "Solvent-Exfoliated Graphene at Extremely High Concentration," *Langmuir*, vol. 27, no. 15, pp. 9077–9082,

Aug. 2011.

[125] A. A. Green and M. C. Hersam, “Solution Phase Production of Graphene with Controlled Thickness via Density Differentiation,” *Nano Lett.*, vol. 9, no. 12, pp. 4031–4036, Dec. 2009.

[126] X. Li *et al.*, “Large-area synthesis of high-quality and uniform graphene films on copper foils,” *Science*, vol. 324, no. 5932, pp. 1312–4, Jun. 2009.

[127] Z. Cai, B. Liu, X. Zou, and H.-M. Cheng, “Chemical Vapor Deposition Growth and Applications of Two-Dimensional Materials and Their Heterostructures,” *Chem. Rev.*, vol. 118, no. 13, pp. 6091–6133, Jul. 2018.

[128] S. Mikhailov, *Physics and Applications of Graphene - Experiments.* InTech.

[129] J. K. Rath, H. Meiling, and R. E. I. Schropp, “Low-temperature deposition of polycrystalline silicon thin films by hot-wire CVD,” *Sol. Energy Mater. Sol. Cells*, vol. 48, no. 1–4, pp. 269–277, Nov. 1997.

[130] M. Werner and R. Locher, “Growth and application of undoped and doped diamond films,” *Reports Prog. Phys.*, vol. 61, no. 12, pp. 1665–1710, Dec. 1998.

[131] J. Fujita *et al.*, “Near room temperature chemical vapor deposition of graphene with diluted methane and molten gallium catalyst,” *Sci. Rep.*, vol. 7, no. 1, p. 12371, Dec. 2017.

[132] Y. Zhang *et al.*, “Recent Progress in CVD Growth of 2D Transition Metal Dichalcogenides and Related Heterostructures,” *Adv. Mater.*, vol. 31, no. 41, p. 1901694, Oct. 2019.

[133] “SINGLE ZONE CVD FURNACE.” [Online]. Available: https://www.vistec-technology.com/product/high-temperature-tube-furnace/. [Accessed: 14-Oct-2019].

[134] A. Capasso, A. E. Del Rio Castillo, H. Sun, A. Ansaldo, V. Pellegrini, and F. Bonaccorso, “Ink-jet printing of graphene for flexible electronics: An environmentally-friendly approach,” *Solid State Commun.*, vol. 224, pp. 53–63, Dec. 2015.

[135] T. Carey, C. Jones, F. Le Moal, D. Deganello, and F. Torrisi, “Spray-Coating Thin Films on Three-Dimensional Surfaces for a Semitransparent Capacitive-Touch Device,” *ACS Appl. Mater. Interfaces*, vol. 10, no. 23, pp. 19948–19956, Jun. 2018.

[136] P. Samorì and V. Palermo, *Flexible Carbon-based Electronics*. Weinheim, Germany Wiley-VCH Verlag GmbH & Co. KGaA, 2018.

[137] “Characteristics and Behavior of Nanoparticles and Its Dispersion Systems,” in *Nanoparticle*

Technology Handbook, Elsevier, 2018, pp. 109–168.

[138] G. Hu *et al.*, "Functional inks and printing of two-dimensional materials," *Chem. Soc. Rev.*, vol. 47, no. 9, pp. 3265–3300, 2018.

[139] A. Pekarovicova and V. Husovska, "Printing Ink Formulations," in *Printing on Polymers*, Elsevier, 2016, pp. 41–55.

[140] H. Sirringhaus *et al.*, "High-Resolution Inkjet Printing of All-Polymer Transistor Circuits," *Science*, vol. 290, no. 5499, pp. 2123–2126, Dec. 2000.

[141] J. Weiner and F. Nunes, *Light-matter Interaction : physics and engineering at the nanoscale.* Oxford University Press, 2017.

[142] A. T. Young, "Rayleigh scattering," *Appl. Opt.*, vol. 20, no. 4, p. 533, Feb. 1981.

[143] D. F. Swinehart, "The Beer-Lambert Law," *J. Chem. Educ.*, vol. 39, no. 7, p. 333, Jul. 1962.

[144] M. Lotya, P. J. King, U. Khan, S. De, and J. N. Coleman, "High-Concentration, Surfactant-Stabilized Graphene Dispersions," *ACS Nano*, vol. 4, no. 6, pp. 3155–3162, Jun. 2010.

[145] A. C. Ferrari, "Raman spectroscopy of graphene and graphite: Disorder, electron-phonon coupling, doping and nonadiabatic effects," *Solid State Commun.*, vol. 143, no. 1–2, pp. 47–57, 2007.

[146] F. Liang, H. Xu, X. Wu, C. Wang, C. Luo, and J. Zhang, "Raman spectroscopy characterization of two-dimensional materials," *Chinese Phys. B*, vol. 27, no. 3, p. 037802, Mar. 2018.

[147] C. F. Bohren and D. R. Huffman, *Absorption and Scattering of Light by Small Particles*. Wiley.

[148] W. R. Browne and J. J. McGarvey, "The Raman effect and its application to electronic spectroscopies in metal-centered species: Techniques and investigations in ground and excited states," *Coord. Chem. Rev.*, vol. 251, no. 3–4, pp. 454–473, Feb. 2007.

[149] "Raman." [Online]. Available: http://bodyyouknow.org/sites/default/files/raman2.png. [Accessed: 14-Oct-2019].

[150] A. (Ariel) Lipson, S. G. (Stephen G. . Lipson, and H. (Henry) Lipson, *Optical physics*. Cambridge University Press, 2011.

[151] E. Ruska, "The early development of electron lenses and electron microscopy.," *Microsc.*

Acta. Suppl., no. Suppl 5, pp. 1–140, 1980.

[152] L. V. P. R. de Broglie, "Recherches sur la théorie des quanta," *Ann. Phys.*, vol. 2, pp. 22–128, 1925.

[153] "transmission electron microscopy (TEM)," in *IUPAC Compendium of Chemical Terminology*, Research Triagle Park, NC: IUPAC.

[154] D. McMullan, "Scanning electron microscopy 1928-1965," *Scanning*, vol. 17, no. 3, pp. 175–185, Dec. 2006.

[155] E. Pretorius, "Influence of acceleration voltage on scanning electron microscopy of human blood platelets," *Microsc. Res. Tech.*, p. NA-NA, 2009.

[156] J. Goldstein *et al.*, *Scanning Electron Microscopy and X-Ray Microanalysise*. Springer US, 2003.

[157] G. Binnig, C. F. Quate, and C. Gerber, "Atomic Force Microscope," *Phys. Rev. Lett.*, vol. 56, no. 9, pp. 930–933, Mar. 1986.

[158] S. Bertolazzi, J. Brivio, … A. R.-M. and, and undefined 2013, "Exploring flatland: AFM of mechanical and electrical properties of graphene, MoS2 and other low-dimensional materials," *microscopy-analysis.com*.

[159] Y. K. Yong, A. Bazaei, and S. O. R. Moheimani, "Video-Rate Lissajous-Scan Atomic Force Microscopy," *IEEE Trans. Nanotechnol.*, vol. 13, no. 1, pp. 85–93, Jan. 2014.

[160] C. O'Mahony, E. U. Haq, C. Sillien, and S. A. M. Tofail, "Rheological Issues in Carbon-Based Inks for Additive Manufacturing," *Micromachines*, vol. 10, no. 2, p. 99, Jan. 2019.

[161] J. D. Jackson, "Classical Electrodynamics Third Edition: 9780471309321." .

[162] R. Waterhouse, Ed., *Printed Antennas for Wireless Communications*. Chichester, UK: John Wiley & Sons, Ltd, 2007.

[163] G. A. Casula, G. Montisci, and G. Mazzarella, "A Wideband PET Inkjet-Printed Antenna for UHF RFID," *IEEE Antennas Wirel. Propag. Lett.*, vol. 12, pp. 1400–1403, 2013.

[164] A. Scidà *et al.*, "Application of graphene-based flexible antennas in consumer electronic devices," *Mater. Today*, vol. 21, no. 3, pp. 223–230, Apr. 2018.

[165] N. Curreli *et al.*, "Graphene-based ultra-wide band printed bow-tie antenna for remote tracking - IEEE Conference Publication." [Online]. Available:

https://ieeexplore.ieee.org/abstract/document/8739804/authors#authors. [Accessed: 28-Oct-2019].

[166] R. F. Harrington, “Effect of Antenna Size on Gain, Bandwidth, and Efficiency,” *Journa l Res. Natl. Bur. Stand.*, 1960.

[167] R. E. Collin, *Antennas and Radiowave Propagation*. 1985.

[168] D. M. Pozar, *Microwave Engineering (4th ed.)*. .

[169] M. Salanne, “Ionic Liquids for Supercapacitor Applications,” *Topics in Current Chemistry*, vol. 375, no. 3. Springer Verlag, 01-Jun-2017.

[170] T. W. Napporn *et al.*, “Electrochemical Measurement Methods and Characterization on the Cell Level,” in *Fuel Cells and Hydrogen*, Elsevier, 2018, pp. 175–214.

[171] H. J. Haugan, S. Elhamri, F. Szmulowicz, B. Ullrich, G. J. Brown, and W. C. Mitchel, “Study of residual background carriers in midinfrared InAs⁄GaSb superlattices for uncooled detector operation,” *Appl. Phys. Lett.*, vol. 92, no. 7, p. 071102, Feb. 2008.

[172] M. Long, P. Wang, H. Fang, and W. Hu, “Progress, Challenges, and Opportunities for 2D Material Based Photodetectors,” *Adv. Funct. Mater.*, vol. 29, no. 19, p. 1803807, May 2019.

[173] M.-K. Lee, C.-H. Chu, Y.-H. Wang, and S. M. Sze, “155-μm and infrared-band photoresponsivity of a Schottky barrier porous silicon photodetector,” *Opt. Lett.*, vol. 26, no. 3, p. 160, Feb. 2001.

[174] B. M. Onat, W. Huang, N. Masaun, M. Lange, M. H. Ettenberg, and C. Dries, “Ultra-low dark current InGaAs technology for focal plane arrays for low-light level visible-shortwave infrared imaging,” 2007, p. 65420L.

[175] Z. Wang *et al.*, “InGaAs PIN photodetectors integrated and vertically coupled with silicon-on-insulator waveguides,” *Opt. Eng.*, vol. 53, no. 5, p. 057101, May 2014.

[176] P. Maity, S. V. Singh, S. Biring, B. N. Pal, and A. K. Ghosh, “Selective near-infrared (NIR) photodetectors fabricated with colloidal CdS:Co quantum dots,” *J. Mater. Chem. C*, vol. 7, no. 25, pp. 7725–7733, 2019.

[177] A. Rogalski, “HgCdTe infrared detector material: history, status and outlook,” *Reports Prog. Phys.*, vol. 68, no. 10, pp. 2267–2336, Oct. 2005.

[178] A. Rogalski, “Comparison of the performance of quantum well and conventional bulk

infrared photodetectors," *Infrared Phys. Technol.*, vol. 38, no. 5, pp. 295–310, Aug. 1997.

[179] C. H. Grein, P. M. Young, M. E. Flatté, and H. Ehrenreich, "Long wavelength InAs/InGaSb infrared detectors: Optimization of carrier lifetimes," *J. Appl. Phys.*, vol. 78, no. 12, pp. 7143–7152, Dec. 1995.

[180] C. H. T. Lin *et al.*, "Type-II InAs/InGaSb SL photodetectors," 2000, p. 133.

[181] I. Kimukin, N. Biyikli, T. Kartaloglu, O. Aytur, and E. Ozbay, "High-Speed InSb Photodetectors on GaAs for Mid-IR Applications," *IEEE J. Sel. Top. Quantum Electron.*, vol. 10, no. 4, pp. 766–770, Jul. 2004.

[182] D. Akinwande, N. Petrone, and J. Hone, "Two-dimensional flexible nanoelectronics," *Nat. Commun.*, vol. 5, no. 1, p. 5678, Dec. 2014.

[183] G. Wu *et al.*, "Ultrahigh photoresponsivity MoS 2 photodetector with tunable photocurrent generation mechanism," *Nanotechnology*, vol. 29, no. 48, p. 485204, Nov. 2018.

[184] S. Krishna, A. Sharma, N. Aggarwal, S. Husale, and G. Gupta, "Ultrafast photoresponse and enhanced photoresponsivity of Indium Nitride based broad band photodetector," *Sol. Energy Mater. Sol. Cells*, vol. 172, pp. 376–383, Dec. 2017.

[185] J. D. Yao, Z. Q. Zheng, and G. W. Yang, "Production of large-area 2D materials for high-performance photodetectors by pulsed-laser deposition," *Prog. Mater. Sci.*, vol. 106, p. 100573, Dec. 2019.

[186] X. An, F. Liu, Y. J. Jung, and S. Kar, "Tunable Graphene–Silicon Heterojunctions for Ultrasensitive Photodetection," *Nano Lett.*, vol. 13, no. 3, pp. 909–916, Mar. 2013.

[187] H. Chandra, S. Allen, S. Oberloier, N. Bihari, J. Gwamuri, and J. Pearce, "Open-Source Automated Mapping Four-Point Probe," *Materials (Basel).*, vol. 10, no. 2, p. 110, Jan. 2017.

[188] F. M. Smits, "Measurement of Sheet Resistivities with the Four-Point Probe," *Bell Syst. Tech. J.*, vol. 37, no. 3, pp. 711–718, May 1958.

[189] A. Marzuki, *Packaged Transistor Characterization Methodology*. Hewlett-Packard Malaysia, 1998.

[190] A. Tracton, *Coatings Technology: Fundamentals, Testing, and Processing Techniques*. Boca Raton,Fla. : CRC Press, 2007.

[191] K. Arapov, R. Abbel, G. de With, and H. Friedrich, "Inkjet printing of graphene," *Faraday*

Discuss., vol. 173, pp. 323–336, 2014.

[192] K.-J. Baeg *et al.*, “Charge Injection Engineering of Ambipolar Field-Effect Transistors for High-Performance Organic Complementary Circuits,” *ACS Appl. Mater. Interfaces*, vol. 3, no. 8, pp. 3205–3214, Aug. 2011.

[193] A. Singh, M. Agrawal, and F. M. Marshall, “The role of organic vs. inorganic fertilizers in reducing phytoavailability of heavy metals in a wastewater-irrigated area,” *Ecol. Eng.*, vol. 36, no. 12, pp. 1733–1740, Dec. 2010.

[194] J. J. van Franeker *et al.*, “All-solution-processed organic solar cells with conventional architecture,” *Sol. Energy Mater. Sol. Cells*, vol. 117, pp. 267–272, Oct. 2013.

[195] R. D. Deegan, O. Bakajin, T. F. Dupont, G. Huber, S. R. Nagel, and T. A. Witten, “Capillary flow as the cause of ring stains from dried liquid drops,” *Nature*, vol. 389, no. 6653, pp. 827–829, Oct. 1997.

[196] J. Li, M. M. Naiini, S. Vaziri, M. C. Lemme, and M. Östling, “Inkjet Printing of MoS 2,” *Adv. Funct. Mater.*, vol. 24, no. 41, pp. 6524–6531, Nov. 2014.

[197] “Fujimilm user manual,” 2014.

[198] C. A. Mack and Society of Photo-optical Instrumentation Engineers., *Field guide to optical lithography*. SPIE, 2006.

[199] M. J. Madou, *Fundamentals of Microfabrication: The Science of Miniaturization*. .

[200] T. M. Mayer, “Field emission characteristics of the scanning tunneling microscope for nanolithography,” *J. Vac. Sci. Technol. B Microelectron. Nanom. Struct.*, vol. 14, no. 4, p. 2438, Jul. 1996.

[201] P. Rai-Choudhury, *Handbook of Microlithography, Micromachining, and Microfabrication. Volume 1: Microlithography*. SPIE PRESS, 1997.

[202] A. A. Tseng, Kuan Chen, C. D. Chen, and K. J. Ma, “Electron beam lithography in nanoscale fabrication: recent development,” *IEEE Trans. Electron. Packag. Manuf.*, vol. 26, no. 2, pp. 141–149, Apr. 2003.

[203] K. S. Sree Harsha, *Principles of Vapor Deposition of Thin Films*. Elsevier Ltd, 2006.

[204] W. M. Haynes, *CRC Handbook of Chemistry and Physics, 97th Edition*. CRC Press, 2016.

[205] C. J. Zhang *et al.*, “Enabling Flexible Heterostructures for Li-Ion Battery Anodes Based on

Nanotube and Liquid-Phase Exfoliated 2D Gallium Chalcogenide Nanosheet Colloidal Solutions," *Small*, vol. 13, no. 34, p. 1701677, Sep. 2017.

[206] *The Role of the Chemical Sciences in Finding Alternatives to Critical Resources*. National Academies Press, 2012.

[207] K. K. Das *et al.*, "Primary concept of nickel toxicity – an overview," *J. Basic Clin. Physiol. Pharmacol.*, vol. 30, no. 2, pp. 141–152, Mar. 2019.

[208] C. J. Shearer, A. D. Slattery, A. J. Stapleton, J. G. Shapter, and C. T. Gibson, "Accurate thickness measurement of graphene," *Nanotechnology*, vol. 27, no. 12, p. 125704, Mar. 2016.

[209] A. K. Geim and K. S. Novoselov, "The rise of graphene," *Nat. Mater.*, vol. 6, no. 3, pp. 183–191, Mar. 2007.

[210] A. Ansaldo *et al.*, "Graphene-based ultra-wide band printed antennas," *Prep.*

[211] "Regulations.gov - Proposed Rule Document." [Online]. Available: https://www.regulations.gov/document?D=EPA-HQ-OPPT-2016-0231-0001. [Accessed: 31-Oct-2019].

[212] "Summary of obligations resulting from inclusion of SVHCS in the Candidate List - ECHA." [Online]. Available: https://echa.europa.eu/candidate-list-obligations. [Accessed: 31-Oct-2019].

[213] J. N. Coleman, "Liquid Exfoliation of Defect-Free Graphene," *Acc. Chem. Res.*, vol. 46, no. 1, pp. 14–22, Jan. 2013.

[214] M. V. Bracamonte, G. I. Lacconi, S. E. Urreta, and L. E. F. Foa Torres, "On the Nature of Defects in Liquid-Phase Exfoliated Graphene," *J. Phys. Chem. C*, vol. 118, no. 28, pp. 15455–15459, Jul. 2014.

[215] R. Buzio *et al.*, "Ultralow friction of ink-jet printed graphene flakes," *Nanoscale*, vol. 9, no. 22, pp. 7612–7624, 2017.

[216] D. Yang *et al.*, "Chemical analysis of graphene oxide films after heat and chemical treatments by X-ray photoelectron and Micro-Raman spectroscopy," *Carbon N. Y.*, vol. 47, no. 1, pp. 145–152, Jan. 2009.

[217] S. Khan, L. Lorenzelli, and R. S. Dahiya, "Technologies for Printing Sensors and Electronics Over Large Flexible Substrates: A Review," *IEEE Sens. J.*, vol. 15, no. 6, pp. 3164–3185,

Jun. 2015.

[218] R. H. Leach, P. J. Pierce, E. P. Hickman, M. J. Mackenzie, and H. G. Smith, *The Printing Ink Manual (Fifth Edition)*. Springer, 1993.

[219] E. H. Jewell, T. C. Claypole, and D. T. Gethin, "Viscosity control in the screen printing of ceramic transfers," *Surf. Coatings Int. Part B Coatings Trans.*, vol. 86, no. 2, pp. 155–162, Jun. 2003.

[220] E. Jewell, B. Philip, and P. Greenwood, "Improved manufacturing performance of screen printed carbon electrodes through material formulation," *Biosensors*, vol. 6, no. 3, 2016.

[221] H. Sun *et al.*, "Binder-free graphene as an advanced anode for lithium batteries," *J. Mater. Chem. A*, vol. 4, no. 18, pp. 6886–6895, 2016.

[222] W. J. Hyun, E. B. Secor, M. C. Hersam, C. D. Frisbie, and L. F. Francis, "High-Resolution Patterning of Graphene by Screen Printing with a Silicon Stencil for Highly Flexible Printed Electronics," *Adv. Mater.*, vol. 27, no. 1, pp. 109–115, Jan. 2015.

[223] L. Debbichi, O. Eriksson, and S. Lebègue, "Two-Dimensional Indium Selenides Compounds: An Ab Initio Study," *J. Phys. Chem. Lett.*, vol. 6, no. 15, pp. 3098–3103, Aug. 2015.

[224] E. Petroni *et al.*, "Liquid-Phase Exfoliated Indium-Selenide Flakes and Their Application in Hydrogen Evolution Reaction," *Small*, vol. 14, no. 26, p. 1800749, Jun. 2018.

[225] N. Curreli *et al.*, "Liquid phase exfoliated indium selenide-based highly sensitive photodetectors," *Prep.*

[226] J. Lauth *et al.*, "Solution-Processed Two-Dimensional Ultrathin InSe Nanosheets," *Chem. Mater.*, vol. 28, no. 6, pp. 1728–1736, Mar. 2016.

[227] D. Han, Y. Khan, K. Gopalan, A. Pierre, and A. C. Arias, "Emission Area Patterning of Organic Light-Emitting Diodes (OLEDs) via Printed Dielectrics," *Adv. Funct. Mater.*, vol. 28, no. 37, p. 1802986, Sep. 2018.

[228] A. Koptioug, P. Jonsson, J. Sidén, T. Olsson, and M. Gulliksson, "On the behavior of printed RFID tag antennas, using conductive paint," in *Proceedings of Antennas and Propagation*, 2003.

[229] A. Fanti *et al.*, "A polycarbonate RFID tag for blood chain tracking," in *2015 IEEE International Symposium on Antennas and Propagation & USNC/URSI National Radio*

Science Meeting, 2015, pp. 356–357.

[230] A. Iravani, M. H. Akbari, and M. Zohoori, "Advantages and Disadvantages of Green Technology; Goals, Challenges and Strengths," *Int. J. Sci. Eng. Appl.*, vol. 6, no. 9, pp. 272–284, Sep. 2017.

[231] G. H. Brown and O. M. Woodward, "Experimentally Determined Impedance Characteristics of Cylindrical Antennas," *Proc. IRE*, vol. 33, no. 4, pp. 257–262, Apr. 1945.

[232] G. G. Xiao, Z. Zhang, S. Lang, and Y. Tao, "Screen printing RF antennas," in *2016 17th International Symposium on Antenna Technology and Applied Electromagnetics (ANTEM)*, 2016, pp. 1–2.

[233] C. Reig and E. Avila-Navarro, "Printed Antennas for Sensor Applications: A Review," *IEEE Sens. J.*, vol. 14, no. 8, pp. 2406–2418, Aug. 2014.

[234] "Amateur Service page." [Online]. Available: http://life.itu.int/radioclub/ars.htm. [Accessed: 04-Nov-2019].

[235] S. A. Weis, "RFID (Radio Frequency Identification): Principles and Applications."

[236] L. J. Boggs, D. Law, and H. Taniguchi, "Rheological parameters of waterborne coatings. Material characteristics of these systems compared to coatings with good flake orientation," *Eur. Coatings J.*, no. 5, pp. 350–353, 1998.

[237] "Letter designations of microwave bands." [Online]. Available: https://www.jneuhaus.com/fccindex/letter.html. [Accessed: 04-Nov-2019].

[238] D. Martin, P. Anderson, and L. Bartmian, *Communication Satellites (5th Ed.)*. 2008.

[239] S. Ghazizadeh, "Acceptance Theory on Mobile Services and Applications," 2012.

[240] "A.I.R. T-DAB Tabella VHF-III." [Online]. Available: http://www.air-radio.it/T_DAB.html. [Accessed: 04-Nov-2019].

[241] M. Houssa, A. Dimoulas, and A. Molle, "Silicene: a review of recent experimental and theoretical investigations," *J. Phys. Condens. Matter*, vol. 27, no. 25, p. 253002, Jun. 2015.

[242] M. Derivaz *et al.*, "Continuous Germanene Layer on Al(111)," *Nano Lett.*, vol. 15, no. 4, pp. 2510–2516, Apr. 2015.

[243] J. O. Island, G. A. Steele, H. S. J. van der Zant, and A. Castellanos-Gomez, "Environmental instability of few-layer black phosphorus," *2D Mater.*, vol. 2, no. 1, p. 011002, Jan. 2015.

[244] C. Lamuta *et al.*, “Indentation fracture toughness of single-crystal Bi2Te3 topological insulators,” *Nano Res.*, vol. 9, no. 4, pp. 1032–1042, Apr. 2016.

[245] N. Kuroda and Y. Nishina, “Resonance Raman scattering study on exciton and polaron anisotropies in InSe,” *Solid State Commun.*, vol. 34, no. 6, pp. 481–484, May 1980.

[246] M. Brotons-Gisbert *et al.*, “Nanotexturing To Enhance Photoluminescent Response of Atomically Thin Indium Selenide with Highly Tunable Band Gap,” *Nano Lett.*, vol. 16, no. 5, pp. 3221–3229, May 2016.

[247] J. Camassel, P. Merle, H. Mathieu, and A. Chevy, “Excitonic absorption edge of indium selenide,” *Phys. Rev. B*, vol. 17, no. 12, pp. 4718–4725, Jun. 1978.

[248] G. W. Mudd *et al.*, “The direct-to-indirect band gap crossover in two-dimensional van der Waals Indium Selenide crystals,” *Sci. Rep.*, vol. 6, no. 1, p. 39619, Dec. 2016.

[249] S. M. Sze and K. K. Ng, *Physics of Semiconductor Devices*. Hoboken, NJ, USA, NJ, USA: John Wiley & Sons, Inc., 2006.

[250] T. Smeeton and C. Humphreys, “Perspectives on Electronic and Photonic Materials,” in *Springer Handbook of Electronic and Photonic Materials*, Cham: Springer International Publishing, 2017, pp. 1–1.

[251] G. Micocci, A. Rizzo, P. Siciliano, and A. Tepore, “Deep Level Transient Spectroscopy Measurements in InSe Single Crystals,” *Phys. Status Solidi*, vol. 114, no. 1, pp. 253–257, Jul. 1989.

[252] G. Micocci, P. Siciliano, and A. Tepore, “Photoinduced current transient spectroscopy in InSe single crystals,” *Sol. Energy Mater.*, vol. 20, no. 3, pp. 181–187, Mar. 1990.

[253] M. Kielar, O. Dhez, G. Pecastaings, A. Curutchet, and L. Hirsch, “Long-Term Stable Organic Photodetectors with Ultra Low Dark Currents for High Detectivity Applications,” *Sci. Rep.*, vol. 6, no. 1, p. 39201, Dec. 2016.

[254] X. He, F. Léonard, and J. Kono, “Uncooled Carbon Nanotube Photodetectors,” *Adv. Opt. Mater.*, vol. 3, no. 8, pp. 989–1011, Aug. 2015.

[255] J. Wojtas *et al.*, “Cavity-Enhanced Absorption Spectroscopy and Photoacoustic Spectroscopy for Human Breath Analysis,” *Int. J. Thermophys.*, vol. 35, no. 12, pp. 2215–2225, Dec. 2014.

[256] J. Kang *et al.*, “Solution-Based Processing of Optoelectronically Active Indium Selenide,” *Adv. Mater.*, vol. 30, no. 38, p. 1802990, Sep. 2018.

[257] J.-F. Wang *et al.*, “Surface engineering of perovskite films for efficient solar cells,” *Sci. Rep.*, vol. 7, no. 1, p. 14478, Dec. 2017.

[258] Y.-O. Choi, N.-H. Kim, J.-S. Park, and W.-S. Lee, “Influences of thickness-uniformity and surface morphology on the electrical and optical properties of sputtered CdTe thin films for large-area II–VI semiconductor heterostructured solar cells,” *Mater. Sci. Eng. B*, vol. 171, no. 1–3, pp. 73–78, Jul. 2010.

[259] D. Periyanagounder, P. Gnanasekar, P. Varadhan, J.-H. He, and J. Kulandaivel, “High performance, self-powered photodetectors based on a graphene/silicon Schottky junction diode,” *J. Mater. Chem. C*, vol. 6, no. 35, pp. 9545–9551, 2018.

[260] Z. Li *et al.*, “High-Performance Photo-Electrochemical Photodetector Based on Liquid-Exfoliated Few-Layered InSe Nanosheets with Enhanced Stability,” *Adv. Funct. Mater.*, vol. 28, no. 16, p. 1705237, Apr. 2018.

[261] S. R. Tamalampudi *et al.*, “High Performance and Bendable Few-Layered InSe Photodetectors with Broad Spectral Response,” *Nano Lett.*, vol. 14, no. 5, pp. 2800–2806, May 2014.

[262] M. Buscema, D. J. Groenendijk, S. I. Blanter, G. A. Steele, H. S. J. van der Zant, and A. Castellanos-Gomez, “Fast and Broadband Photoresponse of Few-Layer Black Phosphorus Field-Effect Transistors,” *Nano Lett.*, vol. 14, no. 6, pp. 3347–3352, Jun. 2014.

[263] O. Lopez-Sanchez, D. Lembke, M. Kayci, A. Radenovic, and A. Kis, “Ultrasensitive photodetectors based on monolayer MoS2,” *Nat. Nanotechnol.*, vol. 8, no. 7, pp. 497–501, Jul. 2013.

[264] K. Roy *et al.*, “Graphene–MoS2 hybrid structures for multifunctional photoresponsive memory devices,” *Nat. Nanotechnol.*, vol. 8, no. 11, pp. 826–830, Nov. 2013.

[265] J. A. Garrido, E. Monroy, I. Izpura, and E. Muñoz, “Photoconductive gain modelling of GaN photodetectors,” *Semicond. Sci. Technol.*, vol. 13, no. 6, pp. 563–568, Jun. 1998.

[266] M.-L. Lu, C.-W. Lai, H.-J. Pan, C.-T. Chen, P.-T. Chou, and Y.-F. Chen, “A Facile Integration of Zero- (I–III–VI Quantum Dots) and One- (Single SnO 2 Nanowire) Dimensional Nanomaterials: Fabrication of a Nanocomposite Photodetector with Ultrahigh Gain and Wide Spectral Response,” *Nano Lett.*, vol. 13, no. 5, pp. 1920–1927, May 2013.

[267] H. Yin, A. Akey, and R. Jaramillo, “Large and persistent photoconductivity due to hole-hole

correlation in CdS," *Phys. Rev. Mater.*, vol. 2, no. 8, p. 084602, Aug. 2018.

[268] M. Beidaghi and Y. Gogotsi, "Capacitive energy storage in micro-scale devices: recent advances in design and fabrication of micro-supercapacitors," *Energy Environ. Sci.*, vol. 7, no. 3, p. 867, 2014.

[269] C. Shen, S. Xu, Y. Xie, M. Sanghadasa, X. Wang, and L. Lin, "A Review of On-Chip Micro Supercapacitors for Integrated Self-Powering Systems," *J. Microelectromechanical Syst.*, vol. 26, no. 5, pp. 949–965, Oct. 2017.

[270] Z.-S. Wu, X. Feng, and H.-M. Cheng, "Recent advances in graphene-based planar micro-supercapacitors for on-chip energy storage," *Natl. Sci. Rev.*, vol. 1, no. 2, pp. 277–292, Jun. 2014.

[271] D. Qi, Y. Liu, Z. Liu, L. Zhang, and X. Chen, "Design of Architectures and Materials in In-Plane Micro-supercapacitors: Current Status and Future Challenges," *Advanced Materials*, vol. 29, no. 5. Wiley-VCH Verlag, 02-Feb-2017.

[272] A. Tyagi, K. M. Tripathi, and R. K. Gupta, "Recent progress in micro-scale energy storage devices and future aspects," *J. Mater. Chem. A*, vol. 3, no. 45, pp. 22507–22541, 2015.

[273] G. Wang, L. Zhang, and J. Zhang, "A review of electrode materials for electrochemical supercapacitors," *Chemical Society Reviews*, vol. 41, no. 2. pp. 797–828, 21-Jan-2012.

[274] Y. Zhang *et al.*, "Progress of electrochemical capacitor electrode materials: A review," *International Journal of Hydrogen Energy*, vol. 34, no. 11. pp. 4889–4899, Jun-2009.

[275] J. Lee, P. Srimuk, S. Fleischmann, X. Su, T. A. Hatton, and V. Presser, "Redox-electrolytes for non-flow electrochemical energy storage: A critical review and best practice," *Prog. Mater. Sci.*, vol. 101, pp. 46–89, Apr. 2019.

[276] A. Ansaldo *et al.*, "High-power graphene–Carbon nanotube hybrid supercapacitors," *ChemNanoMat*, vol. 3, no. 6, pp. 436–446, Jun. 2017.

[277] Z. Wu, K. Parvez, X. Feng, and K. Müllen, "Graphene-based in-plane micro-supercapacitors with high power and energy densities," *Nat. Commun.*, vol. 4, no. 1, p. 2487, Dec. 2013.

[278] W. Gao *et al.*, "Direct laser writing of micro-supercapacitors on hydrated graphite oxide films," *Nat. Nanotechnol.*, vol. 6, no. 8, pp. 496–500, Aug. 2011.

[279] Z. Niu, L. Zhang, L. Liu, B. Zhu, H. Dong, and X. Chen, "All-Solid-State Flexible Ultrathin Micro-Supercapacitors Based on Graphene," *Adv. Mater.*, vol. 25, no. 29, pp. 4035–4042,

Aug. 2013.

[280] Z.-S. Wu, K. Parvez, X. Feng, and K. Müllen, “Photolithographic fabrication of high-performance all-solid-state graphene-based planar micro-supercapacitors with different interdigital fingers,” *J. Mater. Chem. A*, vol. 2, no. 22, p. 8288, 2014.

[281] Q. Cheng, J. Tang, J. Ma, H. Zhang, N. Shinya, and L.-C. Qin, “Graphene and carbon nanotube composite electrodes for supercapacitors with ultra-high energy density,” *Phys. Chem. Chem. Phys.*, vol. 13, no. 39, p. 17615, 2011.

[282] Y. Wang *et al.*, “Preventing Graphene Sheets from Restacking for High-Capacitance Performance,” *J. Phys. Chem. C*, vol. 115, no. 46, pp. 23192–23197, Nov. 2011.

[283] Z. Fan *et al.*, “A Three-Dimensional Carbon Nanotube/Graphene Sandwich and Its Application as Electrode in Supercapacitors,” *Adv. Mater.*, vol. 22, no. 33, pp. 3723–3728, Sep. 2010.

[284] F. Du, D. Yu, L. Dai, S. Ganguli, V. Varshney, and A. K. Roy, “Preparation of Tunable 3D Pillared Carbon Nanotube–Graphene Networks for High-Performance Capacitance,” *Chem. Mater.*, vol. 23, no. 21, pp. 4810–4816, Nov. 2011.

[285] H. R. Byon, S. W. Lee, S. Chen, P. T. Hammond, and Y. Shao-Horn, “Thin films of carbon nanotubes and chemically reduced graphenes for electrochemical micro-capacitors,” *Carbon N. Y.*, vol. 49, no. 2, pp. 457–467, Feb. 2011.

[286] D. T. Pham *et al.*, “Carbon Nanotube-Bridged Graphene 3D Building Blocks for Ultrafast Compact Supercapacitors,” *ACS Nano*, vol. 9, no. 2, pp. 2018–2027, Feb. 2015.

[287] N. Devillers, S. Jemei, M.-C. Péra, D. Bienaimé, and F. Gustin, “Review of characterization methods for supercapacitor modelling,” *J. Power Sources*, vol. 246, pp. 596–608, Jan. 2014.

[288] M. F. El-Kady and R. B. Kaner, “Scalable fabrication of high-power graphene micro-supercapacitors for flexible and on-chip energy storage,” *Nat. Commun.*, vol. 4, no. 1, p. 1475, Jun. 2013.

[289] Y. Yang *et al.*, “Waterproof, Ultrahigh Areal-Capacitance, Wearable Supercapacitor Fabrics,” *Adv. Mater.*, vol. 29, no. 19, p. 1606679, May 2017.

[290] H. Kim *et al.*, “Encapsulated, High-Performance, Stretchable Array of Stacked Planar Micro-Supercapacitors as Waterproof Wearable Energy Storage Devices,” *ACS Appl. Mater. Interfaces*, vol. 8, no. 25, pp. 16016–16025, Jun. 2016.

[291] F. Yi *et al.*, “Stretchable and Waterproof Self-Charging Power System for Harvesting Energy from Diverse Deformation and Powering Wearable Electronics,” *ACS Nano*, vol. 10, no. 7, pp. 6519–6525, Jul. 2016.

[292] G. Camino, A. Maffezzoli, M. Braglia, M. De Lazzaro, and M. Zammarano, “Effect of hydroxides and hydroxycarbonate structure on fire retardant effectiveness and mechanical properties in ethylene-vinyl acetate copolymer,” *Polym. Degrad. Stab.*, vol. 74, no. 3, pp. 457–464, Jan. 2001.

[293] A. W. Czanderna and F. J. Pern, “Encapsulation of PV modules using ethylene vinyl acetate copolymer as a pottant: A critical review,” *Sol. Energy Mater. Sol. Cells*, vol. 43, no. 2, pp. 101–181, Sep. 1996.